

12-2016

Conductive inks and films via intense pulsed light.

Gabriel L. Draper

Follow this and additional works at: <http://ir.library.louisville.edu/etd>

 Part of the [Chemical Engineering Commons](#)

Recommended Citation

Draper, Gabriel L., "Conductive inks and films via intense pulsed light." (2016). *Electronic Theses and Dissertations*. Paper 2564.
<https://doi.org/10.18297/etd/2564>

This Doctoral Dissertation is brought to you for free and open access by ThinkIR: The University of Louisville's Institutional Repository. It has been accepted for inclusion in Electronic Theses and Dissertations by an authorized administrator of ThinkIR: The University of Louisville's Institutional Repository. This title appears here courtesy of the author, who has retained all other copyrights. For more information, please contact thinkir@louisville.edu.

CONDUCTIVE INKS AND FILMS VIA INTENSE PULSED LIGHT

By

Gabriel L. Draper
B.S., University of Colorado at Boulder, 2012

A Dissertation
Submitted to the Faculty of the
J. B. Speed School of Engineering of the University of Louisville
In Partial Fulfillment of the Requirements
For the Degree of

Doctor of Philosophy
in Chemical Engineering

Department of Chemical Engineering
University of Louisville
Louisville, Kentucky

December 2016

CONDUCTIVE INKS AND FILMS VIA INTENSE PULSED LIGHT

By

Gabriel L. Draper
B.S., University of Colorado at Boulder, 2012

A Dissertation Approved on

November 30th, 2016

By the following Dissertation Committee:

Dissertation co-Director

Dr. Thad Druffel

Dissertation co-Director

Dr. Mahendra Sunkara

Dr. Thomas Starr

Dr. Kevin Walsh

Dr. Gerold Willing

DEDICATION

I dedicate this to everyone who has helped me along the way and especially close family
and friends.

Love you Mom with all of my heart!! Love you Phil!

Love you Curtis & Meighan!

Love you all of my cousins, step-siblings, half-siblings, nieces & nephews!

Love you Grandma & Richard!

You da best Kristina!

Thank you my friends since childhood Mikey, Mo, & John!

Thank you my bestest college buddies Devin, Bogdan, Andrew, Dom, Grant, Brian, Eran,
Erica, and Nigel! (To name a few!)

ACKNOWLEDGMENTS

I would like to thank my co-advisors Dr. Thad Druffel and Dr. Mahendra Sunkara. I would also like to thank the other committee members, Dr. Thomas Starr, Dr. Kevin Walsh, and Dr. Gerold Willing. I would also like to thank the University of Louisville Chemical Engineering Department and the Conn Center for Renewable Energy. I would also like to thank the postdocs that have mentored me in the lab Dr. Ruvini, Dr. Meneka Jha, and Dr. Krishnamraju Ankireddy. I would also like to thank my lab-mates Tu Nguyen, Maria Carreon, Ben Russell, Swathi Sunkara, Alejandro Martinez-Garcia, Apollo Nambo, Babajide Patrick Ajayi, Ruchira Dharmasena, and especially Zach Herde, Daniel Jaramillo and Brandon Lavery. I would also like to thank the students who have been my lab mentees Callie Shadrick, Madalyn Wead, Nathan Allen, Preston Dukes, J. Jacobs, David Lincoln, Aaron Fegenbush, and Robbie Spalding.

I would also like to thank the University of Louisville School of Interdisciplinary Graduate Studies, especially Dr. Michelle Rodems, Dr. Latonia Craig, and Dean Beth Boehm. I would also like to thank the University of Louisville administration including Dr. Mordean Taylor-Archer, Diana Whitlock, Brian Buford, Heidi Neal, Dean Gail Depuy, and Dr. Neville Pinto. I would also like to thank the University of Louisville Writing Center, especially Amy Nichols and Chris Scheidler.

I would also like to thank the University of Louisville Cultural Center, especially Sarah Nunez, Norah Atkins, Tierney Bates, and Joey Wilkerson. I would also like to thank

the University of Louisville CODRE, COSW, the LGBT Center, and the Women's Center. I would also like to thank Dr. Derrick Brooms, Joe Goodman, Errol Wint, Khotso Libe, Darryl Young, Dr. Brenda Hart, Dr. Selene Phillips, Dr. Ricky Jones, Jeff Rushton, Sara Alvarez, Jesús Ibáñez, Tania Avalos, Talesha Wilson, Caitlin Durgin, Emmanuel Roque, Leo Salinas Chacon, John Rhodes, Brina Joiner, Segan Tella, and Jose Lopez.

I would also like to thank Andrea Diggs and Atkinson Elementary School for allowing me to visit as a mentor and see the brilliance potential of our youth, which always motivated me to push on.

I would also like to thank Campus Health Services at Cardinal Station and Dr. Zahorik for being an invaluable resource to balancing and learning about my health.

Lastly, I would also like to thank anyone who I may have not listed and organizations who have continually helped me to grow while having a positive impact especially NSBE and also the on campus organizations MAGS, NASO, & SAAB.

ABSTRACT

CONDUCTIVE INKS AND FILMS VIA INTENSE PULSED LIGHT

Gabriel L. Draper

November 30th, 2016

This research focuses on the investigation of Earth abundant copper and carbon based nanomaterials that are subjected to Intense Pulsed Light Processing to create conductive films, as future flexible electronics and renewable energy solutions would benefit from the quick and scalable production of conductive films. Use of nanomaterials in their oxide/hydroxide forms leads to higher stability in aqueous inks for efficient large area solution deposition.

IPL Processing utilized 2044 μs pulses ranging from 589 J - 2070 J over an area of 1.9 cm x 30.5 cm, with energy densities of 10.1, 12.8, 15.8, 19.2, 22.9, 26.8, 31.1 and 35.7 Jcm^{-2} , of non-coherent white light in wavelengths ranging from UV to NIR (240 nm – 1,000 nm) through a xenon lamp. The rapid pulses induce localized temperature increases in the films, flexible plastic substrates can be used without degradation. Three different morphological systems and nanomaterials were studied: 1D (copper hydroxide nanowires), 2D (Graphene Oxide nanosheets), and 3D (cuprous oxide encapsulated by nickel oxide nanoparticles & also copper nitrate hydroxide nanoparticles). The nanomaterials were rapidly reduced into conductive films via Intense Pulsed Light Processing aided through the organic decomposition of additives, providing a reducing environment. Through

inclusion of different materials and morphologies, nanoscale manipulations can lead to breakthroughs in advanced materials and additive manufacturing.

Cu₂O (20nm) nanoparticles encapsulated with a NiO layer were synthesized to explore protecting the Cu from oxidation and diffusion into Si based photovoltaic applications. The room temperature synthesis and IPL processes easily prevented formation of alloys at the copper-nickel interface. The encapsulation was shown to reduce Cu diffusion into Si.

Copper nitrate hydroxide, Cu₂(OH)₃NO₃, was synthesized under ambient conditions with copper nitrate and potassium hydroxide reagents and processed by IPL. Films were deposited by screen-printing and then subjected to IPL Processing. Since Cu₂NO₃(OH)₃ isn't a thermally stable material, initially transformed into CuO. However, when fructose or glucose were intentionally included as additives in the inks, IPL Processing provided direct conversion of the Cu₂(OH)₃NO₃ into Cu. Between the two sugars, fructose was more advantageous as it led to faster reduction and lower sheet resistances, with the lowest sheet resistance being 0.224 Ω/□.

Graphene oxide was reduced with Intense Pulsed Light Processing to explore potential towards scalable conductive films without the need for harsh/toxic reductants. The graphene oxide films on displayed a four magnitude decrease in sheet resistance from 55.1 MΩ/□. to 2280 Ω/□ after IPL. Plastic substrates required less energy to display reduction, with a four magnitude decrease in sheet resistance (62.5 MΩ/□. to 3.43 kΩ/□.) after IPL. When combined with Cu(OH)₂ nanowires at weight percentages of 1.82%, 8.47%, and 32.65%, films exhibited decreased sheet resistances by 25%, 45%, and 66%, respectively.

TABLE OF CONTENTS

DEDICATION	iii
ACKNOWLEDGMENTS	iv
ABSTRACT.....	vi
LIST OF TABLES	xii
LIST OF FIGURES	xiii
CHAPTER 1: INTRODUCTION.....	1
A. Highlights of Engineering Opportunities for Conductive Films in Photovoltaic (PV) Applications	4
B. Motivation for study of IPL Processing Oxide & Hydroxide Forms of Conductive Precursors	5
C. Proposed Concepts for Conductive Films via Intense Pulsed Light	7
D. Objectives for this Study of Nanomaterials & IPL Processing	10
E. Outline of Dissertation	11
F. Impact of Dissertation	11
CHAPTER 2: BACKGROUND.....	15
A. Types of Conductive Materials	22
1) Metal Materials and their Nanowire 1-D Embodiments	22
2) Metal Oxides Implemented as TCF Materials.....	22
3) Carbon-Based & Organic Materials	23

4)	Hybridization of TCF Materials	27
B.	Solution Phase Synthesis of Earth Abundant Precursor Nanomaterials	28
1)	Solution Phase Synthesis of Copper Nanomaterials.....	28
2)	Graphene Oxide (GO) Synthesis Methods	31
C.	Solution Phase Deposition	31
1)	Ink Formulation to Enable Solution Phase Deposition	31
2)	Importance of Substrate Choice on Film Deposition	32
3)	Solution Phase Deposition Methods.....	32
D.	Reduction and Processing Methods	34
CHAPTER 3: EXPERIMENTAL.....		39
A.	Solution Phase Synthesis of Cu ₂ O-NiO core-layer Nanostructures.....	39
B.	Synthesis of Copper Nitrate Hydroxide Cu ₂ NO ₃ (OH) ₃	42
C.	Synthesis of Graphene Oxide via a Modified Hummer's Method.....	42
D.	Synthesis of Copper Hydroxide Nanowires (NWs)	43
E.	Procedures for Cleaning Substrates.....	45
F.	Ink Formulation & Deposition	46
1)	Ultrasonic Spray Deposition of Cu ₂ O-NiO core-layer Nanostructures	46
2)	Screen Printing Cu ₂ NO ₃ (OH) ₃	46
3)	Spin-coating GO	47
4)	Ultrasonic Spray Deposition & Rod-coating of GO.....	47
5)	Spin-coated and drop-casted GO & Cu(OH) ₂ NW Mixtures	49
G.	IPL Processing Parameters and Techniques.....	50
1)	IPL Processing of Deposited Cu ₂ O-NiO core-layer Films.....	51

2)	IPL Processing of Deposited $\text{Cu}_2\text{NO}_3(\text{OH})_3$ Films	53
3)	IPL Processing of Deposited GO and GO & $\text{Cu}(\text{OH})_2$ Films	54
H.	Characterization Instruments Utilized for Study.....	55
CHAPTER 4: IPL PROCESSING $\text{Cu}_2\text{O}@\text{NiO}$ ENCAPSULATED		
NANOPARTICLES.....		
		58
A.	Introduction	58
B.	Results and Discussion.....	59
1)	Synthesized of Cu_2O -NiO core-layer Nanostructures	59
2)	XRD Regression Analysis to determine if Cu-Ni alloy is formed	67
3)	Elemental Distributions throughout IPL Processing	71
4)	Stability of Cu on Silicon	73
C.	Summary	75
CHAPTER 5: IPL PROCESSING OF $\text{Cu}_2\text{NO}_3(\text{OH})_3$ ENHANCED WITH FRUCTOSE		
AND GLUCOSE TO FABRICATE ELEMENTAL Cu		
		76
A.	Introduction	76
B.	Results and Discussion.....	77
1)	Synthesized Copper Nitrate Hydroxide.....	77
2)	Establishment of Baseline Conversion to CuO	79
3)	Direct Fabrication of Elemental through Intentional Inclusion of Fructose and Glucose for Enhanced IPL Processing.....	81
4)	Sheet Resistance of Produced Conductive Cu Films.....	86
C.	Summary	87

CHAPTER 6: REDUCTION OF GRAPHENE OXIDE NANOSHEETS AND Cu(OH) ₂	
NANOWIRES VIA INTENSE PULSED LIGHT PROCESSING	88
A. Introduction	88
B. Results and Discussion.....	88
1) Process Overview for IPL Processing of GO	88
2) Reduction of GO with IPL Processing	94
3) Demonstrated Use of Flexible Plastic for IPL Processing GO Films.....	99
4) Alternative Deposition Methods for Creation of GO Films	102
5) Cu(OH) ₂ NWs for Implementation for Engineering Hybridized Films	106
6) IPL Processing of Hybrid Films Deposited from Mixtures Containing GO and Cu(OH) ₂ NWs.....	108
C. Summary	112
CONCLUSIONS.....	113
RECOMMENDATIONS FOR FUTURE WORK	115
REFERENCES	116
CURRICULUM VITAE.....	131

LIST OF TABLES

Table 1: Characteristics of several TCF technologies	19
Table 2: Selected examples of organic decomposition during IPL Processing	36
Table 3: Comparison of thermal and IPL Processing reduction of GO ¹⁹¹	38
Table 4: Ultrasonic Spray Deposition Variables	48

LIST OF FIGURES

Figure 1: Relative abundance of the chemical elements in Earth's upper continental crust (http://pubs.usgs.gov/fs/2002/fs087-02/)	2
Figure 2: Structures of three types of photovoltaic (PV) cells featuring	5
Figure 3: (A) A Cu-ammonia complex, capped with a surfactant, is formed at the start of the synthesis. (B) The complex is oxidized, forming Cu ₂ O nanoparticles. Ni ²⁺ ions are added and adsorb on the surface of the Cu ₂ O. (C) Further addition of the reducing agent results in the formation of a NiO layer on the nanoparticles. (D-E) The inks are then ultrasonically sprayed on the substrate. (F) An IPL process reduces and sinters the film.	7
Figure 4: Overview schematic of Cu ₂ NO ₃ (OH) ₃ conversion into conductive copper from synthesis to deposition and IPL processing (featuring SEM images of the samples) envisioned for future scaled, commercial applications. The Cu ₂ NO ₃ (OH) ₃ is formed through a copper salt and hydroxide salt reaction.....	8
Figure 5: Conceptualization of 2D GO nanosheets and 1D Cu(OH) ₂ nanowires changing with IPL Processing	9
Figure 6: Conceptualization of hybridization of GO nanosheets and Cu(OH) ₂ nanowires together to create TCFs.....	10
Figure 7: NASA Satellite imaging of Earth at Night.....	13

Figure 8: EIA comparison of world energy consumption of OECD and non-OECD countries	14
Figure 9: ASTM G173-03 Reference Spectra	18
Figure 10: Calculated FOMs using Equation 7 for the TCFs referenced in Table 1	21
Figure 11: Flowchart of Concepts in Background Section	21
Figure 12: Illustration of chemical structure of GO and rGO post-reduction ⁵²	25
Figure 13: Structure of mers in PEDOT:PSS	26
Figure 14: Depiction of Ultrasonic Spray Deposition	33
Figure 15: Depiction of a Rod-coating tool	34
Figure 16: Depiction of close-up of the spiraled rod of a Rod-coating tool	34
Figure 17: Schematic of Cu(OH) ₂ NW Synthesis involving copper nitrate (copper precursor), NaOH (reactant), and PEG400 (as a shaping agent)	44
Figure 18: Image of reaction vessel after Cu(OH) ₂ synthesis vessel (left) and in a centrifuge tube prior to centrifugation process (right)	45
Figure 19: Photograph of 20 mg/mL GO solution displaying great ink stability nearly five months after it was formulated.....	48
Figure 20: Emitted light Spectrum for Xenon 4.2" lamp utilized for IPL Processing.....	50
Figure 21: Comparison of IPL Processing Energy Density Input versus time shown for forty 15.8 Jcm ⁻² pulses (red), forty 35.7Jcm ⁻² pulses (blue), and Incremental (black). Ther	51
Figure 22: Example of visible change of a Cu ₂ NO ₃ (OH) ₃ sample before (left) and after (right) IPL Processing	54
Figure 23: Photo of FEI SEM	57

Figure 24: Photo of Tescan SEM.....	57
Figure 25: Photo of X-ray Diffraction Instrument.....	57
Figure 26: Photo of Raman Spectrometer.....	57
Figure 27: TEM micrographs of Cu ₂ O@NiO nanostructures obtained using Ni ²⁺ concentration of (a) 1 mM, (b) 5 mM, and (c) 20 mM. The insets show high resolution TEM micrographs.	59
Figure 28: TEM-EDX pattern of samples (a) 1 mM, (b) 5 mM, (c) 10 mM and (d) 20 mM. The inset shows TEM-EDX quantification results: Ni/Cu atomic ratio	60
Figure 29: UV-Vis adsorption measurement of 1mM as deposited sample	61
Figure 30: FTIR spectrum (from top to bottom) of the as deposited, one IPL Pulse (energy density of 10.2 Jcm ⁻²), five IPL pulses (energy density of 10.2 Jcm ⁻²), and twenty IPL pulses 1mM samples (ten pulses at an energy density of 10.2 Jcm ⁻² and ten pulses at an energy density of 12.9 Jcm ⁻²). a) O-H bonds b) C-H alkane bonds c) C=O, C-O, and C-H bonds	64
Figure 31: (a) X-ray diffraction patterns of the films after IPL treatment formed using the 1 mM and 10 mM inks. The inset shows the effect of the concentration of Ni nitrate solution on the 2θ position and FWHM of the Cu(111) reflection. The error bars were calculated from the standard deviation. (b) Ratio of the intensity of the Cu(111)/Cu ₂ O (111) reflections after IPL treatment vs. the concentration of nickel nitrate used to fabricate the nickel shell. The error bars were calculated using the standard error. (c) Resistivity of the IPL treated films vs. concentration of nickel nitrate used to fabricate the nickel shell. (The results at 0 mM Nickel nitrate were taken from a previous study). ¹⁹³ The error bars were calculated using the standard error.	66

Figure 32: (a) Maximum Peak Position of the Cu(111) reflection versus the concentration of the nickel salt. (b) Residuals for the analysis of the Cu(111) reflection versus the concentration of the nickel salt. (c) Tabulated linear regression results.69

Figure 33: (a) FWHM of the Cu(111) reflection vs. the concentration of the Ni salt. (b) Residuals for the FWHM of the Cu(111) reflection vs. the concentration of the Ni salt. (c) Tabulated linear regression results.69

Figure 34: SEM images of the surface of the (a) as-deposited and (b & c) IPL treated films deposited using 1 mM inks. The films were treated using a total energy density input of (b) 231 Jcm⁻² and (c) 826.7 Jcm⁻²70

Figure 35: Nanostructures obtained after IPL Sintering using an initial Ni²⁺ concentration of 1 mM; (a) TEM micrograph (a-inset) HRTEM micrograph, (b) STEM, (c) Ni-K maps, (d) Cu-K maps and (e) Cu-K and Ni-K overlaid micrographs.71

Figure 36: Nanostructures obtained after IPL Sintering using initial Ni²⁺ with concentration of 5 mM (a) TEM micrograph, b) HRTEM micrograph, c) STEM, d) Ni-K mapping, e) Cu-K mapping f) Cu-K and Ni-K overlay mapped micrograph.72

Figure 37: Nanostructures obtained after IPL Sintering using initial Ni²⁺ with a concentration of 20 mM; (a) TEM micrograph, (b) HRTEM micrograph, (c) STEM, (d) Ni-K maps, (e) Cu-K maps and (f) Cu-K and Ni-K overlaid micrographs.72

Figure 38: Normalized thermoelectric power curves for the Si, Si/Cu and Si/Cu-Ni samples as a function of the temperature. The inset shows the setup for measuring the thermoelectric power.74

Figure 39: Characterization of synthesized copper nitrate hydroxide a) XRD b) Absorbance c) SEM d) TGA.79

Figure 40. FTIR of $\text{Cu}_2(\text{OH})_3\text{NO}_3$ with one (black), five (green), and ten (red) 12.8 Jcm^{-2} pulses of IPL processing	80
Figure 41: A) XRD results with IPL processing of forty pulses at increasing energy densities B) SEM images of IPL processed copper nitrate hydroxide films with forty pulses at varying energy densities.....	81
Figure 42: TGA and then the FTIR 12.8 Jcm^{-2} IPL processed fructose (left) and glucose samples (right)	83
Figure 43: XRD results with IPL processing of forty pulses at increasing energy densities for fructose (left) and glucose (right). SEM images of fructose (F-a-c) and glucose (G-a-c) samples at different energy densities of IPL processing a) 12.8 Jcm^{-2} c) 15.8 Jcm^{-2} c) 35.7 Jcm^{-2}	85
Figure 44: Sheet Resistance of IPL processed fructose films with forty pulses at varying energy densities.....	87
Figure 45: Overview schematic of spin-coated graphene oxide depositions and IPL processing	89
Figure 46: SDT of the as synthesized GO weight% (top), first order derivative of the weight% with respect to temperature (middle), and the heat flow normalized by the weight (bottom).....	91
Figure 47: Film thickness of the as deposited GO films (black circles) & with fructose (red diamonds).....	92
Figure 48: Transparency of deposited GO films (black circles) & with fructose (red diamonds).....	92

Figure 49: SEM Images of as deposited GO samples (with fructose) A) 5,000 rpm B) 4,000 rpm C) 3,000 rpm D) 2,000 rpm E) 1,000 rpm F) 500 rpm.....93

Figure 50: Comparison of sheet resistance IPL Processing Energy Density Inputs 1428 Jcm^{-2} and 1744 Jcm^{-2} , for both samples without fructose (black circles) and with fructose (red diamonds).94

Figure 51: SEM images of spin-coated GO (without fructose) at 3,000 rpm (top row) and 1,000 rpm (bottom row). The corresponding as deposited samples shown firstly (left), followed by two images at different magnifications of the samples post IPL Processing (center and right).....95

Figure 52: Transparency vs. Wavelength for 1,000 rpm spin-coated GO with fructose as deposited (black) and at several IPL Energy Density Inputs 178.5 Jcm^{-2} (red), 357 Jcm^{-2} (yellow), 632 Jcm^{-2} (blue), 714 Jcm^{-2} (purple), 1428 Jcm^{-2} (green), and 1744 Jcm^{-2} (brown).96

Figure 53: (Top) Transparency (Middle) Sheet Resistance and (Bottom) Raman peak ratio (I_D/I_G) with increasing total induced energy density through IPL Processing.....97

Figure 54: Film Thickness of 1,000 rpm spin-coated GO with fructose samples with increasing IPL Energy Density Input.....98

Figure 55: SEM imagery of 1,000 rpm spin-coated GO with fructose samples displaying film morphology at IPL Processing Energy Density Inputs of 632 Jcm^{-2} (left), 1428 Jcm^{-2} (center), and 1744 Jcm^{-2} . It is noted that the IPL processing of the 1744 Jcm^{-2} sample was done with an incremental IPL Processing scheme, which resulted in maintaining the nanosheets' orientations.....99

Figure 56: Cellulosic plastic sample (Top) film transparency and (Bottom) sheet resistance101

Figure 57: Bending of cellulosic plastic sample connected to a red LED and a DC Power Source at 2.81 V (left) 8.13 V (middle) and 15.0 V (right)101

Figure 58: Transparency (550nm) vs. # of Ultrasonic Spray Deposition Passes of GO films as deposited (black circles) and after IPL Processing with a 1428 Jcm⁻² Energy Density Input (red diamonds).102

Figure 59: Sheet Resistance versus # of Ultrasonic Spray Deposition passes of GO films after IPL Processing with an Energy Density Input of 1428 Jcm⁻².....103

Figure 60: Calculated Figure of Merit (FOM) versus # of Ultrasonic Spray Deposition passes of GO films after an IPL Processing Energy Density Input of 1428 Jcm⁻². .103

Figure 61: Average thickness versus # of Ultrasonic Spray Deposition Passes of GO films with error bars that indicate the standard deviation of measurements and featuring a trendline to display the observed linear relationship of the number of passes to the recorded average thickness of the films (y intercept set to zero).....104

Figure 62: SEM Images of GO films fabricated with Ultrasonic Spray Deposition with 1 pass (top) and 2 passes (bottom) after IPL Processing with an Energy Density Input of 1428 Jcm².104

Figure 63: Transparency of Rod-coated GO films deposited on TOPAS 6015 with one pulse of varying Energy Density pulses of IPL Processing versus wavelength (400 nm - 800 nm). The as deposited film (Black) displayed the highest transparency over the region. The remaining three films displayed a lower transparency values with

increased energy densities of 19.2 Jcm ⁻² (second – red diamonds), 26.8 Jcm ⁻² (third – blue squares), and 35.7 Jcm ² (forth/bottom – purple triangles).....	105
Figure 64: SEM images of as synthesized Cu(OH) ₂ NWs.	106
Figure 65: SDT of as synthesized Cu(OH) ₂ NWs with the weight% (top), first order derivative of the weight% with respect to temperature (middle), and the heat flow normalized by the weight (bottom).....	107
Figure 66: Sheet Resistance after 1744 Jcm ⁻² Incremental IPL Energy Density Input versus wt% GO in solution.	108
Figure 67: R _s comparison of spin-coated samples at concentrations of 91.53% GO (green squares) and 68.35% GO (black circles) versus IPL Energy Density Input.	109
Figure 68: R _s comparison of spin-coated 68.35% GO at the center (red squares) and over the entire samples (black circles) vs. IPL Energy Density Input.	109
Figure 69: XRD of 68.35% GO vs. IPL Energy Density Inputs of 632 Jcm ⁻² (green), 1428 Jcm ⁻² (purple), and 1744 Jcm ⁻² (red).....	110
Figure 70: SEM images of 100% GO (left) and 68.35% GO films after Incremental IPL Processing with an Energy Density Input of 1744Jcm ⁻²	111
Figure 71: Schematic for current passing through a rGO nanosheet (grey) to a Cu NW (orange) and then to another rGO nanosheet (gray), with corresponding electrical resistances shown where R ₂₃ and R ₄₅ are the contact resistances between the Cu and rGO.	111

CHAPTER 1: INTRODUCTION

The scale of energy humans consume per year is in the terawatt (10^{12}) range - ~18TW. The only renewable energy source with the potential to reach this range is solar, as the solar insolation reaching the Earth's surface to be absorbed by oceans and land is ~89 PW (or 89,000 TW). Dedication to developing solar has been adopted into policies by several governments, such as from the US DOE SunShot Vision Study in 2012 (<http://energy.gov/eere/sunshot/sunshot-vision-study>), which set a goal of solar energy meeting "14% of the U.S. electricity needs by 2030 and 27% by 2050". To meet these goals, there must be proactive investigation into technologies that increase the economic viability of solar energy conversion. The grand challenge of this dissertation is to make solar energy economical, which has been also been identified by the National Academy of Science and Engineering (<http://engineeringchallenges.org/challenges/solar.aspx>).

The bulk of photovoltaics in the market (above 90%) are based off crystalline silicon heterojunction technology that use grid of finely deposited lines of silver. Silver is traditionally used in PV manufacturing due to its inherent stability in this demanding application. The deposition of silver is accomplished using pastes followed by thermal treatment to produce conductive lines in a high throughput process.¹ It should be noted that these grids are not continuous transparent conductive films (TCFs) but rather rely on the unshaded areas between grid-lines for the passage of light. Efforts to drive down the cost of the silver include reducing silver usage through optimizing the screen printing

process and utilizing other schemes employed in the microelectronics industry. However, silver has several shortfalls as it often fails to meet the cost requirements for low value applications, especially as the demand for this currently is growing with the rise of ever-smaller electronic devices. Additionally, the photovoltaics industry utilizes approximately 10 percent of the annual worldwide silver production with double digit compound annual growth rate expected to continue for the foreseeable future.² Therefore adaption to lower cost earth abundant materials including carbon, copper, or nickel to replace silver, are necessary to achieve sustainable production and maintain positive profit margins. Figure 1 depicts the relative abundance of the elements in Earth's crust, where it can be seen that Cu and C have several magnitudes higher abundance than Ag and In.

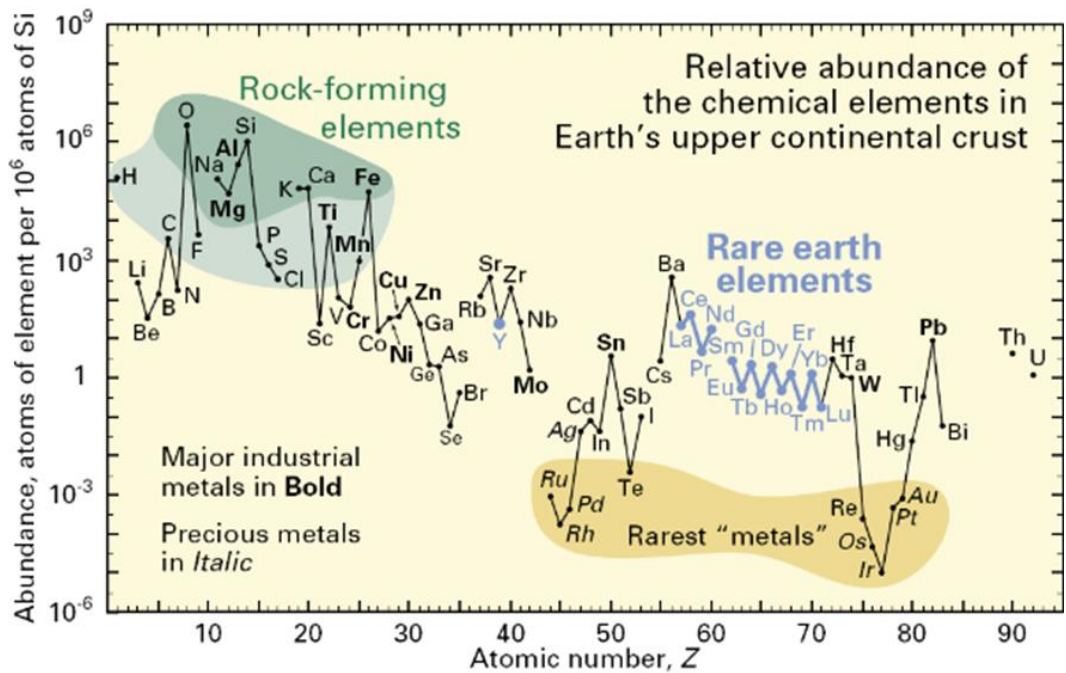


Figure 1: Relative abundance of the chemical elements in Earth's upper continental crust

(<http://pubs.usgs.gov/fs/2002/fs087-02/>)

A disadvantage to using copper as a direct replacement to silver in PV is related to its copper that diffuse rapidly in Si³, and leading to device failure/decreased performance through formation of copper-silicate⁴ at the p-n junction and lower performance due to increased recombination of the minority carriers.⁵ Methods to overcome this include low temperature deposition techniques and incorporation of diffusion barrier layers. This has been addressed in the literature through multiple investigations such as diffusion barriers for copper⁶⁻⁷, copper contamination detection⁸, and the rich chemistry of copper in crystalline silicon⁹.

Summary of challenges:

➤ Economic Challenges

The typical implementation of several materials, including Ag & In for solar can have quite significant price fluctuations over time that make it difficult to have viable costs for large scale production. Therefore, other materials are needed for enticing economic growth for photovoltaics, especially to be competitive with the cost of burning fossil fuels. The alternative materials would provide additional aid to the cost competitiveness if they are also beneficiaries efficient roll-to-roll production.

➤ Material and Chemical Use

Several solar energy technologies currently being researched utilize elements that are not Earth abundant. In addition, some of the processes required in solution phase depositions have significant environmental concerns. Thus it will necessary to research and develop more compatible mechanisms to reduce the toxicity of the types of chemistry and processes involved.

➤ Thermal Processing

Thermal processing is almost always utilized during the processing of thin films, especially those deposited as solutions, which require evaporation of solvents/organics. The heating step is often the rate limiting process and many times is accomplished in batch fashion. However, if newer technologies can rapidly evaporate of solvents/organics, reduction and sintering then it could significantly lower costs of processing and increase throughput.

A. Highlights of Engineering Opportunities for Conductive Films in Photovoltaic (PV) Applications

One field where conductive thin films are currently being implemented is photovoltaic (PV) applications. Current PV technologies include Crystalline Si (c-Si), Thin Film PV (represented as CdTe), and Organic PV, which are displayed in Figure 2. The c-Si PV technology utilize metal mesh grids that are narrowly patterned with line widths (~100 μm) to take advantage of the bare space in-between the lines for light to pass through into the device. However, Thin Film and Organic PV utilize a transparent conductive oxide, mainly Indium-doped Tin Oxide (ITO). The metal mesh grids and transparent conductive oxide could both be potentially replaced by the conductive thin films investigated in this study.

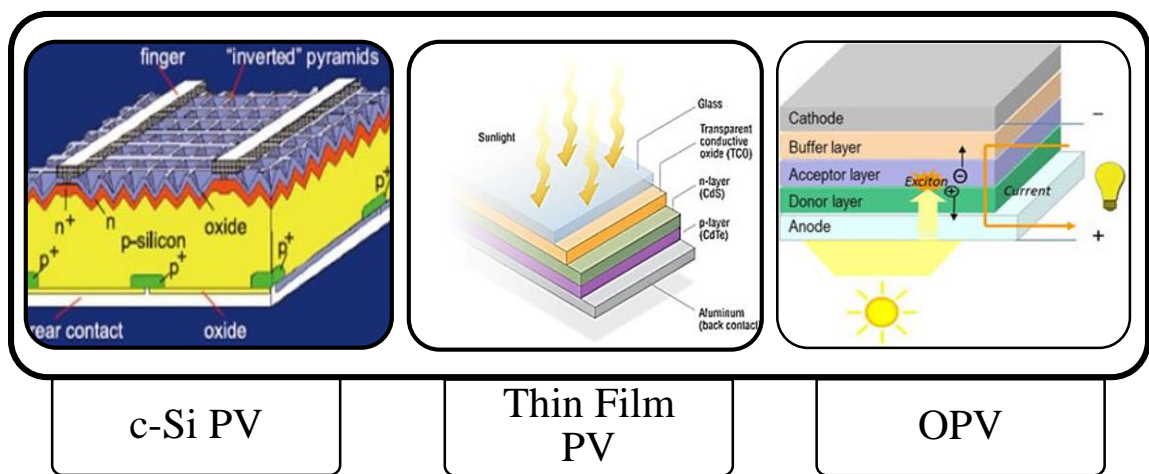


Figure 2: Structures of three types of photovoltaic (PV) cells featuring crystalline silicon (left - <http://solarlove.org/concepts-photovoltaic-technology/>), thin film technology represented by CdTe (center - <http://www.energy.gov/eere/sunshot/cadmium-telluride>), and organic (right - <http://www.energy.gov/eere/sunshot/cadmium-telluride>)

B. Motivation for study of IPL Processing Oxide & Hydroxide Forms of Conductive Precursors

In the past few years there has been an interest in the rapid sintering of nanoparticles using intense pulsed light (IPL) of non-coherent white light.¹⁰ This process, also known as photonic sintering and flash sintering, delivers rapid and high energy pulses of light to nanocomposite thin films. The absorbed light is transferred almost immediately to heat, sintering neighboring nanoparticles and resulting in a conductive film. IPL Processing is a method that rapidly delivers large amounts of energy as an incoherent light spectrum ranging from UV to visible to infrared light. The pulses are typically on the time-scale of milliseconds and over areas of tens of square inches. These approaches allow for on demand customization of the patterns and use of more affordable substrates, leading to

reduced costs of a number of fields such as photovoltaics, touchscreens, flexible electronics, flexible displays, and wearable technology.

The purpose of utilizing short light pulses instead of a constant light source is that the heating is localized into the films. Therefore, the nanomaterials can be sintered/reduced due to the heat transfer being faster than diffusion of oxygen into their crystal lattices. Additionally, the localized heating enables the use of flexible/plastic substrates as their temperature is kept low enough to prevent deformation/melting. The process differs significantly from laser sintering techniques in two distinct details 1) a much larger spectrum of light spanning from the ultraviolet (UV) to the near infrared (NIR) is used and 2) the processing area is significantly larger. Additionally, the nanoparticles can be deposited using well known traditional solution-phase printing techniques over large areas. This makes the IPL process very interesting for scalable manufacturing especially roll-to-roll production.¹¹ Conductive patterns printed using solution-based processes has the capability to drastically reduce production costs. This is especially relevant for large scale applications such as photovoltaics (PV) in which high throughput, efficient materials usage and low energy techniques are needed to reduce the overall costs. The main goal of this dissertation is to explore engineering electrical and optical properties of thin films through scalable processes and Earth abundant materials.

C. Proposed Concepts for Conductive Films via Intense Pulsed Light

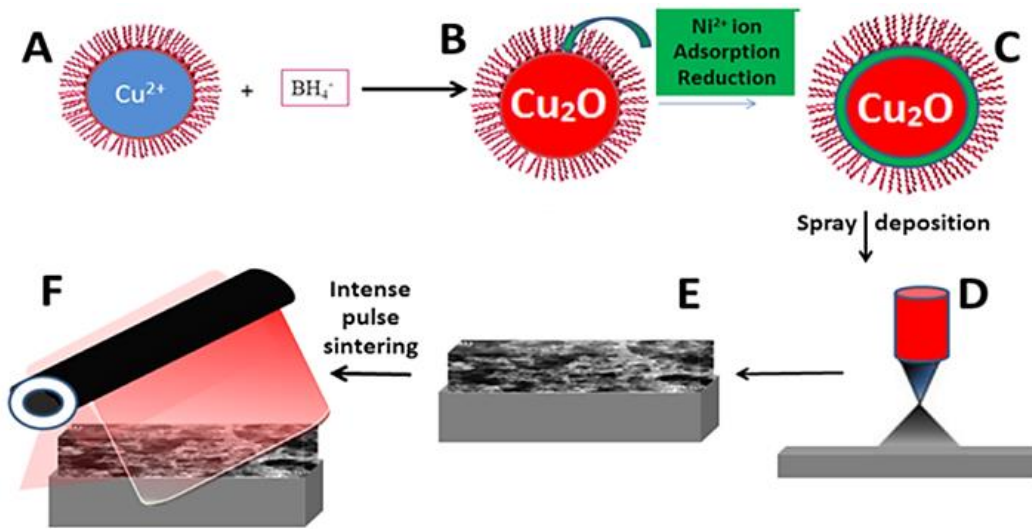


Figure 3: (A) A Cu-ammonia complex, capped with a surfactant, is formed at the start of the synthesis. (B) The complex is oxidized, forming Cu₂O nanoparticles. Ni²⁺ ions are added and adsorb on the surface of the Cu₂O. (C) Further addition of the reducing agent results in the formation of a NiO layer on the nanoparticles. (D-E) The inks are then ultrasonically sprayed on the substrate. (F) An IPL process reduces and sinters the film.

The first approach focused on how copper could potentially serve as a substitute for silver for applications like c-Si photovoltaic applications, where preventing oxidation of Cu and Cu diffusion into the Si are engineering challenges for long-term device performance. This was done through sonochemical encapsulation of Cu₂O NPs with NiO to create core-layer nanostructures, which were deposited with spray deposition and subsequently reduced & sintered via IPL Processing. (Figure 3) Ni was utilized as it has been suggested as a one of the suitable diffusion barrier layers for the Cu interface on a Si substrate and is an earth abundant material.¹² Deposition from solutions in a single step would offer a significant advantage to the deposition of conductive traces to Si substrates,

in which Cu has high diffusivity. IPL Processing had not previously implemented for core-layer nanostructure thin films.

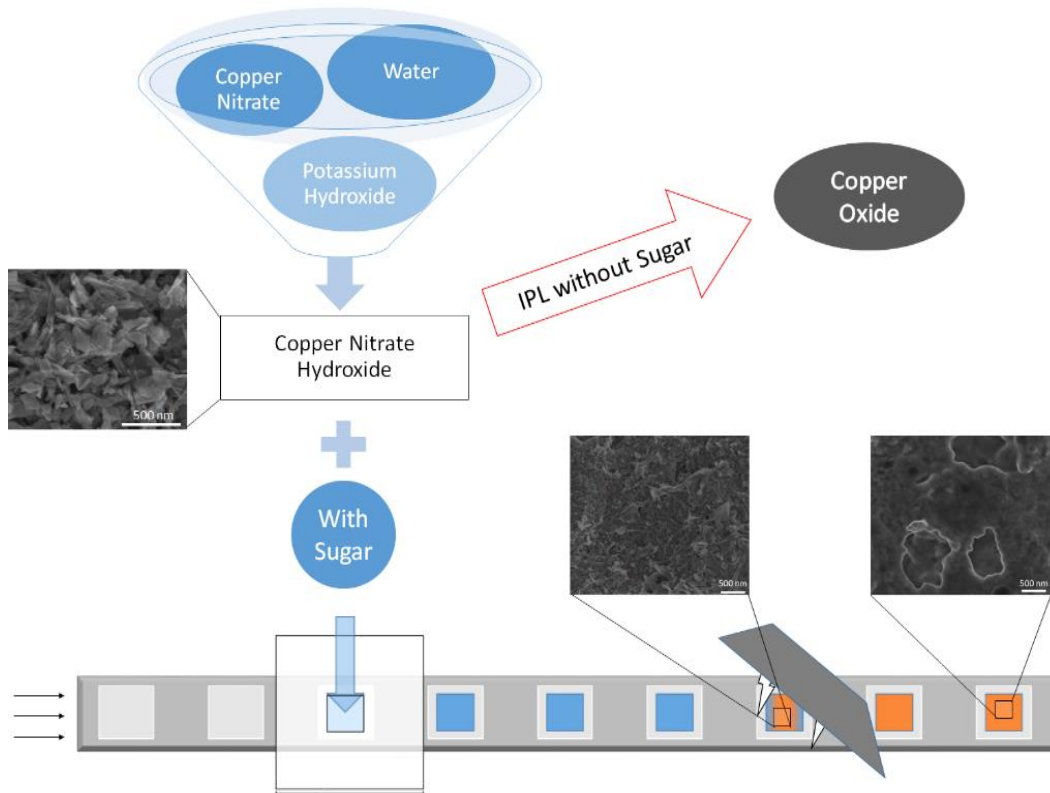


Figure 4: Overview schematic of $\text{Cu}_2\text{NO}_3(\text{OH})_3$ conversion into conductive copper from synthesis to deposition and IPL processing (featuring SEM images of the samples) envisioned for future scaled, commercial applications. The $\text{Cu}_2\text{NO}_3(\text{OH})_3$ is formed through a copper salt and hydroxide salt reaction.

The second approach expanded upon the previous work through innovating a simpler synthesis of a copper precursor with better solution stability that doesn't require the use of a harsh reducing agent and deeper exploration of organic deposition on the reducing environment induced by IPL Processing via intentional inclusion of a sugar (either fructose or glucose). (Figure 4) Depending on the desired printing method, additives could be added to the dispersion or the $\text{Cu}_2(\text{OH})_3\text{NO}_3$ could be separated from the water prior to formulation. For example, to formulate a screen printed paste, the $\text{Cu}_2(\text{OH})_3\text{NO}_3$

precipitate is mixed with the chosen organic, deposited as an additive pattern, and then subsequently IPL processed to create conductive copper.

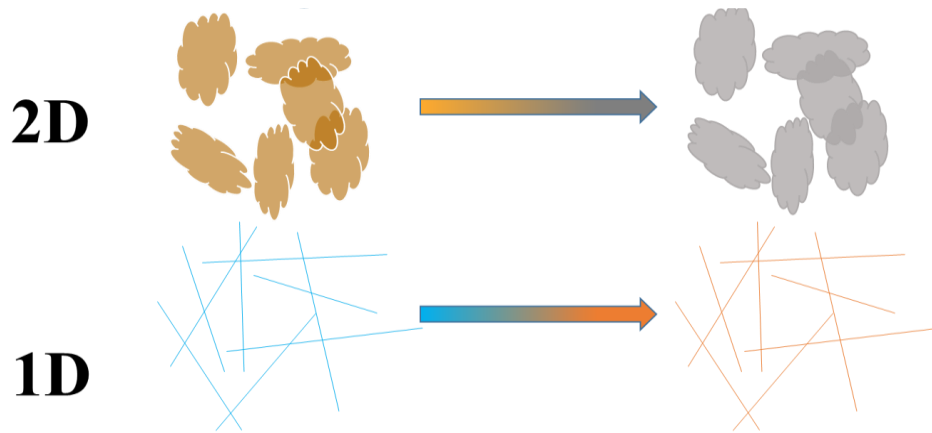


Figure 5: Conceptualization of 2D GO nanosheets and 1D $\text{Cu}(\text{OH})_2$ nanowires changing with IPL Processing

The third approach is to implement graphene oxide with copper hydroxide nanowires to be reduced via Intense Pulsed Light Processing. (Figure 5) This is significant as the first two approaches focused on addressing challenges for the metallization of c-Si PV, but have limited capabilities to address the optical transmittance demands of Thin Film PV and OPV. Graphene oxide is highly stable in aqueous solutions and when reduced, has high optical transmittance, though its sheet resistance suffers from discontinuities for large area. However, combined together with high aspect ratio Cu NWs (after the solution stable $\text{Cu}(\text{OH})_2$ is reduced via Intense Pulsed Light Processing) to help to connect the reduced

graphene oxide nanosheets, the sheet resistance of films without too great of decrease optical transmittance. (Figure 6)

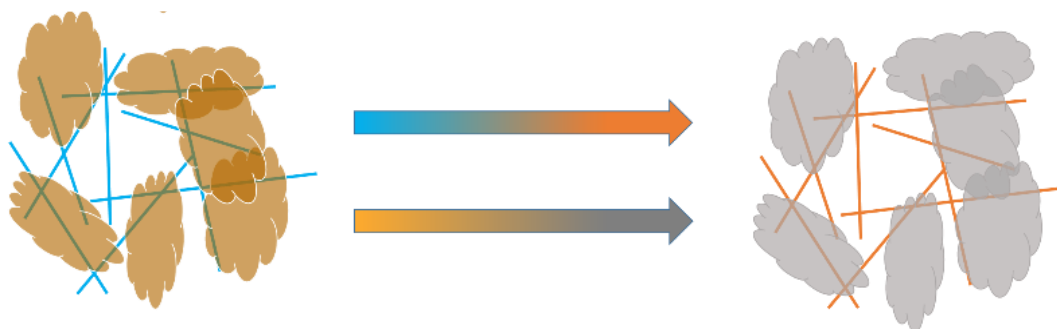


Figure 6: Conceptualization of hybridization of GO nanosheets and $\text{Cu}(\text{OH})_2$ nanowires together to create TCFs

D. Objectives for this Study of Nanomaterials & IPL Processing

The overall objective of this dissertation is to research the scalable manufacturing of conductive films overall large areas using roll-to-roll technologies. A number of state art processes require high temperatures and harsh chemicals that often add costs and limitations to substrates. Solution phase processes can address these issues, but often do not result in industrial applicable films. Specific objectives of this work are:

1. Explore the solution phase synthesis of stable oxide/hydroxide materials for large area depositions, through techniques that enable morphology and compositional control within an aqueous system.
2. Research the impact of IPL Processing as a means to reduce the deposited films rapidly, over a range of materials and morphologies.
3. Develop synergistic schemes to improve the deposition of thin films and enable the IPL technology.

4. Create thin films for flexible polymer substrates using the localized heating offered by IPL Processing.
5. Combine knowledge of single systems into hybrid films via IPL Processing.

E. Outline of Dissertation

This dissertation is comprised of eight chapters. Chapter 1 introduces conductive thin films and inks via Intense Pulsed Light and highlights importance to commercial/industrial applications. Chapter 2 reviews state of the art conductive thin films, including materials, synthesis, deposition, and reduction & processing methods. Chapter 3 describes specific experimental methods and details of the work. Chapter 4 explores an ink composed of Cu₂O nanoparticles encapsulated with a NiO layer for preventing copper diffusion into Si towards c-Si PV applications. Chapter 5 will explore the use of a Cu₂NO₃(OH)₃ based ink and how the intentional inclusion of select sugars enhances the rapid transformation into elemental Cu. Chapter 6 will describe IPL Processing of earth abundant and aqueously stable nanomaterials of 2D GO and 1D Cu(OH)₂ NWs to create conductive films. Chapter 7 will provide conclusions of the work and Chapter 8 will give recommendations for future study.

F. Impact of Dissertation

Historically, some of the first uses of nanomaterials were for uses in photography and stained glass windows and now nanomaterials are being developed to envision a vibrant and colorful picture of the future. This work is the embodiment of applying our time, intellect, and effort into assisting with at least one the great challenges we face as a society, energy. The broader impacts of the study are derived from the use of intense,

exhaustive, and deep levels of science working towards a contemporary real world solution. The application based interest people would have of things such as flexible electronics could be worn or have higher resiliency for dynamic living is incredibly high. A possible replacement of silver pastes and ITO would allow for increased commercial viability of solar cells and flexible electronics. Deeper understanding of IPL processing will allow for scalable manufacturing with reduced capital costs and commercial costs. Since the feedstocks are abundant materials, a wider array of people would have access to creating their own solutions to combatting global warming and energy deficits.

The human consumption of energy has dramatically increased in the last several hundred years, mainly through the combustion of fossil fuels. This has led to many modern innovations such as lighting, heating and air conditioning, refrigeration, medicine, transportation, computers and integrated circuits, and the internet. However, these innovations came with a cost. While our potential quality of life has greatly increased, great dangers to our existence have grown too through stronger and more efficient instruments of destruction and death, extinction of other lifeforms, imbalance of ecosystems, pollution of our air/waters/lands, damage to the ozone layer from chlorofluorocarbons (CFCs) used in early refrigeration starting in 1929 and greatly increased abundance of greenhouse gases in our atmosphere. The latter has recently crossed a threshold of the CO₂ concentration in the atmosphere breaking 400 ppm – which many deem as a point of irreversibility. With the increased greenhouse concentration comes new realities for the human race with the acidification of the oceans (through their absorption of CO₂) and disappearance of coral reefs, melting of the polar ice caps causing receding coastlines from rising ocean levels, higher average global temperatures and more

extreme & chaotic weather patterns – which is particularly prolific in the recent years’ hurricanes. For instance, in 2006 Hansen, Sato et. al stated that throughout 30 years, there was a $\sim 0.2^{\circ}\text{C}$ increase in the global surface temperature per decade.¹³

Additionally, there are inequitable disparities access to modern energy infrastructures and consumption. This can be exemplified visually by lighting seen through satellite imagery of the globe at night from NASA, which is displayed in Figure 7. Certain regions, such as Western Europe and the Eastern United States, vividly outshine most of the map despite their smaller relative population when compared to the scale of global human population. These regions consume disproportionate amounts of energy, as the populations of these regions are quite small.



Figure 7: NASA Satellite imaging of Earth at Night

The developed countries of the world have been the main consumers of energy, though the bulk (other countries) surpassed their usage in the 2000’s as seen in Figure 8 from the 2013 U.S. Energy Information Administration, International Energy Outlook. Where OECD stands for Organisation for Economic Co-operation and Development and

consists mainly of Western European countries and North America plus Japan and Australia.

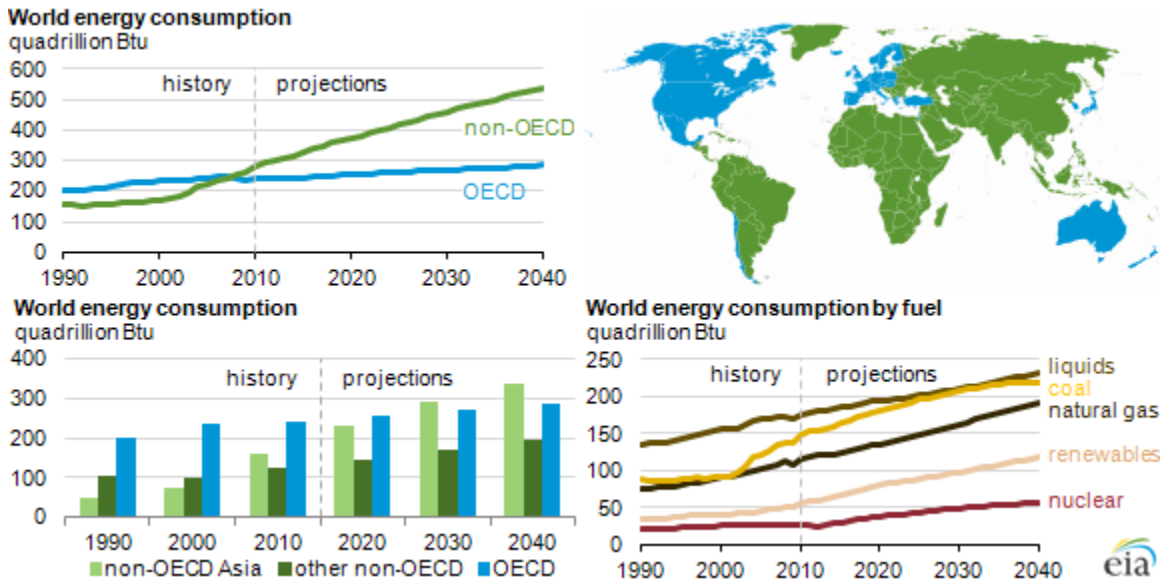


Figure 8: EIA comparison of world energy consumption of OECD and non-OECD countries

CHAPTER 2: BACKGROUND

Nanotechnology has been a great asset for development of research into sustainable solutions. Nanotechnology is defined by having at least one of the three dimensions having length of less than 100 nm. At these sizes the behavior of these nanomaterials can change dramatically from their bulk material properties. This is exemplified by the electrical conductivity of 2D sheets of carbon (graphene) and metal nanoparticles having a reduced melting point. On a broad scale, nanomaterials could also reduce the amount of material needed through extremely efficient, low-waste processes. However, the production of bulk materials for macro-scaled devices using nanomaterials often carries the requirement of downstream processing to increase the grain size and reduce losses at grain interfaces. The specific area this work has focused on is the creation of new knowledge regarding production of conductive films employing nanomaterial inks via Intense Pulsed Light Processing.

Historically, conductive networks have been dominated by metals, though nanomaterials can play a role in future developments. For starters, the production of conductive metal traces and films for electronics onto various substrates is typically accomplished through physical, vapor, and electrodeposition routes. These techniques have gained widespread acceptance in a number of applications in electronics, but often require very specific environments and have very exacting tolerances that drive up costs. This is not generally an issue for high value electronics, but can be a limiting factor for more

pedestrian applications. Recently, there has been interest in depositing these conductive patterns utilizing more versatile techniques such as screen, inkjet and aerosol jet printing and the use of non-metals that conduct electricity well. These techniques are used in a number of low cost manufacturing industries and are much more amenable to continuous processing. Quite a lot of technology has been established into the production of these inks and supported by several global companies (such as Dupont, Dow, Kodak and etc.). As the size of devices continue to shrink they require ever finer line widths and thickness, making it is apparent that incorporation of nanomaterials becomes a natural fit in formulation of inks.

To introduce nanomaterials into the ink formulations, it is important to consider that inks and pastes are designed specifically for the desired deposition technique and intended application within/as a device. Inks are composed of the functional nanomaterials but also can include multiple components such as carriers, precursors, additives and enhancements to assist with the reproducibility and precision of deposition and/or chemical transformations and/or sintering during post processing. Carriers can include solvents (to be removed by evaporation), stabilizers, binders, surfactants and viscosity modifiers. To avoid the need for extraneous/exhaustive investigation for every ink, the inclusion of precursors that exhibit higher solution stability such as an oxide or hydroxide of the conductive material are of interest. Oxide and hydroxide forms of materials are particularly advantageous for aqueous solutions due to H-bonding with the polar water molecules, leading to increased solution stability and environmentally benign processes.

Following deposition however, the conductive precursors must be reduced and/or sintered for the films to exhibit excellent electrical conductivity and performance.

Traditional methods of reduction and sintering would negate some of the aforementioned benefits of continuous processing by becoming a rate-limiting step in the process and requiring temperatures that would irreversibly damage most flexible substrates. However, there are alternative technologies to help alleviate that challenge such as Intense Pulsed Light (IPL) Processing. IPL Processing can be used in place of traditional thermal sintering¹⁴ in ovens that are typically used for sintering¹⁵ and could significantly reduce processing times¹⁶.

Certain applications (i.e. thin film or organic photovoltaics and touchscreens) have an additional need from their conductive films for device performance, known as optical transmittance or transparency. The main material currently used for transparent conductive films (TCFs) is Indium-doped Tin Oxide (ITO) as its performance on both of these aspects is substantially high. However, ITO falls short of an ideal solution due to the conditions of deposition (typically done through sputtering under vacuum), is costly to make, can have significant price fluctuations as the price of indium may change rapidly, and it is brittle – preventing robust usage and repeated bending of flexible substrates.

Two essential properties of TCFs are sheet resistance and optical transmittance. Sheet resistance, represented as R_s , is the electrical resistivity of a material over an area, providing units of Ω/\square , where $\rho_{\text{resistance}}$ = electrical resistance and t_{film} =film thickness. (Equation 1) Since the film thickness is in the denominator, thicker films lead to lower sheet resistance values.

$$R_s = \frac{\rho_{\text{resistance}}}{t_{\text{film}}} \quad \text{Equation 1}$$

Optical transmittance of TCFs are typically compared utilizing 550 nm, as the solar spectrum on Earth exhibits its maximum radiation in visible green light wavelengths.

(Figure 9) It is noted that full understanding of the optical performance requires evaluation of transmittance over the broader spectrum. Transmittance is calculated through Beer-Lambert Law, shown as Equation 2, where I_0 = initial incident of light, I_1 = resultant incident of light, α = absorption coefficient of the material and t_{film} = film thickness. As absorption coefficient is a material property, the film thickness within the exponential function becomes the key variable for obtaining a desired optical transmittance. It should also be noted that this creates a nonlinear relationship between optical transmittance and sheet resistance of films. Select state of the art materials utilized in TCF applications are displayed in Table 1.

$$T = \frac{I_1}{I_0} = \exp(-\alpha \cdot t_{film}) \quad \text{Equation 2}$$

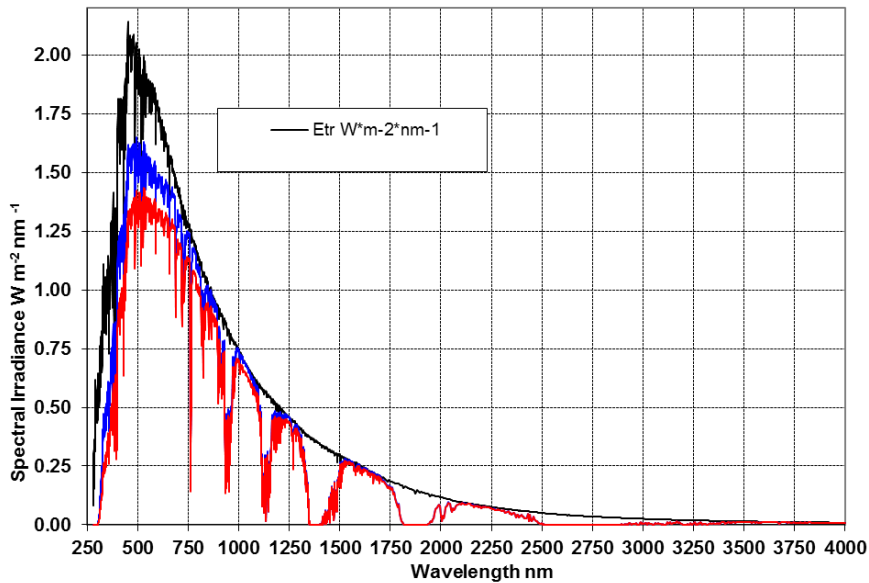


Figure 9: ASTM G173-03 Reference Spectra

Table 1: Characteristics of several TCF technologies

	Sheet Resistance (Ohm/□)	Transmittance (550nm)	Citation
Indium-doped Tin Oxide (ITO)	15.0	85%	17
	35.5	91.9%	18
Aluminum-doped Zinc Oxide (AZO)	7.85×10^3	91.84%	19
ZnO	1.88×10^5	92.20%	19
Cu Nanowires (Cu NW)	5	67%	20
	141	90%	
	9	88%	21
	17	92%	
	55	94%	
	51.8	90.9%	18
Reduced Graphene Oxide (rGO)	12.2×10^3	87.9%	17
	1.1×10^4	87%	22
	4.3×10^4	73%	23
	$10^2 - 10^3$	80%	24
	9.85×10^3	94.2%	25
	36.6×10^3	95.5%	26
PEDOT:PSS	3×10^5	98%	21
Ag Nanowires (Ag NW)	34.4	86%	17
	21.8	76.3%	25
CVD Graphene	350	90%	27
	200	85%	28
	280	76%	29
Carbon Nanotubes	2.1×10^3	72%	30
	7.5×10^2	53%	
	6.9×10^2	50%	
rGO/Ag NW	4.7	68.1%	17
Cu NW / Graphene	53.8	89.3%	18
Cu NW / PEDOT:PSS	24	91%	21
	46	93%	

Performance of transparent conductive films (TCFs) has been evaluated through a figure of merit (F_{TC}), displayed as Equation 3, and the corresponding optimal film thickness for performance, displayed as Equation 4, described by Haacke in 1976.³¹

$$F_{TC} = \frac{T}{R_s} \quad \text{Equation 3}$$

$$t_{\max} = \frac{1}{\alpha} \quad \text{Equation 4}$$

For proper understanding the performance of TCFs, it is important to incorporate the film thickness with the transparency and sheet resistance. To find the figure of merit at 90% transmissivity (ϕ_{TC}), the equations can be adjusted to Equation 5 & Equation 6 (for reference, ϕ_{TC} of ITO = .052). Where T^{10} = transparency with 10% loss and t_{\max}^{10} = the maximum film thickness for a 10% loss in transparency. The figure of merit previously described has the advantage of analyzing performance while incorporating the film thickness, it however can be difficult to use for a system with GO because the extent of reduction will affect the absorption.

$$\phi_{TC} = \frac{T^{10}}{R_s} = \alpha_{film} \exp(-\alpha \cdot t_{film}) \quad \text{Equation 5}$$

$$t_{\max}^{10} = \frac{1}{10\alpha} \quad \text{Equation 6}$$

Therefore, another 'Figure of Merit' (FOM) calculation has been utilized in the literature, for example by Kwan, Le et. al in 2016, where Z_0 = impedance of vacuum (376.73 Ω). (Equation 7)

$$FOM = \frac{Z_0}{2 * R_s * (\frac{1}{\sqrt{T}} - 1)} \quad \text{Equation 7}$$

With this equation, again the higher numbers indicate higher performance. In that same study FOM values were reported for rGO films reported in the range of .189 to 0.232,

70.0 for Ag NWs, and 134.4 to 189.9 for their hybrid Ag NW/rGO films (whereas a typical FOM value for ITO would be 297).¹⁷ FOMs of the aforementioned TCFs in Table 1 have been calculated and are displayed in Figure 10.

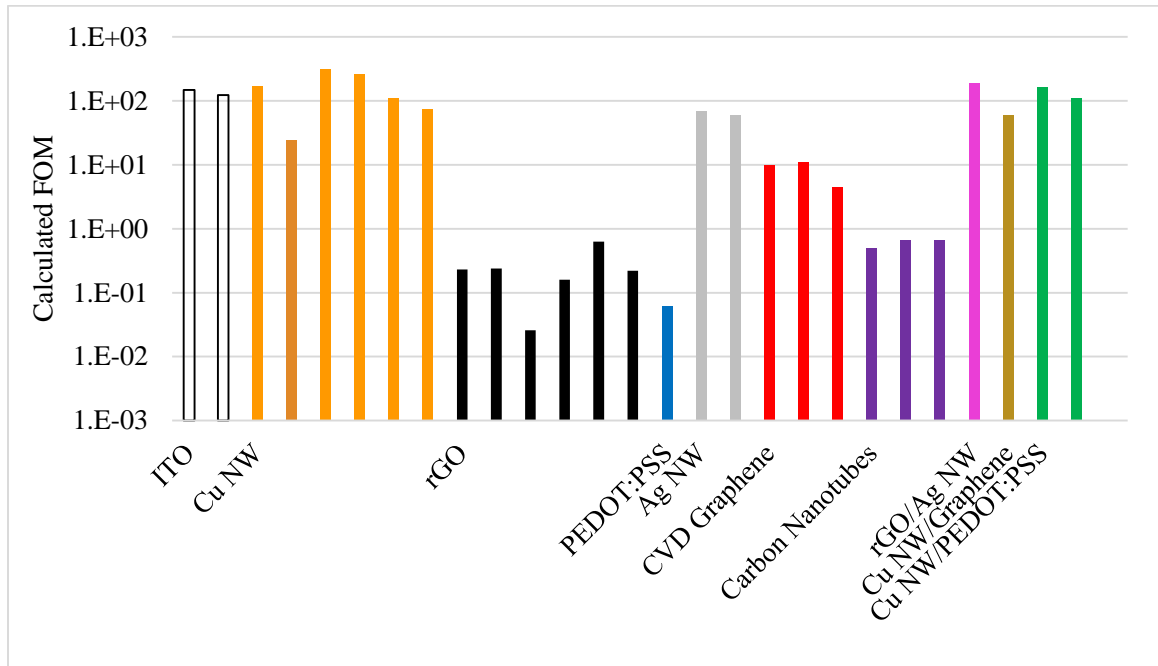


Figure 10: Calculated FOMs using Equation 7 for the TCFs referenced in Table 1

A flowchart of the remaining sections of this chapter is displayed below. (Figure 11) Firstly, Materials will be discussed, followed by the Synthesis of copper nanomaterials and graphene oxide, then by solution phase deposition, and lastly Reduction and Processing Methods.

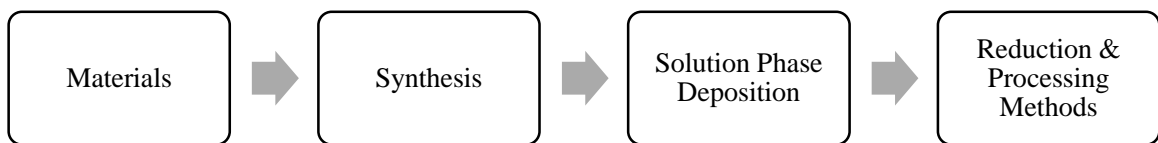


Figure 11: Flowchart of Concepts in Background Section

A. Types of Conductive Materials

1) Metal Materials and their Nanowire 1-D Embodiments

Metals are electrically conductive due their metallic bonding, where electrons are able to move as their conduction band is below the highest energy of the valance band. Nanowires (NW) made with metals are utilized for TCFs due to their morphology allowing for decreased coverage, while still maintaining excellent electrical conductivity. The high aspect ratios help to maximize the distance that the electrons can travel with a finite amount of material. Many of the studies in the literature have been conducted on Ag NWs. However, Nam and Lee in a 2016 review discussed how Cu NWs have gained attention as a substitute for Ag NWs due to advantages in cost and abundance with similarly high performance.³²

Zhu et al. (2013) created transparent electrodes with ‘self-welding’ Ag NWs through rod-coating (in two orthogonal directions) followed by a plasma irradiation treatment (75 W, 1 hr) to remove the PVP polymer coating without oxidizing the NWs³³

Sachse et al. created Cu NW transparent electrodes without the use of hydrazine in 2014 and produce an organic solar cell with 3% efficiency. The films were spray coated though not conductive afterwards. The electrodes were then subject to pressing (increased conductive performance more than it decreased transmissivity) and reduction at higher temperatures to reach these performance levels.³⁴

2) Metal Oxides Implemented as TCF Materials

Indium-doped tin oxide (ITO) is the most widely used transparent conductive film for modern applications such as touch-screens in mobile phones. The transparency of ITO

is due to the large band gap of tin oxide, which classifies it as an insulator. However, through doping with indium, the material becomes electrically conductive without losing a significant amount of transmittance. FTO is similar to ITO except it has been doped with F, to provide higher temperature stability. Aluminum doped zinc oxide (AZO) is another metal oxide that can be used for TCF applications.³⁵

3) Carbon-Based & Organic Materials

i. Graphene

Graphene, an atomic sheet of carbon, is one of the most marvelous material discoveries of the modern age and nanotechnology. Its thickness has been measured as 0.34 nm in the literature²³ and a single layer absorbs 2.3% of light, with five layers absorbing nearly 12%.³⁶ At this scale, the interlocked carbon atoms behave counter-intuitively as the material is incredibly strong, quite transparent, has displayed a potentially controllable work function³⁷, exhibits a high thermal conductive, is flexible, and is theoretically the most electrically conductive material known to man. Due to these phenomenal properties, it has inspired enthusiasm in a myriad of applications from biological sensors and cancer treatments³⁸ to supercapacitors, lithium ion batteries, light adsorbing paint, membranes, solar cells (such as dye-sensitized solar cells³⁹), displays that bend⁴⁰, and whatever the limits of our imaginations are. One current/specific application that graphene is particularly well-suited for is use as an electrically conductive and transparent material known as transparent conductive coatings (TCCs) or Transparent conductive electrodes (TCEs).⁴¹ It is noted that the notations of TCCs, TCEs, and TCFs are used interchangeably in the literature, though this dissertation focused on the use of TCFs exclusively.

Pristine graphene is grown through a chemical vapor deposition (CVD) on Cu foil.⁴² Ni foil can also be used. The graphene is grown in a furnace around 1000°C wherein a H₂/Ar environment, CH₄ is introduced. At these temperatures, the solid state diffusion of carbon into the copper crystal lattice begins to happen, as the diffusion is faster and there is a higher solid state solubility. The furnace is then cooled and depending on the cooling rate, the diffused carbon will migrate towards the surface of the carbon foil. In order to transfer these graphene films to a flexible substrate, a plastic is placed onto the graphene side of the copper foil and then the entire copper foil is etched away in a solution, leaving the graphene on the plastic without inducing significant stresses on the film.

ii. Graphene Oxide/Reduced Graphene Oxide

Graphene Oxide (GO) is a 2D material composed of bonded carbon atoms featuring oxygen-based functional groups, whose removal transitions the material to become reduced graphene oxide (rGO). (Figure 12) It is prepared through the chemical-oxidative exfoliation of graphite via the Hummer's Method.⁴³ When reduced, it becomes conductive and has prospects for use in TCFs.⁴⁴ Motivation for application of rGO is in part due to its potential as a replacement of PEDOT:PSS in polymer solar cells.⁴⁵ rGO varies significantly from pristine graphene due to the distortions of the carbon chains during the synthesis' chemical oxidation.⁴⁶ A 2016 literature article showed that GO/rGO have many potential applications ranging from TCFs and conductive inks to bio-medicine, separation membranes, energy storage, and even anticorrosion technology or fire-retardants.⁴⁷ GO exhibits fluorescence in water solutions was found to originate from e⁻s transitioning from oxidized/non-oxidized regions⁴⁸ and it has been reported that its fluorescence is pH dependent⁴⁹. For bio-medical applications, there have been articles looking at how the

toxicity of GO is based on the oxidative method for synthesis⁵⁰ and how it could affect brain function⁵¹.

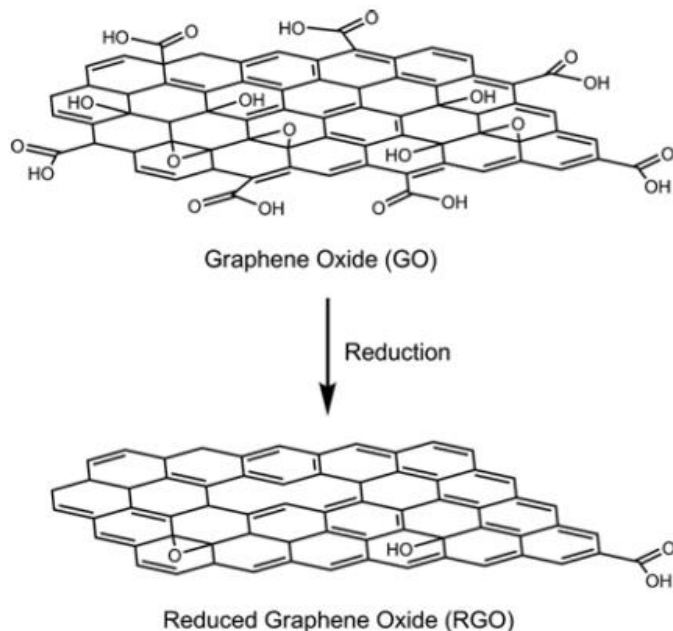


Figure 12: Illustration of chemical structure of GO and rGO post-reduction⁵²

GO can either be deposited and subsequently reduced or reduced prior to deposition. For example, An, Kim et al. in 2015 inkjet printed rGO, obtaining a resistivity of $.0013 \Omega \cdot \text{m}$.⁵³ A typical rGO film with a 550nm transparency of 94% has a sheet resistance of $49.2 \text{ k}\Omega/\square$.⁵⁴ In 2016, Wei, Yu et al. observed electron hopping in rGO.⁵⁵ During the deposition of GO films, it is very important that the GO sheets are left in a flat orientation and sheet stacking is minimized. One cause of stacking GO sheets is interstitial water molecules between the sheets, as large amount of water is absorbed to the sheets⁴⁶ and has been shown to cause stacking.⁵⁶ Sheets that are deposited as a single layer provide lower sheet resistance and higher transparency. Within the literature, there are several approaches to overcome this challenge such as adjusting hydrophobicity or hydrophilicity

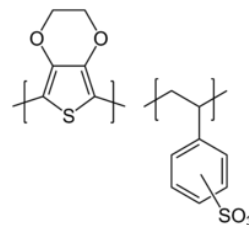
with a surfactant and modification of pH,⁵⁷ capillary force driven self-assembly at liquid-air interfaces to make GO thin films,⁵⁸ spin-coated sol-gel silica and GO composites,⁵⁹ Meyer-rod surface tension driven flat deposition of rGO,⁶⁰ Langmuir-Blgett adsorption,⁶¹ and altering the GO sheet sizes⁶²⁻⁶³. Doping surface bonds of GO can also be modified with reagents (such as SOCl₂).²³

iii. Carbon Nanotubes

Carbon nanotubes are sp² carbon ring based nanomaterials that are essentially rolled-up sheets of graphene. They can be multi-walled (with several layers) and have varying diameters. They have been studied in the literature as thin films deposited by rod coating⁶⁴ and spray coating³⁰, as two examples.

iv. PEDOT:PSS

Organic molecules can conduct electrons when an electron is excited from its highest occupied molecular orbital (HOMO) to its lowest unoccupied molecular orbital (LUMO).



A widely used conductive copolymer is poly(3,4-ethylenedioxythiophene):polystyrene sulfonate (PEDOT:PSS). **Figure 13: Structure of PEDOT:PSS**

The transparency of this material comes from the organic bonds absorbing light mainly in the infrared region of the electromagnetic spectrum. It is fabricated as a copolymer to assist with its solution stability in polar solvents, such as water, through the SO₃ functional groups contributed by the incorporation of polystyrene sulfonate. The use of an organic TCF is highly preferable for organic light emitting diode (OLED) and organic photovoltaic (OPV) applications. They are also advantageous for future roll-to-roll processing on

flexible plastic substrates, as they do not require ample post-processing to become conductive and are chemically similar to the plastic substrates themselves.

4) Hybridization of TCF Materials

Hybrid technologies are combinations of technologies to overcome a challenge for specific applications, such as greater flexibility or lower cost. Performance of these hybrids can depend on lattice defects and grain boundaries.⁶⁵⁻⁶⁶ Layani et al. in 2014 discussed materials/structures for TCFs, mentioning some hybrid structures, which could potentially rival ITO.⁶⁷ One consideration for proper understanding of hybrid schemes is to also take into account how materials interact with themselves first, for example Cu NWs inter-NW resistance has been studied in the literature.⁶⁸ Another consideration for hybrid devices is that they are electrically compatible materials whose band gaps/work functions have good alignment. This leads to Ohmic contacts, if the difference is less than .3eV, with minimal contact resistance. In 1977, Michaelson reported the work function the elements as C – 5.0 eV, Cu – 4.65 eV, Ag – 4.26 eV, and Au – 5.1 eV.⁶⁹

Copper NWs were combined by Kholmanov et al. in 2013 to create hybrid structures though the copper nanowires were spray coated and then graphene oxide was deposited with spin-coating separately (treated with hydrazine vapor for 24 hours and annealed at 400°C for 4 hrs under 5% H₂) and dry transferred with PMMA onto the NW film. Hydrazine used to prevent oxidation of the purchased NWs. The films also showed a beneficial behavior of reduced sheet resistance loss when left at 60°C in ambient atmosphere, increasing their stability so the use in commercial applications is more viable.²⁶

Kwan, Le et al. utilized spray coating to deposit layers of Ag NWs followed by spray coating rGO and were able to show that the rGO coated Ag NWs exhibited better survivability under conditions which would normally lead to oxidation, resulting in increased resistivity.¹⁷ Kholmanov, Stoller et al. created spin-coated TCFs with Ag NWs and gold rGO.⁵⁴ They found that the Ag NWs had Ag NW / Ag NW contact resistance junction of 61 Ω and 77 Ω . Mayousse, Celle et al. in 2014 utilized hydrothermally synthesized Cu NWs that were subsequently covered by a 50 nm spin-coated PEDOT:PSS layer to create flexible TCFs with a sheet resistance of 55 Ω/\square . at 94% transmittance.²¹ They also applied an acid treatment with glacial acetic acid, which helped to remove both the octadecylamine and surface oxide to improve performance and enable Ohmic contact. Additional examples of hybridized TCFs are graphene w/ PEDOT:PSS⁷⁰, metal NWs with CVD graphene⁷¹, Graphene on metal grids⁷², GO and polymers⁷³, graphene-silica composites⁵⁹, rGO and Ag NWs films⁷⁴, graphene-stabilized copper nanoparticles⁷⁵, and GO-Ag nanoparticles⁷⁶.

B. Solution Phase Synthesis of Earth Abundant Precursor Nanomaterials

1) Solution Phase Synthesis of Copper Nanomaterials

Copper NPs have gained momentum due to their potential as a replacement of silver in printed electronics.⁷⁷ Syntheses have been conducted with various techniques including chemical reduction (such as with NaBH_4 ⁷⁸⁻⁷⁹, hydrazine⁸⁰⁻⁸¹ and L-ascorbic acid⁸²), polyol⁸³⁻⁸⁵, microwave assisted polyol⁸⁶⁻⁸⁷, alcohol reduction⁸⁸, electrochemical deposition⁸⁹, electrolysis⁹⁰, hydrothermal⁹¹⁻⁹², metal vapor⁹³, photochemical⁹⁴, reverse micellar synthesis,⁹⁵⁻⁹⁶ sonochemical⁹³, thermal reduction⁹⁷ and thermal decomposition of

a precursor⁹⁸⁻⁹⁹. Additionally, there are two reports for the synthesis of Cu₂O@NiO core-layer nanostructures grown using a heated bath containing a solution of mixed metal salts. As a result, core-layer structures with diameters less than 100nm were formed, with a Cu-Ni alloy interface.¹⁰⁰⁻¹⁰¹

The synthesis of metal NWs is typically done through a polyol method, which incorporated PVP as a driving force for one directional growth and to form a thin outer layer on the NWs, protecting them from oxidation. In 2005 Chang et al. created copper nanowires by reacting hydrazine with a Cu(NO₃)₂ and NaOH in the presence of ethylenediamine (EDA), which formed complexes with the copper ions and aided in the formation of the nanowires. They found that a high amount of NaOH was necessary to prevent the formation of copper hydroxide. The EDA was needed to limit the morphology growth as nanoparticles were made if it was too low. However, if the concentration of EDA was too high, nanowires were not formed and rather the synthesis created 2D nanodisks.¹⁰²

Liu et al. in 2003 were able to avoid the harsh reducing reagents while synthesizing Cu NWs through hydrothermal synthesis of copper nanowires was performed by by complexing the aqueous Cu²⁺ ions with glycerol prior to reacting with OH⁻ and HPO₃²⁻. Glycerol was added as 40% vol for the reaction and to increase the viscosity; resulting in a higher NW stability. Reaction times however, were 20 hours.⁹² Shi et al. in 2005 implemented a hydrothermal reaction taking 48 hours utilizing octadecylamine as a capping agent.¹⁰³ Cu NWs were also produced by Jin et al. in 2011 by using hexadecylamine as a capping agent and glucose as the reducing agent for 6 hours at 100°C.¹⁰⁴ Zheng, Liang et al. in 2014 proposed that the wastewater from Cu NWs

syntheses, still containing ethylenediamine and concentrated NaOH, can be reused for the synthesis after removal of the produced Cu NWs by addition of more hydrazine and ethylenediamine to help alleviate challenges associated with scaling the synthesis of Cu NWs.¹⁰⁵

There are also multiple investigations into the synthesis of copper oxide nanomaterials with methods such as aqueous reduction method through the use of a NaBH_4 ¹⁰⁶ or sonochemical Synthesis CuO ¹⁰⁷. Cupric and cuprous oxide NWs were created by Sunkara, Vendra et al. in 2013 with a wet chemical oxidation (with hydrogen peroxide and ammonium bisulphate) of copper foil under basic conditions to create $\text{Cu}(\text{OH})_2$ NWs and then subjected to oxidation with atmospheric plasma. The application to photoelectrolysis was also investigated and showed higher performance than with thin films.¹⁰⁸ Cu_2O NWs were prepared by Orel, Anžlovar et al in 2006 with copper acetate and diethylene glycol reacting at 190°C for 6 hours.¹⁰⁹

Copper Hydroxide, $\text{Cu}(\text{OH})_2$, is sometimes used as a template for creation of CuO or Cu NWs. However, other morphologies can be obtained such as leaf-like structures.¹¹⁰ $\text{Cu}(\text{OH})_2$ NW bundles were created by Li et al in 2010 in an aqueous mixture of $\text{Cu}(\text{NO}_3)_2$ and NaOH with PEG200 (polyethylene glycol 200) directed Growth at ambient conditions in 4 hours. The $\text{Cu}(\text{OH})_2$ transformed into CuO if the reaction was left to go on for 8hrs.¹¹¹

Copper Nitrate Hydroxide (CNH) can also be produced, typically through reacting copper nitrate and sodium hydroxide or potassium hydroxide. To produce $\text{Cu}_2\text{NO}_3(\text{OH})_3$, rather than CuOH_2 , the molar ratios and time of reaction are changed. The coppers are coordinated through either two OH^- groups or an OH^- group and a NO_3^- group.¹¹² In 2004, Park and Kim created unidirectionally aligned $\text{Cu}(\text{OH})_2$ nanorods from a two dimensional

copper hydroxyl nitrate.¹¹³ $\text{Cu}_2\text{NO}_3(\text{OH})_3$ has been synthesized in various morphologies such as microcrystals¹¹⁴, nanoplatelets¹¹⁵, and nanorings¹¹⁶.

2) *Graphene Oxide (GO) Synthesis Methods*

GO is typically produced with a modified hummer method, which was originally published by Hummer and Offeman in 1958⁴³. Although, there are methods which date back to from 1939¹¹⁷ and 1898¹¹⁸. The method chemically exfoliates graphite through utilization of strong oxidation reagents and features a reaction between H_2SO_4 and KMnO_4 .¹¹⁹ There are several modifications to the original method and recommendations in the literature, such as Marcano, Kosynkin et. al. in 2010 who discussed that the synthesis of GO could be improved from the typical Hummer's Method by excluding NaNO_3 and increasing the KMnO_4 molar ratio.¹²⁰ Centrifugation separation is typically used to cleaned-up and isolate the reaction's product of high quality GO.¹²¹ Removal of 'oxidative debris' after synthesis has also been shown to help produce higher quality GO.¹²²

C. Solution Phase Deposition

1) *Ink Formulation to Enable Solution Phase Deposition*

For formulation of inks, the main considerations are the concentration of solids, choice of solvent(s), and the addition of selected additives. The surface tension and viscosity are two important properties of an ink. The shear rates will vary between deposition methods. The magnitude of the shear rates will indicate the potential for control over factors (such as film thickness and orientation of materials) of that deposition method.

2) Importance of Substrate Choice on Film Deposition

Each type of substrate will have a different surface energy. The surface energy of the substrate will affect film wetting. The surface energy can be decreased through use of surface treatments. One vastly used technique is oxygen plasma treatment, which significantly reduces the surface energy of substrates. Substrates are chosen for a variety of reasons however, depending on the application and processing therein. For instance, if a high temperature sintering process is needed then a plastic substrate would not suffice. For glass, the two main types are borosilicate, which has a better thermal coefficient of expansion, and soda-lime glass that has higher optical transparency and is more favorable for aqueous inks (due its higher polar interactions of surface energy). For plastics, polyethylene terephthalate (PET) is typically the choice as it has a relatively high glass transition temperature $\sim 150^{\circ}\text{C}$. There are additional options however, such as a cellulosic based plastic (like TOPAS 6015). Plastic substrates are being widely explored as they enable flexible application, are typically lower cost, and roll-to-roll continuous processing.

3) Solution Phase Deposition Methods

For spin-coating, a small amount of the ink solution is placed onto the substrate, covering the surface. The substrate is then rotated at high rotations per minute (rpm), typically ranging from 1,000 rpm to 5,000 rpm. It is noted that spin-coating is difficult to scale for large area coatings as it typically has a high amount of materials waste (above 90%), becomes increasingly sensitive to surface disconformities, and is a batch process. Screen printing utilizes high viscosity pastes typically ranging from 10^2 - 10^5 centipoise (cP). The higher viscosities are essential for control of patterns.

Ultrasonic spray deposition is an improved deposition method of typical spray technique. The utilization of ultrasonic nozzle to induce droplet atomization, combined with air jets, allows for a high level of control. (Figure 14)

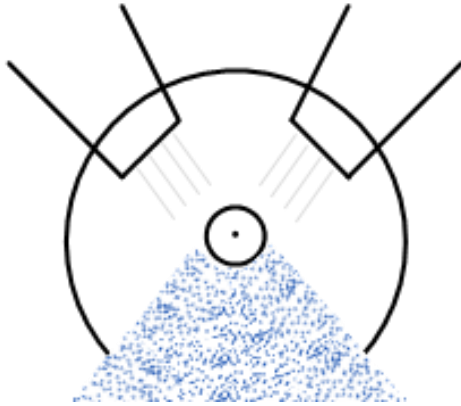


Figure 14: Depiction of Ultrasonic Spray Deposition

The governing equations for Ultrasonic Spray Deposition have been described by Majumder, Rendall et. al. in 2010 for single walled carbon nanotube films, showing how the processing parameters can be optimized to control droplet drying time to improve quality of films.³⁰

Rod-coating (or the Meyer Rod technique) is based upon the inks being confined to a small region/volume by a spiraled rod (around the main cylinder), as seen in Figure 15. The evaporative forces and surface interactions help to control deposition. The diameter of the rod is a crucial variable to the resulting film thicknesses (there are upwards of 90 to choose from). Other variables and ways to control the deposition process include the solution concentration, choice of substrate, substrate surface modification treatments, doping of the pre-deposited graphene oxide material, and choice of solvent(s). Rod-coating has been utilized in the literature for depositing GO, for example in 2012 by Wang, Liang et al., where they also modeled how to calculate the drying time and thickness of films.⁶⁰

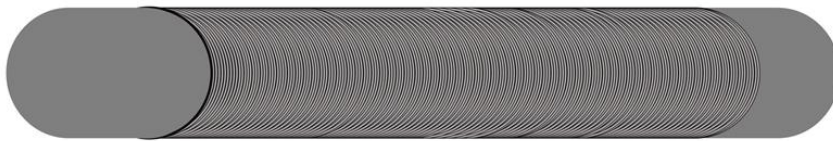


Figure 15: Depiction of a Rod-coating tool

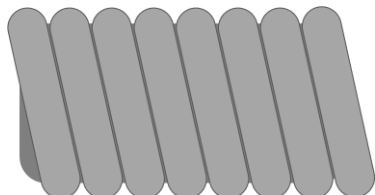


Figure 16: Depiction of close-up of the spiraled rod of a Rod-coating tool

D. Reduction and Processing Methods

Intense pulsed light (IPL) Processing has been utilized as a rapid and scalable technique to accomplish the heat treatment.^{11, 123} IPL is an emerging advanced manufacturing process that illuminates light from a xenon strobe over a wide area, which induces localized temperature increases.¹²⁴ The IPL process is particularly advantageous as an alternative method of sintering metal nanoparticles, as the rapid pulses would significantly reduce processing times¹⁶ and is applicable to flexible substrates¹²⁵⁻¹²⁶, which would be irreversibly damaged by traditional thermal sintering¹⁴. Sintering is the process of combining particles (typically metal powders) into a bulk or porous structure without the need to completely melt the material through solid state diffusion.¹²⁷ There are several in-depth studies of IPL sintering mechanisms in the literature including nucleation through flash sintering¹²⁸ and nanogranulation of metal alloy on carbon nanotubes¹²⁹.

IPL processing has been used predominately for the sintering of metals such as gold¹³⁰⁻¹³¹, Nickel (Ni)¹⁰, Ag¹³²⁻¹³⁷, and Cu^{91, 106, 138-141}. There are various examples in the literature of IPL Processed with multiple variations of types of ink compositions and

morphologies such as Ag micro-flakes with resin¹⁴², Ag NWs¹⁴³, Ag NWs for touch pads¹⁴³ Ag NWs¹⁴⁴, Ag NWs on polymer substrates¹⁴⁵, ‘strongly adhesive’ Ag NWs¹⁴⁶, Ag on different substrates¹³⁷, Ag nano-ink¹³³, Ag NWs w/ Graphene Encapsulation¹⁴⁷. Outside of metals, additional materials have been studied in the literature including semiconductors such as CdS¹⁴⁸⁻¹⁴⁹ and CdTe^{148, 150}, CoO/Nickel nanoflakes¹⁵¹, photo-oxidation of Silicon¹⁵², and Si NPs¹⁵³ and also for annealing graphene¹⁵⁴. IPL processing has also been used for direct integration with solar cells such as creating a Cu(In,Ga)Se₂ alloy¹⁵⁵, processing a CuIn_{1-x}Ga_xSe₂ ink for gravure printing¹⁵⁶, CIGS Particles¹⁵⁷, dodecylamine capped CIGS NPs¹⁵⁸, perovskites¹⁵⁹, and buffer layers for organic photovoltaics.¹⁶⁰

Song, Han et al. in 2016 showed that masked IPL processing of Ag NWs or Cu NWs films on transparent polymer films could be used to selectively pattern the NWs due to the increased adhesion during processing.¹⁶¹ They also studied how the sheet resistance of films changed with use of different pulse durations (500, 1000, and 2000 microseconds) and found that 500 microsecond pulse durations with a three second interval between pulses didn’t cause thermal damage to the films and their sheet resistance was maintained.

IPL processing of copper nanoparticles has enabled the sintering of copper, without the use of an inert environment or vacuum because the time-frame of heating and cooling is faster than the oxidation of the copper.¹³⁹ Forgoing the use of inert environments and vacuum processes is enticing for scaled manufacture due to the associated costs. IPL sintered copper nanoparticles have shown very good conductivities¹⁶ and sintering/melting at 318°C¹⁶². Utilizing inks with metal nanoparticles decreases the required sintering temperature, due to the increased surface to volume ratio of the particle and quantum confinement, resulting in the particles having a low melting point temperature. This

phenomenon has been reported for a number of nanoparticles, including gold¹⁶³ and copper⁹¹. However, the solution stabilized copper nanoparticles were susceptible to oxidation and agglomeration.

To counter oxidation, the synthesis/deposition of copper nanoparticles used harsh reducing agents of hydrazine¹⁶⁴ and sodium borohydride^{78, 106}. Additives such as PVP⁸⁵ or CTAB¹⁶⁵ can increase the solution stability and control the particle size of the copper nanoparticles, but there is an inherent tradeoff when adding large molecules and polymers on the resulting porosity/conductivity of IPL processed films.¹⁶⁶ To overcome the agglomeration and oxidation challenges of copper during synthesis and deposition, it is advantageous to use cuprous oxide^{106, 167}, cupric oxide¹⁶⁸, or copper salts/complexes such as Cu ion inks¹⁶⁹, Cooper Nitrate Hydroxide¹⁷⁰, and Copper Carboxylate¹⁶⁶. During IPL Processing, decomposition of organic molecules has been shown to induce a reducing environment. (Table 2)

Table 2: Selected examples of organic decomposition during IPL Processing

Material	Organics	Reference
Cu (native Cu₂O shell)	PVP	91
Cu₂O	Tergitol and ethylene glycol	106
Cu₂O@NiO	Tergitol and ethylene glycol	167
Cu₂NO₃(OH)₃	Fructose or glucose	170
Cu(HCOO)₂, Cu(CH₃COO)₂ Cu(C₁₇H₃₃COO)₂	Metal-organic copper complex	171

Reduction of GO to rGO is an exothermic reaction that releases CO₂, H₂O, and CO.⁵² Typical reduction methods of graphene oxide films involve high temperature vacuum annealing and/or use of chemical reducing agents.¹⁷²⁻¹⁷³ Temperatures needed to remove most/all of the oxygen functional groups are above 1000°C.^{60, 174} Chemical

reagents include hydrazine^{63, 175}, NaBH₄⁶², N,N-dimethylacetamide¹⁷⁶⁻¹⁷⁷, metals¹⁷⁸ (such as Al⁷⁴ and Cu¹⁷⁹), HI acid¹⁸⁰, ascorbic acid (Vitamin C)¹⁷, alkaline conditions¹⁸¹, glucose¹⁸², hydrothermal ‘green’ reduction¹⁸³. There have been a few examples in the literature which explore photoreduction methods such as UV Light Pulses¹⁸⁴, pulsed laser radiation of a solution containing ammonia¹⁸⁵, camera flashes^{52, 186}, sunlight compared to UV light and a laser¹⁸⁷, and UV-assisted in TiO₂ suspension¹⁸⁸.

IPL processing reduces GO films directly with UV light and by increasing the thermal energy. The ability of GO to absorb light increases as it reduces.⁴⁴ The increased absorption occurs due to the reformation of π - π bonds, which have higher energy, red-shifting the absorbance. Qualitatively, the reduction’s progress can be seen by a visual transformation of films from yellowish-brown to black. Quantitatively, this can be captured experimentally with UV-Vis spectroscopy. The increased absorbance of GO during reduction is advantageous for IPL processing; as sequential IPL pulses will be more effective in contributing to the reduction. Literature values have reported that wavelengths below 520nm are required to contribute to reducing GO directly.⁷⁶

Raman spectroscopy is utilized to characterize carbon-based materials to help differentiate them (i.e. graphite, graphene oxide, reduced graphene oxide, and graphene). Raman spectroscopy is useful in this work for identifying GO’s extent of reduction¹⁸⁹ and the number of layers¹⁹⁰. The main indicators are the defects (D) peak ($\sim 1350\text{ cm}^{-1}$) and graphite (G) peak ($\sim 1580\text{ cm}^{-1}$).¹⁹⁰ The D peaks are representative of defects (like grain boundaries),¹⁸⁹ while the G peaks are characteristic of carbon materials. However, it should be noted that the laser wavelength utilized for excitation will alter the spectroscopic response of GO/rGO.

FTIR can show diminishing oxygenated-functional Groups epoxides, carbonyls, alcohol's, aldehyde's and carboxylic acids. XPS allows for analysis of the carbon to oxygen present in molecular bonds (~30% oxygen as synthesized GO) and how the carbon to oxygen ratio increased as GO is reduced.⁵⁶

Al-Hamry, Kang et. al. in 2016 utilized IPL processing on ~15-70 nm thick spin-coated GO films and their findings of the reduction compared to traditional thermal treatments at 200°C and 400°C are displayed in Table 3.¹⁹¹

Table 3: Comparison of thermal and IPL Processing reduction of GO¹⁹¹

	Sheet Resistance (Ω/\square)	Transparency (550 nm)	C/O ration	I _D /I _G ratio
As dep GO		93.2%	1.5	1.45
200°C	199 x 10 ³	69.5%	1.7	1.7
400°C	203 x 10 ³	79.4%	2.3	1.1
IPL	178 x 10 ³	67%	3	1.1

Park, Kim et. Al. in 2015 deposited GO through filter-deposition to create ~.5 μ m thick 'self-standing' GO films, which was IPL Processed with 1-5 pulses (5-20ms duration) and total energy densities of 20-40 Jcm⁻², resulting in sheet resistances 17.55 Ω/\square – 78.78 Ω/\square . and analyzed the presence of monolayer rGO vs. multilayer rGO by the XRD peak ratio at 24.7° (002) to 43.4° (100).¹⁹²

Arapov et al. in 2016 photonically annealed binder-based graphene inks and subsequently implemented compression rolling, which helped increase the conductivity of their films as the proximity of the graphene sheets was reduced resulting in 1.4 Ω/\square , with a 25 μ m thick film.¹⁹³

CHAPTER 3: EXPERIMENTAL

In this chapter, the synthesis methods are described for each of the four nanomaterials studied in this dissertation, followed by deposition methods and IPL Processing.

A. Solution Phase Synthesis of Cu₂O-NiO core-layer Nanostructures

Commercially available Tergitol NP-9 (Sigma Aldrich, 99%) was used as the capping agent for the synthesis of the copper oxide nanoparticles. Anhydrous copper nitrate (Cu(NO₃)₂, Alfa Aesar, 99.99 %), nickel nitrate hexahydrate (Alfa Aesar, 98 %), ethylene glycol (C₂H₆O₂, Alfa Aesar, 99.5%), sodium borohydride (NaBH₄, Sigma Aldrich, 98%) and ammonium hydroxide (Fisher Scientific, 29.18 %) were used in the synthesis of the Cu₂O-NiO core-layer nanostructures.

The synthesis of a copper dispersion by the reduction of Tergitol capped Cu²⁺ ions using NaBH₄ solution has been described in an earlier work.¹⁰⁶ For the synthesis, 5 ml of Tergitol NP-9 was added to a 50 ml aqueous solution of 0.1 M Cu(NO₃)₂, followed by 100 ml of Ethylene glycol. The pH of the solution was adjusted from pH 7 to 11 by the drop-wise addition of NH₄OH. To this solution, 50 ml of aqueous NaBH₄ (0.05 M) was added and the reaction was then stirred for 2 h in an inert atmosphere. The Cu₂O nanoparticles in the form of a black precipitate were isolated by centrifugation at 5000 rpm for 5 min. Although a black precipitate was observed, CuO peaks were not observed in the corresponding XRD characterization. 1.5 g of as obtained Cu₂O nanoparticles was

dispersed into a 25 ml solution of acetone and nickel nitrate hexahydrate ($\text{Ni}(\text{NO}_3)_2 \cdot 6\text{H}_2\text{O}$) (1 mM, 5 mM, 10 mM and 20 mM) under ultra-sonication at a power of 10 Watt for one hour. Further, 25 ml of an aqueous solution of NaBH_4 (1 mM, 5 mM, 10 mM and 20 mM) was added to the respective solution and sonicated for one hour. It has been noted that the NaBH_4 concentration for reduction of the metal ion is two-fold higher than the required concentration, in order for the excess H_2 released by the decomposition of NaBH_4 helping to maintaining the reduction media and reducing the formation of surface oxide, as shown in our previous report.¹⁰⁶

By adjusting the concentrations of the reducing agent, NaBH_4 and capping agent, Tergitol, to control the diameter. These nanoparticles were synthesized in a water/glycol (1:1 v/v) solvent (Figure 4A) and were capped with a layer of Tergitol (Figure 4B). The Cu_2O nanoparticles were then isolated from the solvents used during the synthesis and subsequently re-dispersed in a solution of acetone and $\text{Ni}(\text{NO}_3)_2$. Due to the solubility of Tergitol in acetone, Ni^{2+} ions were directly adsorbed on the surface of Cu_2O particles (Figure 4C). To facilitate complete adsorption of the nickel ion on the cuprous oxide nanoparticles, the solution was then ultrasonically mixed for 1 hour under atmospheric conditions.

An aqueous solution of NaBH_4 was then added to the solution and was ultrasonically mixed for another hour. Initially the introduction of a reducing agent resulted in the formation of a Ni coating (Equation 8). However, the energy supplied to the system during ultrasonication in the presence of oxygen resulted in the oxidation of this coating (Equation 9). XRD, SEM and TEM results have all shown that no other Cu or Ni species (metal borides) were present in the final product. The concentration of the $\text{Ni}(\text{NO}_3)_2$ was

adjusted between 1 mM and 20 mM to control the thickness of the Ni layer. These core-layer nanostructures are the oxides of Cu and Ni (Cu₂O@NiO) and are reduced during the IPL process. To make a film using these core-layer nanostructures, the dispersions are spray deposited onto a silicon substrate followed by intense pulsed light sintering (Figure 3 D-F).

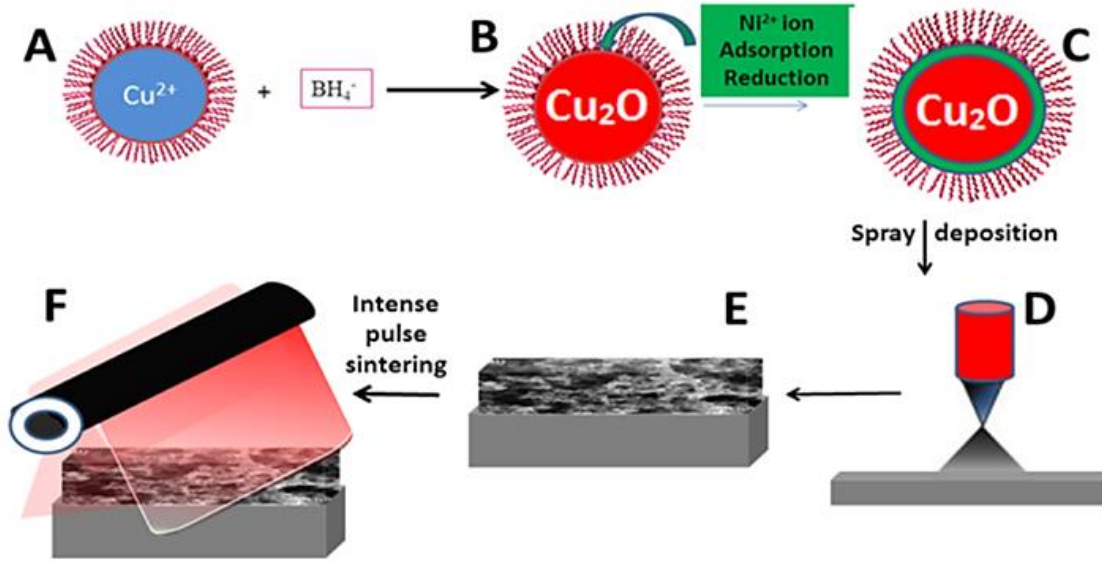
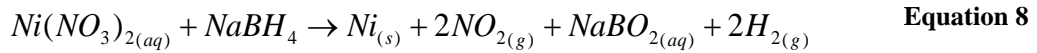


Figure 3: (A) A Cu-ammonia complex, capped with a surfactant, is formed at the start of the synthesis. (B) The complex is oxidized, forming Cu₂O nanoparticles. Ni²⁺ ions are added and adsorb on the surface of the Cu₂O. (C) Further addition of the reducing agent results in the formation of a NiO layer on the nanoparticles. (D-E) The inks are then ultrasonically sprayed on the substrate. (F) An IPL process reduces and sinters the film.



B. Synthesis of Copper Nitrate Hydroxide $\text{Cu}_2\text{NO}_3(\text{OH})_3$

Copper nitrate hydroxide was synthesized by the reaction of copper nitrate and potassium hydroxide. Copper nitrate hydrate $\text{Cu}(\text{NO}_3)_2 \cdot 2.5\text{H}_2\text{O}$, Alfa Aesar, 99.99%) was purchased from Alfa Aesar. Potassium hydroxide pellets (KOH, 98%) was purchased from Sigma Aldrich. 24 g (0.103 mols) $\text{Cu}(\text{NO}_3)_2 \cdot 2.5\text{H}_2\text{O}$ was dissolved in 200 ml of deionized water. In a separate beaker 11.64 g (0.207 mols, 4.16 M) KOH was dissolved in 100 ml of deionized water. The $\text{Cu}(\text{NO}_3)_2$ solution was stirred using a magnetic stirrer and the KOH solution was added to the solution at a rate of $1.67 \text{ ml} \cdot \text{min}^{-1}$ using a syringe pump. After the all of the KOH was added to the solution, the mixture was then placed in an ultrasonic bath for 30 minutes. The pale light blue precipitate was isolated by centrifuging the mixture at 7000 rpm for 3 minutes. The precipitate was washed once with deionized water.

C. Synthesis of Graphene Oxide via a Modified Hummer's Method

Graphite flakes (99.8%, metals basis) were purchased from Alfa Aesar. Potassium permanganate (99.0%), sulfuric acid (98%), hydrogen peroxide (35%) and hydrochloric acid (37%) were purchased from Sigma-Aldrich. All chemicals were used without additional purification. Graphene oxide (GO) was synthesized through use of a modified Hummer's Method.⁴³ The produced GO exhibited a yellowish-brown color. A typical procedure went as follows:

1. 3g of graphite and 63 mL of H_2SO_4 were carefully placed in a 1,000 mL three necked flask and placed into a refrigerator overnight.
2. The next day, the three necked flask was placed in an ice bath and under a water-cooled condenser operating under full reflux.

3. 9g KMnO_4 were slowly (approximately 15 minutes) added to the cooled flask – to prevent explosive by-product formation and facilitate the oxidative exfoliation.
4. The ice bath is removed and replaced with a water bath (to help equalize the distribution of heat) with a thermometer to observe the temperature, still under full reflux conditions, put over a hot plate, and heated to 40°C .
5. 138 mL of DI water were added, extremely slowly at first to prevent quenching the reaction, and then at a gradually increasing rate (~30 minutes)
6. Temperature was increased to 90°C for 15 minutes
7. A mixture of 420 mL of DI water and 30 mL H_2O_2 (refrigerated 30% solution) was added slowly (~45 minutes)
8. Centrifugation for 5 minutes at 7,500 rpm to separate out the GO
9. Washed with 3wt% HCl – remove unreacted graphite and metal contaminants (Na, Mn, etc.)
10. Washed with DI water until pH was neutralized (7^+ times) – checked with pH test strips

D. Synthesis of Copper Hydroxide Nanowires (NWs)

The $\text{Cu}(\text{OH})_2$ NWs were synthesized through a synthesis found in the literature for making $\text{Cu}(\text{OH})_2/\text{CuO}$ NW bundles.¹¹¹ PEG400 was utilized as the shaping agent due to its larger aspect ratio than the PEG200. The synthesis materials are depicted as a cartoon in Figure 17.

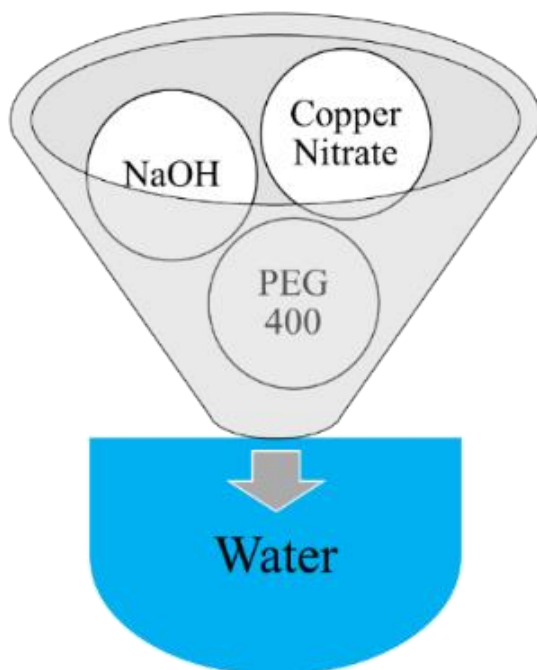


Figure 17: Schematic of $\text{Cu}(\text{OH})_2$ NW Synthesis involving copper nitrate (copper precursor), NaOH (reactant), and PEG400 (as a shaping agent)

A typical procedure goes for the synthesis of $\text{Cu}(\text{OH})_2$ NWs go as follows:

1. 600 mL of DI water was added to a three necked flask
2. 30 mL of PEG was added and magnetically stirred with patience as the polymer became part of the solution (instead of part of the problem)
3. 3.6 g $\text{Cu}(\text{NO}_3)_2 \cdot 2.5\text{H}_2\text{O}$ was added
4. 6.0 g of NaOH was slowly added over 10 minutes
5. Solution was stirred for four (4) hours
6. The product was isolated via centrifugation at 6,500 rpm for 3 minutes (Figure 18)
7. Washed with DI water until pH was neutralized - checked with pH test strips

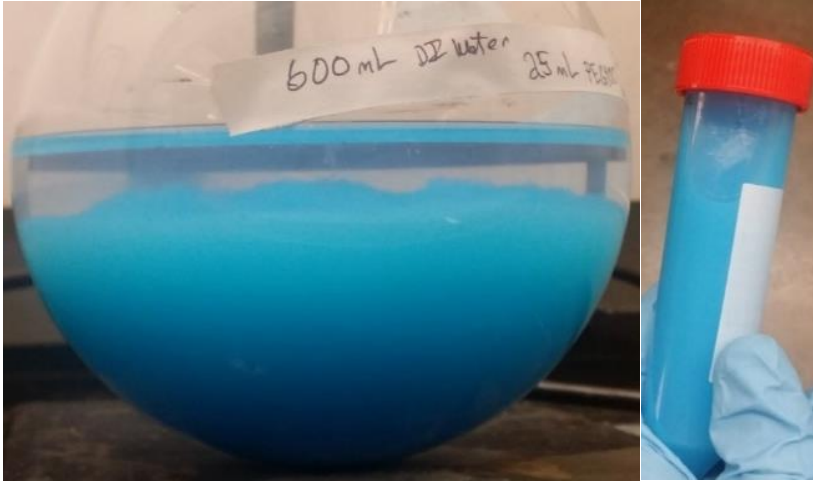


Figure 18: Image of reaction vessel after $\text{Cu}(\text{OH})_2$ synthesis vessel (left) and in a centrifuge tube prior to centrifugation process (right)

E. Procedures for Cleaning Substrates

Glass substrates were approximately 1" by 1" – cut with diamond scribe alignment system from VistaVision (soda-lime) microscopic glass slides purchased from VWR. The substrates were then cleaned by sonication for 10 minutes in three different solutions 1) alkaline detergent 2) DI water 3) ethanol or isopropyl alcohol and subsequently air dried. The samples were then treated with an oxygen plasma treatment for 10 minutes to remove any residual organics.

Silicon substrates were cut with the same system as the glass substrates (except for the Si used for thermoelectric measurements). The Si wafers were delicately moved with plastic tweezers, with the polished side being carefully placed on a ChemWipe, to prevent scratching. They were cleaned with sonication in three different solutions 1) alkaline detergent, 2) deionized water, and 3) ethanol then subsequently air dried.

PET substrates were cut with scissors and approx. 1" by 1" in size. They were cleaned with the same procedure as the glass substrates with the exception of the oxygen plasma treatment being reduced to 2 minutes (from 10 minutes), to prevent warping.

Cellulostic plastic (TOPAS 6015) substrates that were utilized were cut as 1" circles cleaned with sonication for 10 minutes in three different solutions 1) alkaline detergent 2) DI water 3) ethanol. This type of plastic was used as it was more brittle than PET and could be cut with the circular cutter procured for the lab.

F. Ink Formulation & Deposition

1) Ultrasonic Spray Deposition of Cu_2O -NiO core-layer

Nanostructures

The ink dispersions were sonicated using a Virsonic 100 Ultrasonic Cell Disrupter for at least 30 minutes prior to film deposition. Films were fabricated from the different inks using a 48 kHz ultrasonic spray mounted on to a WideTrack Coating System (Sono Tek). The inks were sprayed onto glass substrates placed on a hotplate at 120°C. The films were labelled according to the concentration of nickel nitrate used to fabricate the Ni layer. The films had a thickness of approximately 1.5 – 3.0 μm as measured using a Tencor AlphaStep 500 contact profilometer.

2) Screen Printing $Cu_2NO_3(OH)_3$

For deposition, 10 wt% monosaccharide was chosen to control the reducing atmosphere during the IPL process from decomposition and to increase the viscosity of the inks for screen printing. Inks were prepared by fructose or glucose with copper nitrate hydroxide through mixing 10 g (90 wt%) $Cu_2(OH)_3NO_3$ with 1.01 g (10 wt%)

monosaccharide (fructose or glucose) with a mortar and pestle prior to printing for 15 min. The inks were then allowed to air dry to remove residual water after the centrifugation process prior to screen printing. Inks were printed manually with a rubber squeegee onto a Ryonet 200 mesh grid. Square films printed for investigation.

3) Spin-coating GO

Two highly concentrated solutions were prepared with 8.095 g GO in 50 mL of ethanol. It should be noted that the GO was still considerably enraptured with water and moist during the weighing process. Of the 8.095 g in each solution, this would correspond to an estimated 2.835 g GO weight and an ink concentration of ~60 mg/mL. The solutions were thick due to the relatively high concentration. Prior to deposition they were sonicated for 10 minutes with bath sonication followed by 30 seconds with a more powerful probe sonicator (Hiescher UP200S, 200 W, 24 kHz) at 40% power. The spin-coating deposition occurred at six different speeds (5,000; 4,000; 3,000; 2,000; 1,000; and 500 rpm), with matching accelerations, for 30 seconds. Additional samples were produced at the 1,000 rpm spin speed, specifically with the fructose-containing solution.

4) Ultrasonic Spray Deposition & Rod-coating of GO

Ultrasonic Spray deposited GO films were fabricated with a 20 mg/mL GO ink (1.0 g GO in 40 mL H₂O and 10 mL ethanol, with .200 g of added fructose) using a 48 kHz ultrasonic spray mounted on to a WideTrack Coating System (Sono Tek). Specific variables used for this deposition are displayed in Table 4. A higher concentration of fructose was used compared to the screen printed Cu₂NO₃(OH)₃ to account for the GO source material having a large moisture content. The ultrasonic spray unit was operated

with glass and silicon substrates placed on a hotplate, set at 80°C. Prior to deposition, the inks were placed into a bath sonicator for 10 min and then subsequently placed into a powerful probe sonicator (Hiescher UP200S, 200 W, 24 kHz at 20% power for 90 seconds). The resultant ink exhibited high stability for months and has an observed black color. (Figure 19) It is noted that the color appeared as a yellow-ish light brown at lower concentrations.

Table 4: Ultrasonic Spray Deposition Variables

Variable	Setting
Nozzle Power	5-8 W
Air jet force	60 Lpm
Distance to stage from spray nozzle	5"
Stage travel distance	180 mm
Stage speed	25 mm/s
Pause between passes	5 s
Spray width	4.5"
Flow rate	1.0 mL/min
Number of passes	1,2,3,5,7,10
Hot plate temperature	80°C



Figure 19: Photograph of 20 mg/mL GO solution displaying great ink stability nearly five months after it was formulated

Rod-coating, or ‘Meyer rod’, deposition can help to facilitate the deposition of nanoscale-thin graphene oxide films, which also have a horizontal sheet orientation. This is an advantageous method over spin-coating deposition as it practical for scaling up and reduces wasted ink during deposition. The setup utilized the Meyer rod and an automated film applicator was operable over an area that is 8” wide and 12” long. Thin film deposition is done in a quick and repeatable fashion as the spiraled rods (around the main cylinder) confine the volume of ink over an area. The evaporative forces and surface interactions would then help to control the sheet orientation. The diameter of the rod was chosen as to be consistent with studies in the literature.⁶⁰ The solution concentration, choice of substrate, substrate surface modification treatments, doping of the pre-deposited graphene oxide material, and choice of solvent are examples of how the Meyer rod’s deposition process could be further optimized without the need of another diameter (as there are upwards of 90 to choose from).

5) Spin-coated and drop-casted GO & Cu(OH)₂ NW Mixtures

The mixtures of GO and NWs at a concentration of 15-20 mg/mL were analyzed at 68.35%, 91.53%, 98.18% and 100% GO, where the wt% GO of solutions was modified by adding .2 mL, 1.0 mL, and 5.0 mL from a 10 mg/mL solution of Cu(OH)₂ NWs. Fructose was added (.10g) for use in facilitate reduction via organic decomposition during IPL Processing. Samples were spun at 500 rpm, 1000 rpm, and 5000 rpm with matching accelerations for 30 s. Even thicker deposits were created via hot-casting, where the glass substrates were pre-heated on an 80°C hotplate directly before spin-coating the samples at 500rpm to further aid solvent evaporation. Drop-casted samples were prepared by dropping 6-8 drops of the ink onto substrates heated by an 80°C hotplate.

G. IPL Processing Parameters and Techniques

IPL Processing was performed with a Sinteron 2000 (Xenon Corporation), which emits incoherent white light ranging from 240 nm – 1000 nm. (Figure 20) Pulses were delivered at a pulse rate of 1.8 pulses per second, which is the factory setting for the equipment and used for all the materials studied in this dissertation. IPL Processing utilized 2044 μs pulses ranging from 589 J - 2070 J over an area of 1.9 cm x 30.5 cm, with energy densities of 10.1, 12.8, 15.8, 19.2, 22.9, 26.8, 31.1 and 35.7 Jcm^{-2} . The processing stage was placed at the focal point distance of 1" from bottom of the xenon lamp's window. Glass substrates were processed with maximum of 10 pulses in a row followed by a ten (10) second rest period to prevent the glass substrates from cracking, due to transient thermal conditions. Incremental IPL Processing was also performed to gradually increase the energy density of the process, where at 10 pulses at each energy density were applied giving a total 80 pulses with a cumulative energy density of 1744 Jcm^{-2} . (Figure 21)

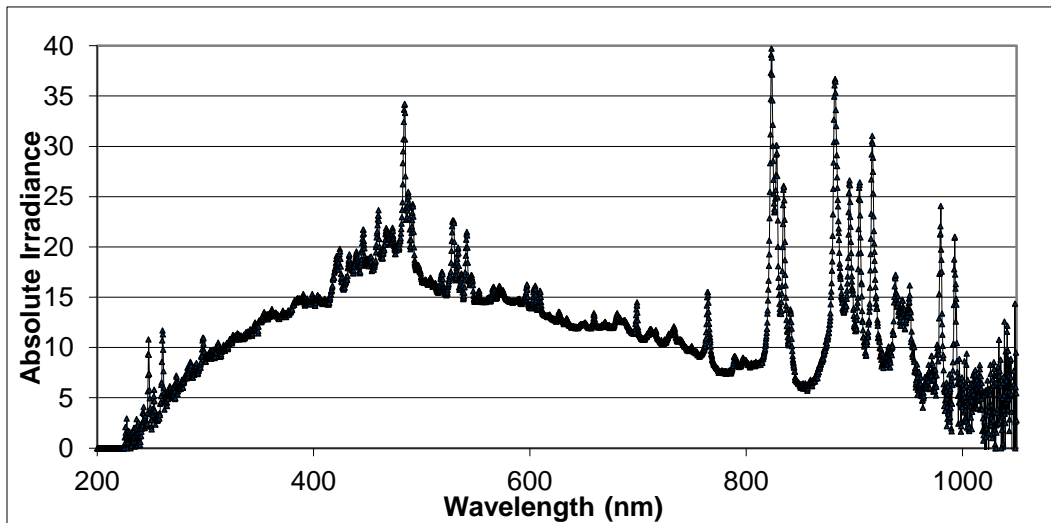


Figure 20: Emitted light Spectrum for Xenon 4.2'' lamp utilized for IPL Processing

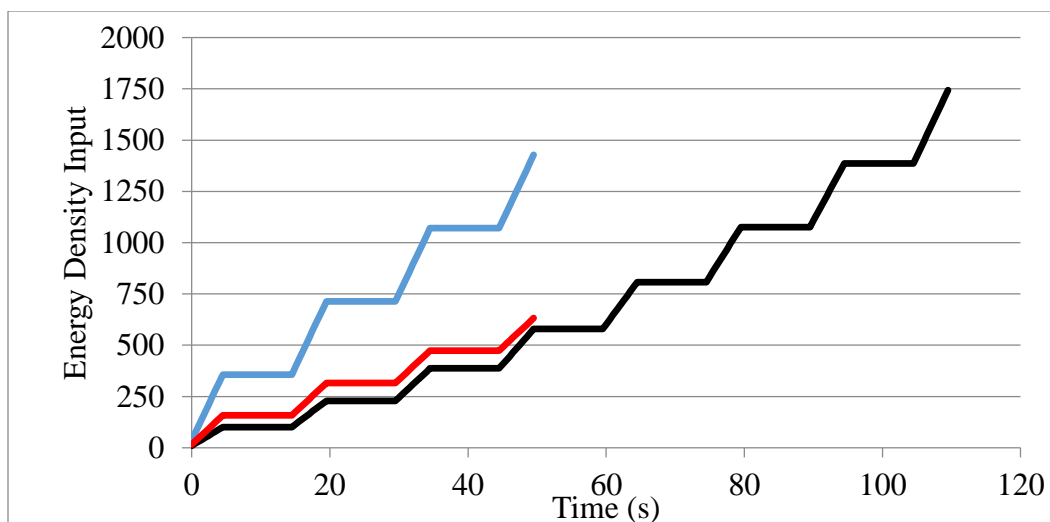


Figure 21: Comparison of IPL Processing Energy Density Input versus time shown for forty 15.8 Jcm⁻² pulses (red), forty 35.7Jcm⁻² pulses (blue), and Incremental (black). Ther

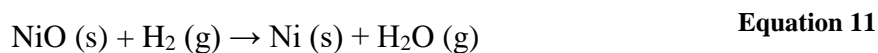
1) IPL Processing of Deposited Cu₂O-NiO core-layer Films

The Cu₂O-NiO core-layer films were subjected into IPL Processing under a nitrogen atmosphere using an incremental procedure described previously.¹⁰⁶ At each setting 10 pulses of light were applied. In total 80 pulses of light with a total energy density of 1744 Jcm⁻² was applied to each film. The transformation of the oxidized core-layer nanoparticles into a bulk metallic film proceeds via two steps. The first is the reduction of the Cu₂O@NiO precursor to their metallic forms, followed by the sintering and coalescence of these particles to form electrical pathways. Both stages capitalize on the high surface area to volume ratio associated with nano-sized particles. The high surface area provides a larger interface for the adsorption of reducing gases, thereby increasing the rate of reduction. In addition, the high surface to volume ratios can create a significant depression in the melting point temperatures of the metals, with the melting point of Cu (T_{Mpt.} bulk ~ 1080°C) and Ni (T_{Mpt.} bulk ~ 1455°C) being reduced to approximately 800

and 1270°C for particles with a 4 nm radius.^{10, 140} When considering only the Cu₂O system, both elevated temperatures and a reducing environment/atmosphere are needed for the reduction process to proceed.¹⁹⁴⁻¹⁹⁵ Finite element modelling has been used to predict the temperature rise induced by the IPL system in thin films deposited on glass substrates. This rise in temperature at the surface of the films was calculated to be higher than 800°C when multiple pulses of light with very short pulse durations were applied to the films.¹⁴⁸ Kim et al's study on the reduction of Cu₂O to Cu under a flow of 5% hydrogen (H₂ in helium), has shown that the reaction (Equation 10) proceeds without any intermediate phases being formed.



Under these conditions the temperature for the onset of Cu₂O reduction occurred at approximately 300°C with an activation energy of 114.6 kJmol⁻¹. Reduction of Cu₂O has also been shown to occur at lower temperatures, however the induction period where H₂ adsorption and dissociation takes place increases and the rate of the reaction decreases; resulting in significantly longer processing times (tens of minutes vs. hours).¹⁹⁴ The reduction of NiO to Ni using H₂ proceeds via a similar route (Equation 11).¹⁹⁶



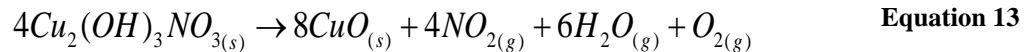
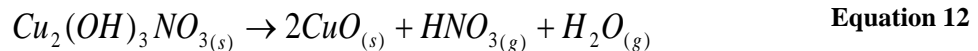
Similarly, to Cu₂O, the reduction of NiO begins with an induction period where H₂ is adsorbed and dissociated on the surface. This results in the “nucleation” of metallic Ni on the surface. Further reduction of the material occurs at the Ni/NiO interface and as the rate of reduction is proportional to interface area, an autocatalytic reaction occurs. Therefore, the reduction of the oxide proceeds inwards towards the core of the particles as the H⁺ diffuses in and H₂O diffuses out. The H₂O released in both the Cu₂O and NiO

reactions, results in a drop in the reduction rate in the closed systems as the H₂O molecules adsorbed on the surface hinder the adsorption of H₂. In the NiO system the activation energy for the reduction of the oxide to Ni is increased from approximately 85 kJmol⁻¹ to 127 kJmol⁻¹ when H₂O is added to the system. Furthermore, the formation of a continuous metallic film on the surface is believed to hinder the diffusion of H₂O out of the material.

194, 196

2) IPL Processing of Deposited Cu₂NO₃(OH)₃ Films

The thermal decomposition of Cu₂(OH)₃NO₃ to CuO was observed when IPL Processed without a generated reducing environment. IPL processed films have been shown to rise to high temperatures 300°C at an energy density of 8.3 Jcm⁻² and 500°C at an energy density of 17.6 Jcm⁻² for CdS.¹⁴⁸ Cu₂(OH)₃NO₃'s thermal decomposition values of 236-280°C¹¹⁶ were well within these temperature ranges and the thermal decomposition reaction of Cu₂(OH)₃NO₃ can be represented by Equation 12. At temperatures higher than 250°C however, HNO₃ converts to NO₂, H₂O and O₂.¹¹⁵ The formation reaction of cupric oxide would then be represented as Equation 13.¹¹⁴



The IPL Processing of Cu₂NO₃(OH)₃ films was carried out under ambient atmospheric conditions with forty pulses at energy densities of 10.1, 12.8, 15.8, 19.2, 22.9, 26.8, 31.1 and 35.7 Jcm⁻². A 15 s rest period, where no pulses were applied, was used between each set of 10 pulses to prevent cracking of the glass substrates. FTIR analysis was performed with samples processed at a constant energy density of 12.8 Jcm⁻². Figure 22 displays an example of how a sample can exhibit a clear change in color through IPL

Processing. The ultraviolet portion of spectrum is particularly essential to films that are optically transparent in the visible electromagnetic spectrum.



Figure 22: Example of visible change of a $\text{Cu}_2\text{NO}_3(\text{OH})_3$ sample before (left) and after (right) IPL

Processing

3) IPL Processing of Deposited GO and GO & $\text{Cu}(\text{OH})_2$ Films

The IPL Processing of GO films was conducted utilizing 2.044 ms pulses with energy densities of 10.1, 12.8, 15.8, 19.2, 22.9, 26.8, 31.1 and 35.7 Jcm^{-2} . They pulses were either applied with forty pulses of a specific energy density or in an incremental fashion, with ten pulses at each energy density. IPL processing reduces the films directly with UV light and by increasing the thermal energy, where H_2O and CO_2 formation is possible through the removal of the GO's oxygenated functional groups (i.e. alcohols, carboxylic acids, epoxides, and aldehydes). (Equation 14) To enhance the capacity of IPL processing to reduce GO, an organic molecule was introduced. Fructose was selected, as it was shown in previous work to be an advantageous additive since it has a relatively low thermal decomposition temperature and is readily available. Fructose was incorporated at 10 wt% of the GO present in the solutions prior to deposition, to be consistent with the wt% utilized in previous work.¹⁷⁰ With fructose being included, the proposed mechanism is shown below using one of its decomposition products, folic acid, to model the reaction. (Equation 15)



H. Characterization Instruments Utilized for Study

A FEI Nova NanoSEM 600 (Figure 23) or a Tescan SEM (Figure 24) with an accelerating voltage of 1- 15 kV and a working distance of 5 - 6 mm was used to study the morphology of the nanomaterials, film deposition uniformity, and the extent of sintering. Technai G220 transmission electron microscope operated at 200 kV. A drop of acetone with the dispersed powder was taken on a porous carbon film supported on a gold grid, and then dried in vacuum. A Bruker AXS D8 X-ray diffractometer using Ni- filtered Cu-K α radiation with a step size of 0.02° and a scan speed of .05 sec/step was utilized for x-ray diffraction characterization of the crystal lattices. (Figure 25) Transparency measurements were performed with a Lambda 950 UV–vis spectrophotometer. Sheet resistance measurements were carried out with a Four-point probe attached to a Keithley Model 2401 SourceMeter. An Alpha-Step 500 Surface Profiler was used to measure the thickness of films. Simultaneous Differential Scanning Calorimetry and Thermogravimetric Analysis (SDT) with a heating rate of 10°C per min up to 800°C under 100 ml/min N₂ flow. Raman Spectroscopy was performed with a Renishaw inVia Raman Spectrometer and excited by a red laser (632nm), calibrated with Si to 520-521 cm⁻¹, with 4 repetitions to increase signal-to-noise ratio. (Figure 26) Raman data was typically processed (smoothed, subtracted baseline, and normalized from 0 to 1). Presence of organic molecules were observed with a PerkinElmer Spectrum BX FT-IR spectrometer through use of KBr pellets. The potassium bromide (KBr, ≥99%, Sigma Aldrich) pellets were created by taking 15 mg

of KBr and adding 2% of a given sample, by physical removal from substrate, and then pressing at 5 tons for 10 minutes. All $\text{Cu}_2\text{NO}_3(\text{OH})_3$ FTIR samples were done with a varying amount of pulses at an energy density of 12.8 Jcm^{-2} and normalized to account for weight variations.

Thermoelectric measurements were performed as follows. $\langle 100 \rangle$ p-type silicon (Si) wafers (1-10 Ωcm , 500 μm thick, Silicon Prime Wafers) were cut into approximately $1.0 \times 0.7 \text{ cm}^2$ samples and were cleaned using the standard RCA cleaning method prior to measurement of the thermoelectric power.¹⁹⁷ A solution containing ammonium hydroxide (10 ml, 28% NH_3OH , Alfa Aesar), hydrogen peroxide (10 ml, 30% H_2O_2 , J.T. Baker) and deionized water (50 ml) was heated to 70°C . The wafers were placed in the solution for 10 minutes to remove organic contaminants from the surface. Following cleaning the rinsed wafers were etched in approximately 2.5 vol% Hydrofluoric acid (48% HF, Cole Parmer) solution for 10 minutes to remove native oxides from the surface. The wafers were then rinsed again with deionized water. A solution containing hydrochloric acid (10 ml, 37% HCl, Sigma Aldrich), H_2O_2 (10 ml) and deionized water (50 ml) was heated to 70°C . The wafers were placed in the cleaning solution for 10 minutes prior to deposition to remove ionic contaminants from the surface and create a thin passivation layer on the surface of the wafer. Following cleaning the cut wafers were left bare or coated with either the basic Cu_2O ink (i.e. no Ni layer) or $\text{Cu}_2\text{O}@ \text{NiO}$ ink synthesized using 1 mM of the Ni salt. The wafers coated with the ink were then IPL treated under the conditions described above. Each wafer was mounted on to the sample holder and two, K-type thermocouples were connected along the length of the wafer using a small amount of high purity conductive silver paint. A small heater was positioned in direct contact to the Si, closest to the first

thermocouple. The sample holder was then inserted into a glass chamber and pumped down to 10^{-5} Torr. A Barnstead Themolyne 2100 Tube Furnace was used to heat the wafer to 370°C (643 K) and cool it back to room temperature at a rate of $5^{\circ}\text{C}/\text{min}$. The small heater creates a localized temperature gradient along the length of the wafer. Subsequently majority charge carriers (holes) diffuse from the hot to the cold area, resulting in a potential difference. Both the temperature difference (ΔT) and open circuit potential difference (ΔV) along the length of the sample were measured simultaneously using Keithley source-meters (2400, 2410), nanovoltmeters (2182A) and picoameters (6487), as well as a Fluke 8842A multimeter. The thermoelectric power of the sample at a given temperature was calculated; $S = \Delta V/\Delta T$.



Figure 23: Photo of FEI SEM



Figure 24: Photo of Tescan SEM

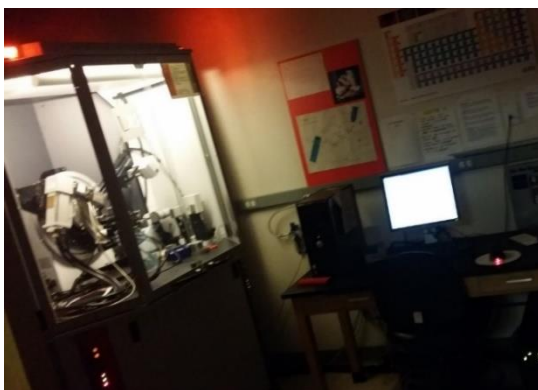


Figure 25: Photo of X-ray Diffraction Instrument

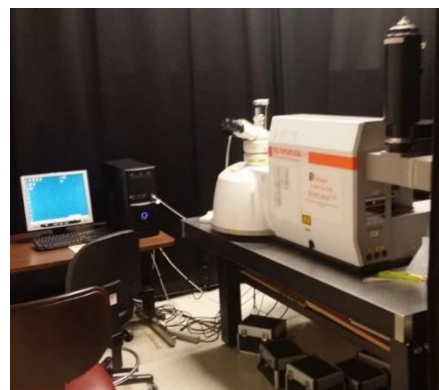


Figure 26: Photo of Raman Spectrometer

CHAPTER 4: IPL PROCESSING $\text{Cu}_2\text{O}@$ NiO ENCAPSULATED NANOPARTICLES

A. Introduction

This chapter focuses on the prevention of Cu diffusion into Si by incorporating a thin Ni barrier layer around Cu nanoparticles, which was accomplished through solution phase process that synthesized copper oxide nanoparticles and then encapsulated them with a nickel oxide layer to form (Cu_2O -NiO) core-layer nanostructure. Synthesis was performed in the presence of a surfactant to control particle diameters and layer thicknesses. The process described here does not rely on the co-precipitation of metals in a single bath, has been carried out at room temperature, and do not require further processing prior to deposition. The room temperature process enables us to easily prevent the formation of alloys at the copper-nickel interface. The synthesis results in a simple technique (easily commercializable;) with highly controllable layer thicknesses on a 20 nm copper oxide nanoparticle. The deposited films are then subjected to IPL processing to reduce the oxides to their metallic form and sinter the films to yield highly conductive films in very short process times. Films have been deposited onto silicon, and the copper-nickel structure reduced Cu diffusion into Si. The films are analyzed using transmission electron microscopy (TEM), X-ray diffraction (XRD), and Four Point Probe techniques.

B. Results and Discussion

1) *Synthesized of Cu₂O-NiO core-layer Nanostructures*

TEM micrographs of the Cu₂O@NiO nanostructures, synthesized using different concentrations of Ni(NO₃)₂; 1 mM, 5 mM and 20 mM are shown in Figure 27. Figure 27a-c shows that the size of Cu₂O core nanoparticles were approximately 10-20 nm in size. The TEM micrographs were used to approximate the thickness of the NiO coating. The thickness of the NiO layer was observed to grow almost linearly as the Ni²⁺ concentration used in the reaction was increased. Average thicknesses of 5, 9, 15 and 20 nm were measured when Ni²⁺ concentrations of 1, 5, 10 and 20 mM were used. The corresponding high resolution images are also shown in the insets. From the images it is clear that the Cu₂O nanoparticles exist as an agglomeration, and the NiO layers are formed around these agglomerates.

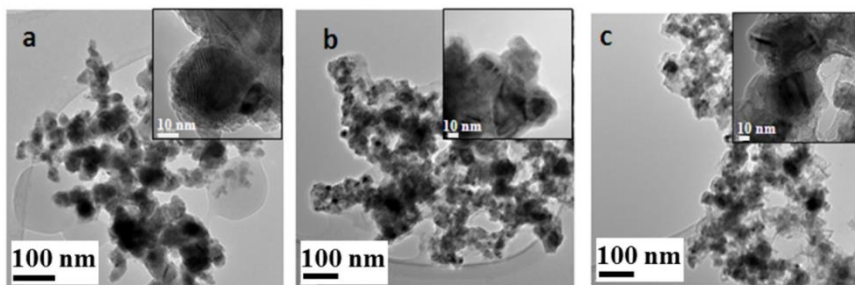


Figure 27: TEM micrographs of Cu₂O@NiO nanostructures obtained using Ni²⁺ concentration of (a) 1 mM, (b) 5 mM, and (c) 20 mM. The insets show high resolution TEM micrographs.

Furthermore, TEM EDX studies on the Cu₂O@NiO core-layer confirmed the presence of Cu and Ni (Figure 28). As expected the Cu₂O/NiO ratio increased linearly with the Ni²⁺ concentration (Figure 28 inset). The results suggest that as the concentration of Ni ions in the reaction was raised, the thickness of the NiO layer in the Cu₂O@NiO core-layer

nanoparticles increased. From these studies it appears that by tuning the initial concentration of Ni^{2+} ions, the thickness of the Ni layer can be controlled.

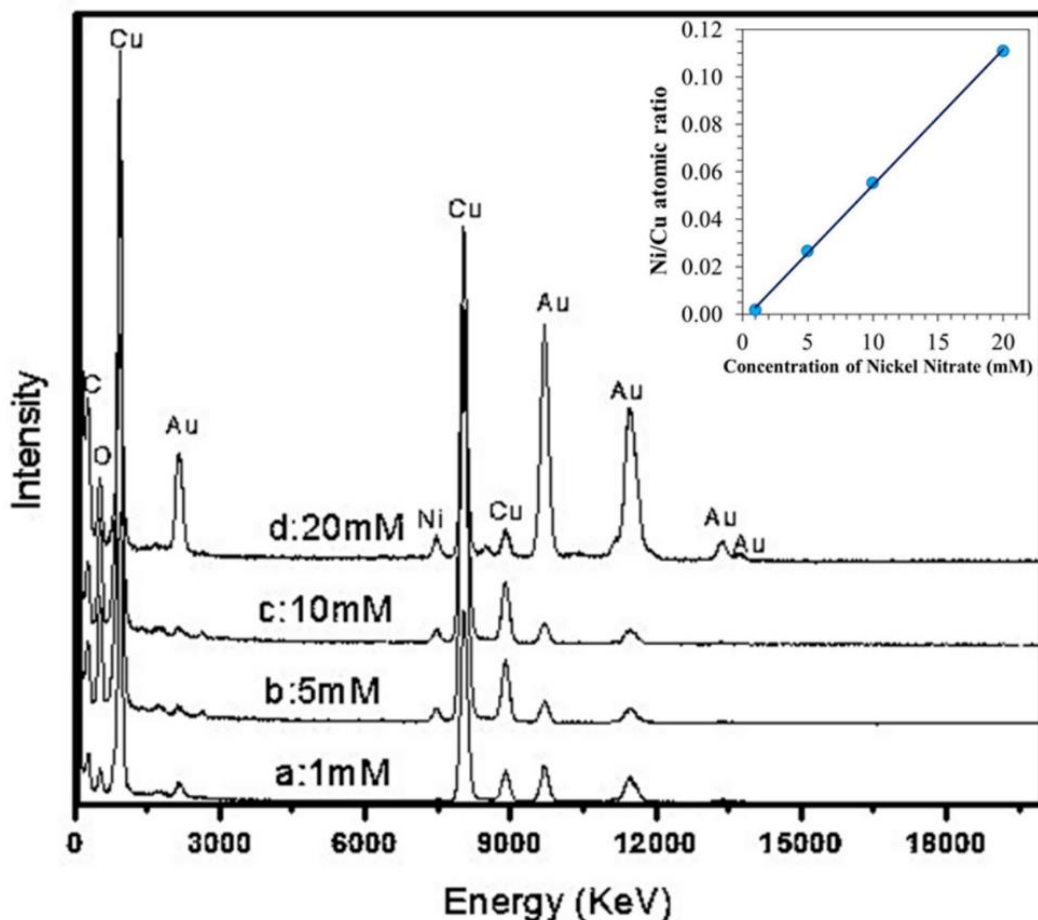


Figure 28: TEM-EDX pattern of samples (a) 1 mM, (b) 5 mM, (c) 10 mM and (d) 20 mM. The inset shows TEM-EDX quantification results: Ni/Cu atomic ratio

The primary Cu_2O nanoparticles were synthesized with Tergitol NP-9 and ethylene glycol, while the NiO coating was subsequently formed by transferring the Cu_2O nanoparticles into an acetone and water based solution containing Ni^{2+} ions. The films were deposited from this acetone based solution onto substrates heated to approximately 120°C ; driving off excess acetone and water. Consequently, this low temperature deposition results in residual chemicals of ethylene glycol and Tergitol surrounding the particles. Although

it is worth noting the adsorption of small amounts of acetone on the surface of the Cu₂O@NiO particles is also possible. However due to their low volatility both ethylene glycol and Tergitol will be the primary constituents. Upon IPL treatment these organic residues surrounding the system are decomposed in to reducing gases. The temperature increase in the films is caused by the adsorption of intense pulses of white light with wavelengths ranging from 240 nm – 1000 nm, by the Cu₂O@NiO particles. The pulses have a spectral distribution similar in shape to that of sunlight. However the Xenon spectrum contains a large amount of UV light with the irradiance peaking close to the visible region (~450 nm), before gradually tailing off into the IR region.¹⁹⁸ NiO and Cu₂O are known to have bulk bandgaps of 3.5 and 2.1 eV, respectively.¹⁹⁹ Hence, the as-deposited films are expected to adsorb a significant proportion of the energy supplied from the pulses.

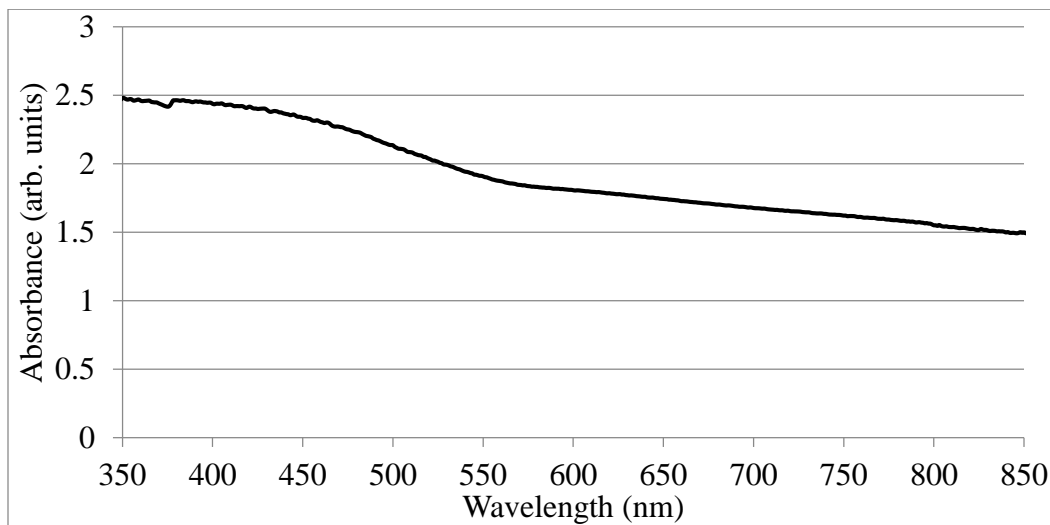


Figure 29: UV-Vis adsorption measurement of 1mM as deposited sample

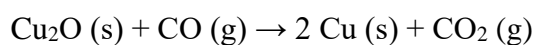
UV-Vis adsorption spectra of the 1 mM films showed good adsorption from the UV to IR region, with the films displaying highest absorption in the high energy (UV)

region. The gradual adsorption edge is a result of the light scattering by the nano-sized particles (Figure 29). Therefore, the nanoparticles absorb energies greater than or equal to their bandgap, promoting electrons across the bandgap. As the electrons relax to lower energy states, phonons are produced in the crystal lattice and cause a temperature rise in the material. The high intensity of the light pulses creates large number phonons which can elevate the temperature of the films from room temperature to several hundred degrees centigrade during the millisecond pulse.

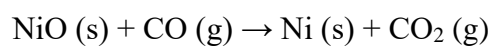
FTIR analysis of the as-deposited Cu₂O@NiO films was performed to understand the point at which the IPL treatment removed the organic residues from the films. The FTIR spectrum of the as-deposited films clearly showed the presence of organic residues; with peaks for the O-H, C-H, C=O, C-O and C-H bonds being observed (Figure 30). The films were subsequently treated with one pulse of light using an energy density of 10.2 Jcm⁻², resulting in a significant reduction in the peak intensity for all of the bonds. Thermal decomposition of ethylene glycol is reported to begin at temperatures greater than 240°C, primarily forming glycolic acid with small amounts of oxalic and formic acid.²⁰⁰ Therefore, one pulse of light at this intensity appears to be sufficient for the films temperature to reach the decomposition temperature of the organic components surrounding the nanoparticles. The IPL procedure used on these films, gradually ramps up the intensity of the light pulses.

Increasing the number of pulses applied to the films to 5 pulses with an energy density of 10.2 Jcm⁻², led to a further reduction in the FTIR peak intensity (Figure 30). Therefore, after initially decomposing the ethylene glycol, the glycolic acid can be further decomposed to CO, CO₂, H₂, CH₄, CH₃OH and CH₂O. Tergitol NP-9's largest component is nonylphenyl polyethylene glycol ether. This ether begins to decompose at approximately

250°C, forming CO, CO_x, NO_x and hydrocarbons as its decomposition products. After a total energy input of 231 Jcm⁻² (10 pulses × 10.2 Jcm⁻² + 10 pulses × 12.9 Jcm⁻²) was applied to the films, the absence of peaks in the corresponding FTIR spectrum indicated that all of the organic residue had been removed and thermally decomposed to form the reducing atmosphere. The decomposition products for acetone also include CO, CH₄, H₂ and C₂H₄.²⁰¹ Therefore it is clear that CO is a key component of the reducing gases. Both Cu₂O and NiO will be reduced; with CO reacting with oxygen on the surface of the lattice (Equation 16 and Equation 17).



Equation 16



Equation 17

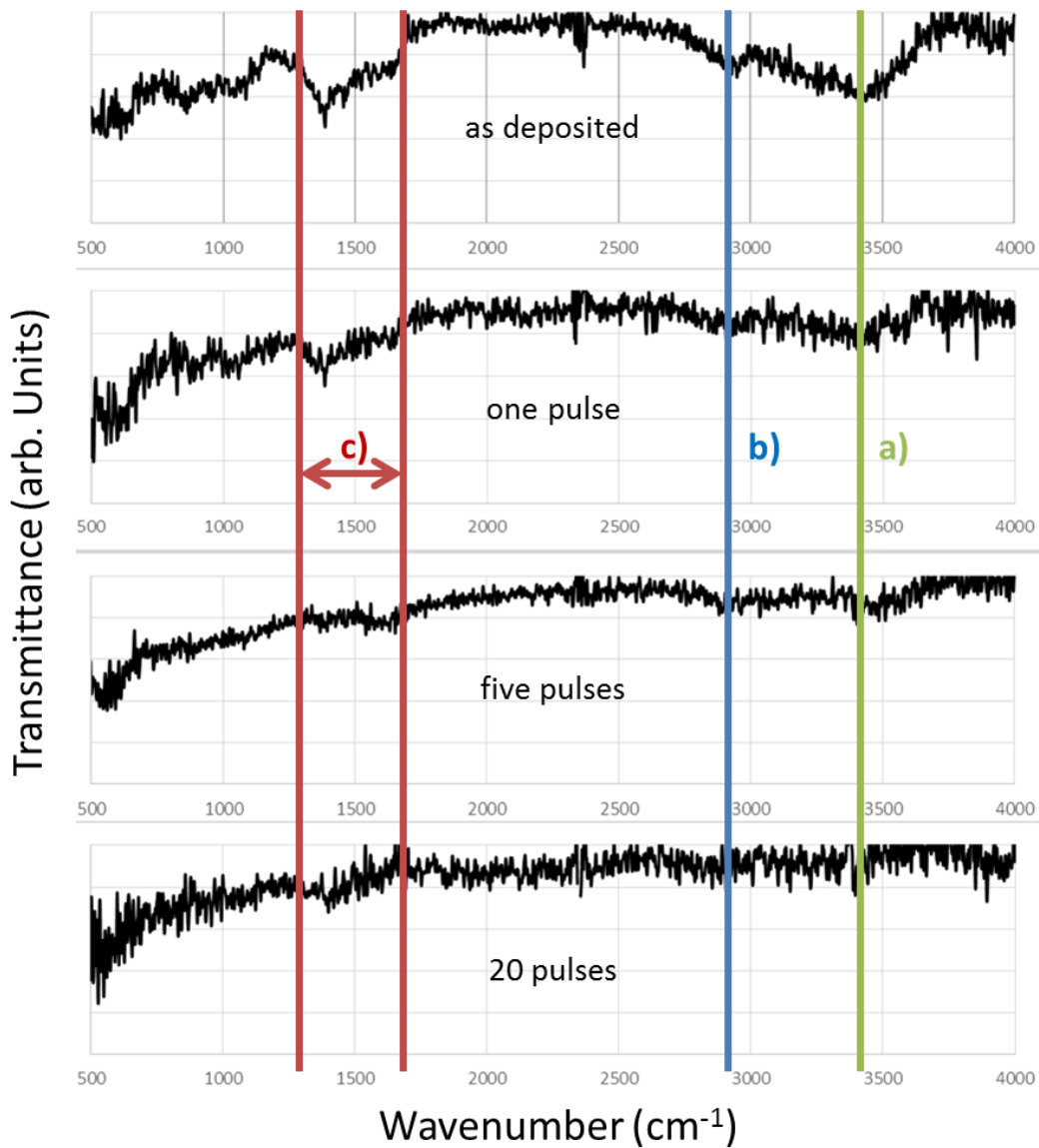


Figure 30: FTIR spectrum (from top to bottom) of the as deposited, one IPL Pulse (energy density of 10.2 Jcm⁻²), five IPL pulses (energy density of 10.2 Jcm⁻²), and twenty IPL pulses 1mM samples (ten pulses at an energy density of 10.2 Jcm⁻² and ten pulses at an energy density of 12.9 Jcm⁻²). a) O-H bonds b) C-H alkane bonds c) C=O, C-O, and C-H bonds

The reducing gases formed during the IPL are adsorbed onto the surface of the particles, reducing the NiO to Ni. As the reaction progresses, gases diffuse into the core of the particles reducing both the NiO shell and the bulk of the particles (Cu_2O). Increasing the thickness of the NiO oxide shell causes a number of effects on the system. (1) The overall particle size is increased; reducing the relative surface area available for the adsorption of gases, and (2) the reducing gases must diffuse and react with a relatively larger volume of material. Subsequently the increase in the thickness of the Ni shell results in the incomplete reduction of the Cu_2O core.

Investigations into the composition of the primary Cu based nanoparticles was previously reported.¹⁰⁶ XRD investigations of the deposited films showed that the inks were composed of Cu_2O and Cu in approximately a 2:1 ratio. The crystallites were orientated towards the (111) reflections for both cubic Cu_2O ICDD (00-001-1142) and cubic Cu ICDD (00-001-1241). The application of the NiO coating shows no additional reflections corresponding to nickel compounds and no shifts in the positions of the Cu_2O and Cu reflections in the XRD patterns of the as-deposited films (not shown). Figure 31a shows the XRD diffraction patterns of the IPL treated films fabricated from 1 mM and 10 mM $\text{Ni}(\text{NO}_3)_2$. All the IPL treated films displayed (111), (200), (220) and (311) reflections corresponding to cubic Cu_2O (ICDD 00-001-1142) and Cu (ICDD 00-001-1241). Due to the relatively small quantities of $\text{Ni}(\text{NO}_3)_2$ used to synthesize the dispersions, no reflections for either NiO or Ni were observed.

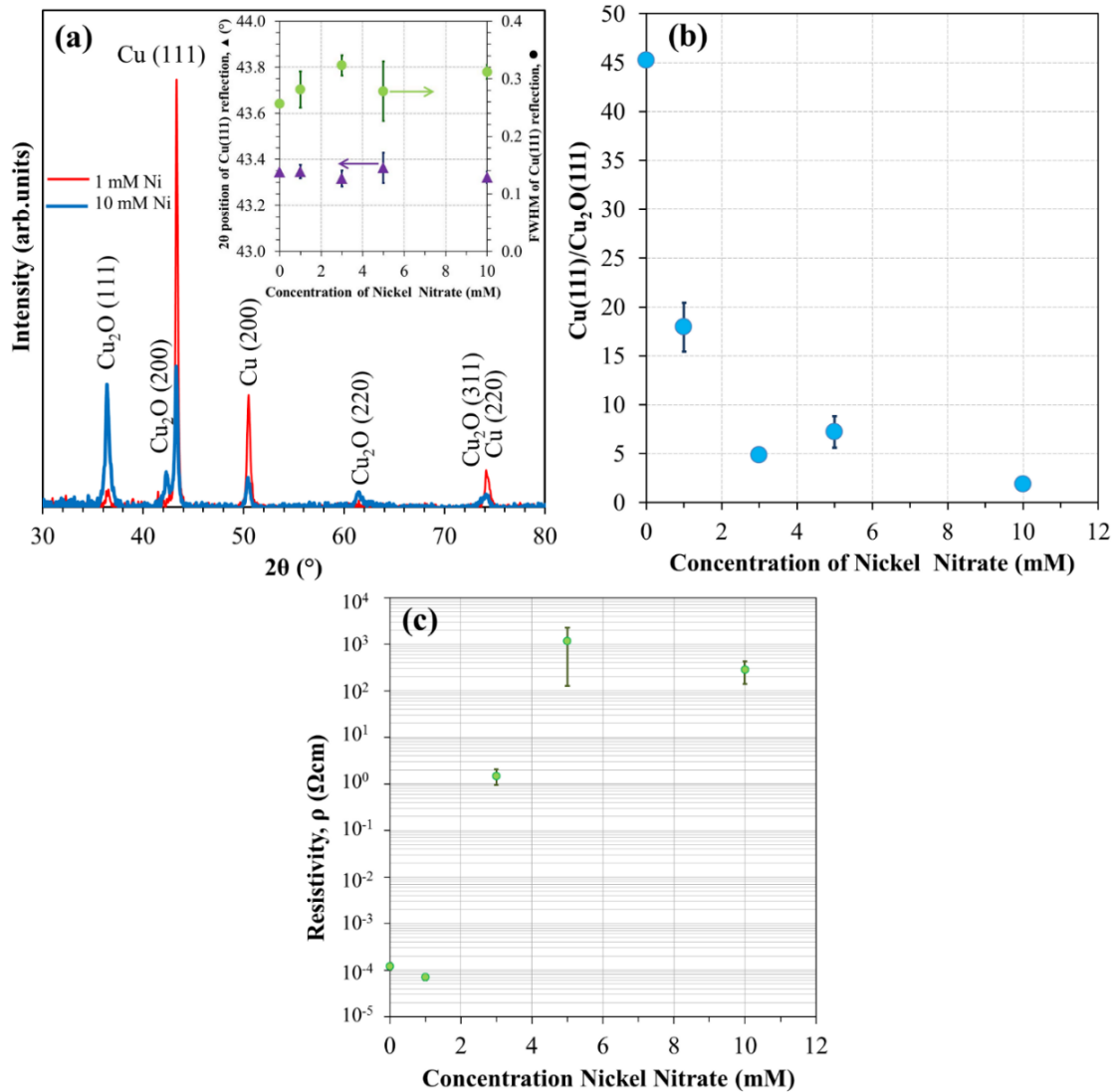


Figure 31: (a) X-ray diffraction patterns of the films after IPL treatment formed using the 1 mM and 10 mM inks. The inset shows the effect of the concentration of Ni nitrate solution on the 2θ position and FWHM of the $\text{Cu}(111)$ reflection. The error bars were calculated from the standard deviation. (b) Ratio of the intensity of the $\text{Cu}(111)/\text{Cu}_2\text{O}(111)$ reflections after IPL treatment vs. the concentration of nickel nitrate used to fabricate the nickel shell. The error bars were calculated using the standard error. (c) Resistivity of the IPL treated films vs. concentration of nickel nitrate used to fabricate the nickel shell. (The results at 0 mM Nickel nitrate were taken from a previous study).¹⁹³ The error bars were calculated using the standard error.

Figure 31b also shows the effect of increasing the concentration of Ni salt on the ratio of the Cu(111)/Cu₂O(111) reflections. The results demonstrate a significant decrease in this ratio as the thickness of the Ni layer was increased. Indicating the increasing thickness of the Ni layer is hindering the reduction of the Cu₂O.

Figure 31c shows the effect of the concentration of the Ni salt used to synthesize the layer on the resistivity, ρ of the films after IPL treatment. Using Ni salt concentrations of 5 and 10 mM, the ρ of the films remained above 102 Ωcm . By decreasing the concentration of Ni salt in the synthesis stage to 3 mM, the reduction in the thickness of the layer yielded a two orders of magnitude drop in ρ . Further reductions in the Ni²⁺ concentrations to 1 mM, produced a ρ similar in magnitude to the films produced without the Ni layer. Resistivity values for bulk Cu and Ni have been reported as 1.67×10^{-6} and 6.8×10^{-6} Ωcm at 25°C.²⁰² The films fabricated from the 1 mM Ni salt solutions are only one order of magnitude away from the bulk ρ of Ni due to the high porosity of these films. The films produced with thicker Ni layers demonstrate a significantly higher ρ due to the incomplete reduction of Cu₂O.

2) XRD Regression Analysis to determine if Cu-Ni alloy is formed

The low temperature synthesis method described above produces a Cu₂O core and a discrete NiO layer that does not appear to form an alloy, although literature reports on the synthesis of Cu@Ni core@shell nanoparticles have found an alloy at this interface.^{101,}
¹⁴⁰ Although the relatively small difference in the atomic radii of Cu and Ni is known to result in the easy formation of solid solutions, it would appear as though the IPL Processing is preserving the distinct boundary between the metals at the interface. Therefore, to investigate if Cu and Ni are alloying during the synthesis and subsequent IPL treatment,

the positions of the XRD reflections were analyzed further. If alloying is present in the system, the reflections will broaden and shift between the corresponding positions for Cu and Ni. It was found, as detailed below, that both the position of the Cu (111) and the full width half maximums (FWHM) did not vary significantly with an increasing Ni salt concentration

Integral Regression Analysis for the position of the Cu(111) reflection using a 95% confidence interval linear regression. Analysis of the data found the coefficients to be 43.35° (intercept) and $-0.0017^\circ\text{mM}^{-1}$ (slope). The position of the maximum peak for the pure copper at $2\theta=43.3459^\circ$ fell within the lower (43.305°) and upper (43.385°) bounds. The slope of zero fell within the lower ($-0.009^\circ\text{mM}^{-1}$) and upper ($0.005^\circ\text{mM}^{-1}$) bounds. The (111) reflection is expected to shift from a 2θ position of 43.19° for a 100% Cu system towards 44.60° for 100% Ni system, as Cu and Ni alloy.¹⁰¹ The position of the XRD reflections does not show an indication of Cu alloying with the Ni after IPL treatment (Figure 32 inset). The value of the Cu (111) reflection falls within the lower and upper bounds for the intercept (Figure 32). Additionally, the value of zero was also in between the lower and upper bounds for the slope. Therefore, we fail to reject the null hypothesis that the Cu (111) reflection positions for all patterns are the same.

A similar Integral Regression Analysis was performed for the full width half maximum (FWHM) of the Cu(111) reflection using a 95% confidence interval linear regression (Figure 33). Analysis of the data found the coefficients to be 0.289° (intercept) and $0.002^\circ\text{mM}^{-1}$ (slope). The position of the FWHM of pure copper at $2\theta = 0.257^\circ$ fell within the lower ($.256^\circ$) and upper ($.323^\circ$) bounds. The slope of zero fell within the lower ($-0.004^\circ\text{mM}^{-1}$) and upper ($0.008^\circ\text{mM}^{-1}$) bounds. The FWHM value observed in the Cu

films fell within the upper and lower bounds of the 95% confidence interval. Additionally, a slope of zero also fell within the lower and upper bounds for the slope. Therefore, the null hypothesis, that the broadness of the reflections is equal for all concentrations of the Ni salt, is failed to be rejected supporting the absence of a Cu-Ni alloy. Lastly, both data sets had residuals that did not show a recognizable pattern and were scattered randomly about the y-axis.

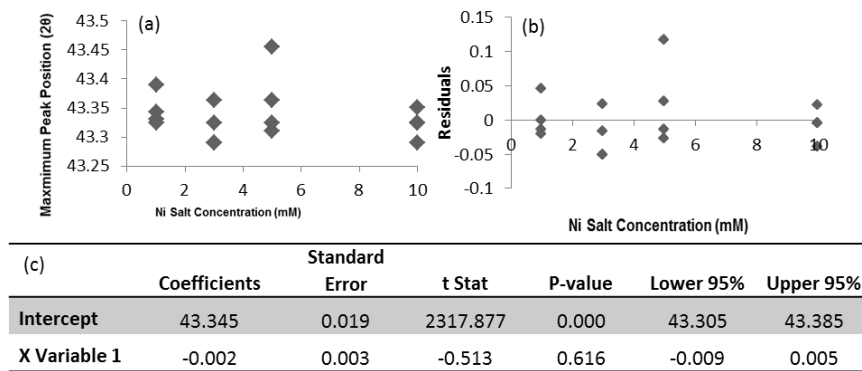


Figure 32: (a) Maximum Peak Position of the Cu(111) reflection versus the concentration of the nickel salt. (b) Residuals for the analysis of the Cu(111) reflection versus the concentration of the nickel salt.

(c) Tabulated linear regression results.

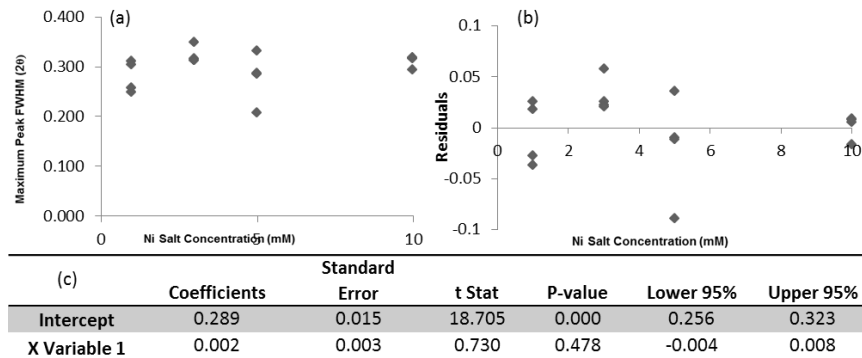


Figure 33: (a) FWHM of the Cu(111) reflection vs. the concentration of the Ni salt. (b) Residuals for the FWHM of the Cu(111) reflection vs. the concentration of the Ni salt. (c) Tabulated linear regression results.

The final aim of these inks is to replace the Ag pastes currently utilized in the PV industry to make the front metal contacts on silicon solar cells. The close to the bulk value of Ag with an average ρ of approximately $3.0 \times 10^{-6} \Omega\text{cm}$, meaning that the resistivity of our films are ~ 1.5 orders of magnitude higher. One reason for the higher electrical resistance of the films is porosity, as seen through SEM imaging of the as-deposited and IPL Processed films for the 1mM inks. (Figure 34). The as-deposited films display a degree of porosity, even before the films were IPL treated. After a total energy input of 231 Jcm^{-2} was applied to the films, particle coalescence and melting was observed (Figure 34b). FTIR investigations found that at this point in the IPL process, all the organic residual had been removed from the film. However, removal of the organic materials also resulted in the formation of significantly larger pores in the film. Increasing the energy density of the pulses even further resulted in further sintering and melting of the particles without significant changes to its porosity. We believe that optimizing the deposition and IPL conditions will result in lower porosity, resulting in a reduced ρ .

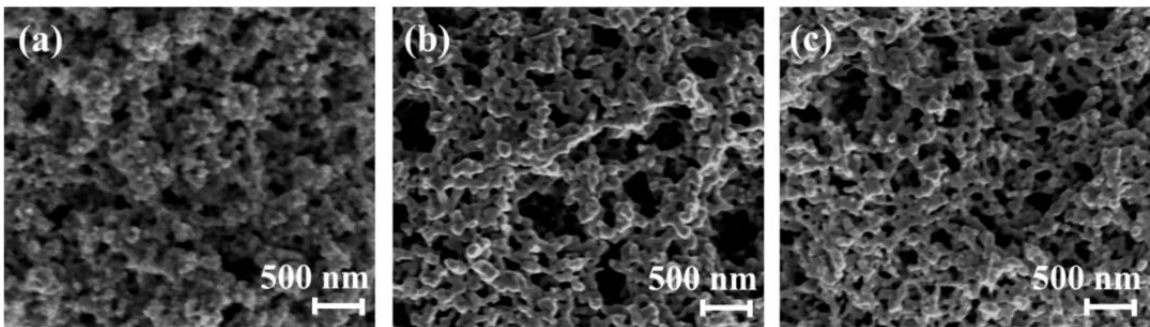


Figure 34: SEM images of the surface of the (a) as-deposited and (b & c) IPL treated films deposited using 1 mM inks. The films were treated using a total energy density input of (b) 231 Jcm^{-2} and (c) 826.7 Jcm^{-2}

3) Elemental Distributions throughout IPL Processing

A closer examination of the nanostructures was done using STEM-EDX to map the distributions of the Cu and Ni metals after the IPL process for the 1 mM (Figure 35), 5 mM (Figure 36), and 20 mM (Figure 37) Ni^{2+} ion concentrations. The distribution of the metals after the IPL process for the material made using shows that the Ni encompasses the entirety of the Cu (Figure 34 d and e). Additionally, the Ni has formed a measureable layer that increases in thickness as the concentration of Ni^{2+} progresses from 1 mM to 20 mM. The layer of the 1 mM sample is very thin, much thinner that reported earlier. This confirms the Cu-Ni core-layer nanostructure thin film using ambient temperature routes/processing.

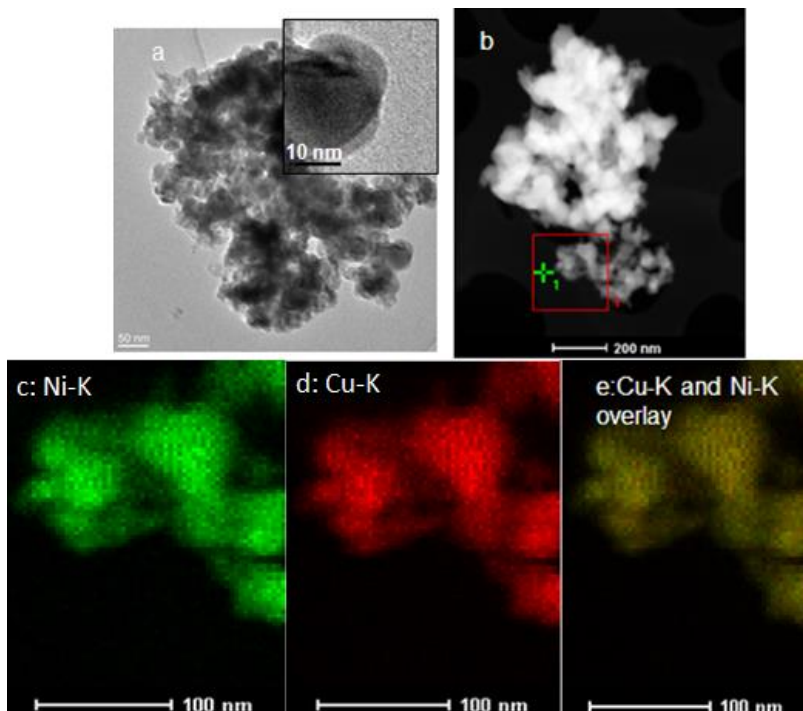


Figure 35: Nanostructures obtained after IPL Sintering using an initial Ni^{2+} concentration of 1 mM; (a) TEM micrograph (a-inset) HRTEM micrograph, (b) STEM, (c) Ni-K maps, (d) Cu-K maps and (e) Cu-K and Ni-K overlaid micrographs.

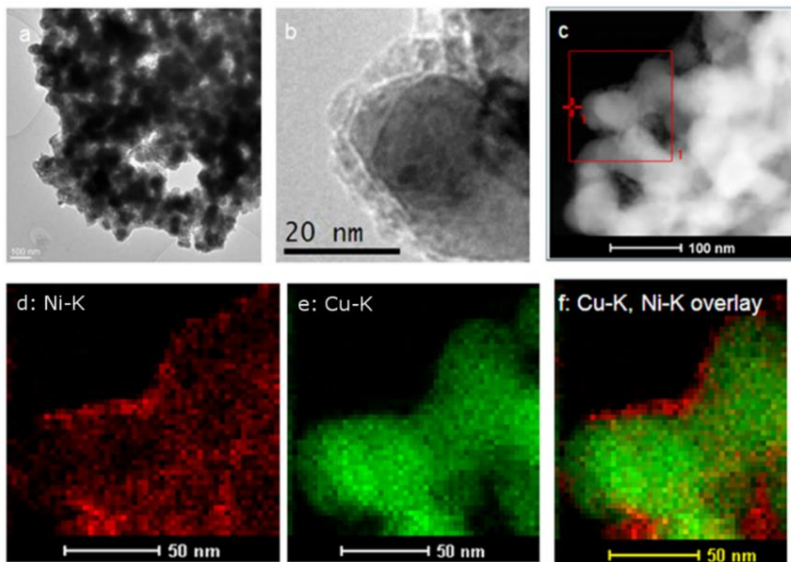


Figure 36: Nanostructures obtained after IPL Sintering using initial Ni^{2+} with concentration of 5 mM (a) TEM micrograph, b) HRTEM micrograph, c) STEM, d) Ni-K mapping, e) Cu-K mapping f) Cu-K and Ni-K overlay mapped micrograph.

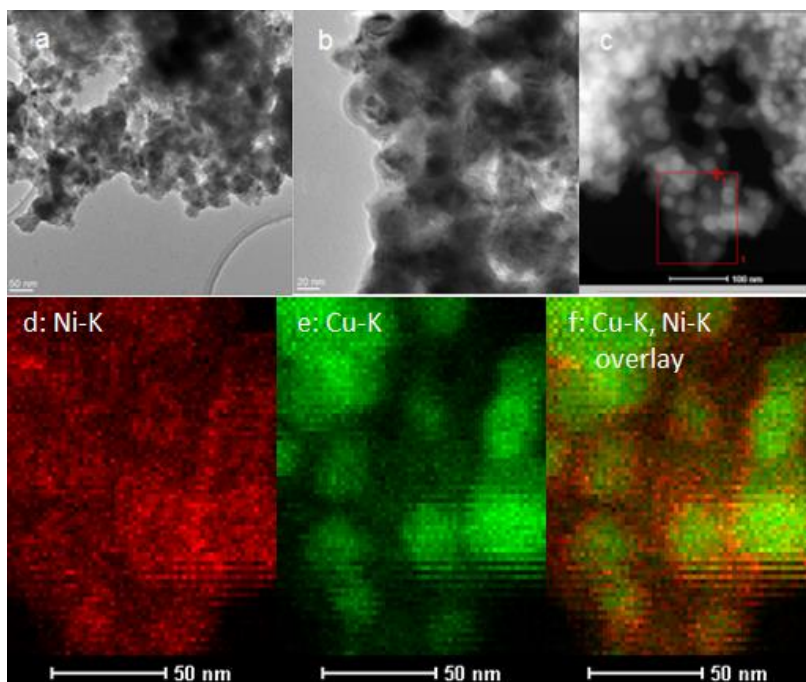


Figure 37: Nanostructures obtained after IPL Sintering using initial Ni^{2+} with a concentration of 20 mM; (a) TEM micrograph, (b) HRTEM micrograph, (c) STEM, (d) Ni-K maps, (e) Cu-K maps and (f) Cu-K and Ni-K overlaid micrographs.

4) Stability of Cu on Silicon

The aim of this work is to provide an alternative to the silver-based pastes currently used in the mass production of crystalline silicon solar cells. However, the diffusivity of Cu into Si is known to be rapid in comparison to other elements such as silver. Therefore, if the Si is left unprotected Cu can diffuse to the p-n junction and shunt the device; resulting in a drop in cell efficiency. The diffusion of Cu in to Si follows an Arrhenius relationship as a function of temperature. Based on Fick's first and second law the effective diffusivity of Cu in Si is governed by Equation 18.⁵

$$D(\text{cm}^2/\text{s}) = 4.7 \times 10^3 \exp\left(\frac{-0.43\text{eV}}{k_B T}\right) \quad \text{Equation 18}$$

Where k_B is Boltzmann's constant and T is the temperature. In Si, Cu is known to diffuse rapidly through interstitial sites, forming positively charged ions (Cu^+) at these positions. Consequently, it acts as a single electron donor in silicon, resulting in charge compensation in p-type Si. Substitutional diffusion of Cu on the other hand has been reported to be a significantly slower process. The solubility of Cu in Si is low and upon slow cooling it is found to precipitate near the surface, while fast cooling leads to the formation of Cu precipitates through the bulk of the material.^{5, 203-204} In addition the formation of Cu silicide's has been observed at temperatures as low as 200°C , resulting in a change in the material's electrical performance.²⁰⁵

Figure 38 shows the thermoelectric power curves for the Si, Si/Cu and Si/Cu-Ni samples as a function of the temperature. The results were normalized to their thermoelectric power at 300 K, $((S_T - S_{300\text{K}})/S_{300\text{K}})$. The temperature behavior of each sample is typical for a doped semiconductor. At room temperature, the density of the holes

is larger than that of the intrinsic electrons and holes, giving rise to a positive thermo power. As the temperature increases ionization of the remaining acceptor atoms initially causes an increase in the thermo power due to the promotion of additional holes (the Fermi level moves towards the valence band edge).

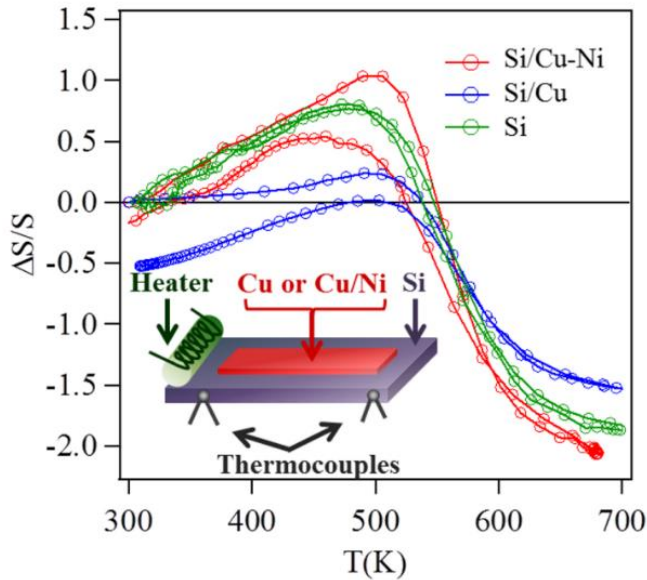


Figure 38: Normalized thermoelectric power curves for the Si, Si/Cu and Si/Cu-Ni samples as a function of the temperature. The inset shows the setup for measuring the thermoelectric power.

As the temperature increases further, the density of intrinsic holes and electrons becomes greater than that of the donor holes (extrinsic) causing the Fermi level to move towards the center of the bandgap. However, the electrons have a higher mobility than the holes in Si; therefore, contribution of the intrinsic electrons to the thermo power is greater than the intrinsic holes. Thus, at a certain temperature the thermo power changes sign, indicating that the transport is dominated by the intrinsic conduction of electrons that are thermally excited across the bandgap rather than the donated holes. Cu can also donate charge carriers to the semiconductor; as such the thermoelectric properties of the wafer are changed. Upon cooling the thermoelectric properties of the bare Si wafer does not change,

indicating no physical or chemical changes to the material have occurred. The Si/Cu sample on the other hand, demonstrates a large difference in its thermoelectric properties from its initial conditions; with a lower thermo power upon cooling. This indicates that Cu has diffused into the Si and the possible formation of Cu silicide. Comparatively the Si/Cu@Ni shows very little to no change in its thermo power after heating, indicating that the Ni barrier layer is impeding Cu diffusion into the Si.

C. Summary

In summary, a new economical process was developed for the room temperature synthesis Cu₂O-NiO core-layer nanostructures. While the second stage, involves controlling the Ni layer thickness by variation of the reactant concentrations (Ni(NO₃)₂ and NaBH₄). Densification of the Cu₂O@NiO core-layer film (fabricated by spray coating) and removal of the native oxide using the intense pulsed light sintering process is the final stage of the fabrication process. Lastly, the mitigation of Cu diffusion by the Ni layer has been investigated.

CHAPTER 5: IPL PROCESSING OF $\text{Cu}_2\text{NO}_3(\text{OH})_3$ ENHANCED WITH FRUCTOSE AND GLUCOSE TO FABRICATE ELEMENTAL Cu

A. Introduction

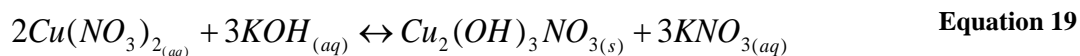
In this chapter, a room temperature aqueous synthesis of a copper precursor has been developed to aid in the solution stability of an ink and to enhance the transformation into bulk copper with the IPL process because applications in printed electronics and renewable energy technologies have shown a growing demand for scalable copper and copper precursor inks. The alternative copper precursor ink of copper nitrate hydroxide, $\text{Cu}_2(\text{OH})_3\text{NO}_3$, was aqueously synthesized under ambient conditions with copper nitrate and potassium hydroxide reagents. Films were deposited by screen-printing and subsequently processed with Intense Pulsed Light. Through the IPL process, copper nitrate hydroxide was successfully converted into cupric oxide (CuO) or elemental Cu, depending on the ink composition. The $\text{Cu}_2(\text{OH})_3\text{NO}_3$ quickly transformed in less than 30 seconds using forty (2 ms, 12.8 Jcm^{-2}) pulses into CuO. At higher densities the sintering improved the bulk film quality. For the direct formation of Cu, a reducing agent was required that wouldn't hamper prospects as a scalable commercial process. Therefore, the simple sugars fructose and glucose were added to the inks as organic molecule decomposition creates a reducing environment during IPL processing. Fructose and glucose were chosen as they are readily available chemicals that can increase the viscosity of the inks and are thermally decompose below 200°C , well before the temperature range where copper nitrate

hydroxide becomes thermally unstable near 300°C. The mechanisms of the synthesis, chemical and physical transformation, and reduction of copper nitrate hydroxide are thoroughly studied XRD, SEM, FTIR, and UV-Vis, which will lead to a pathway toward the scalable production of conductive copper thin films.

B. Results and Discussion

1) *Synthesized Copper Nitrate Hydroxide*

The synthesis was designed to be simple and faster than a copper oxide synthesis while avoiding the addition of large organic molecules, harsh reducing agents, and polymers. The synthesis of copper nitrate hydroxide is favorable over the synthesis of copper hydroxide as it provides a lower thermal decomposition temperatures of 236-280°C (copper nitrate hydroxide)¹¹⁶ and 400°C (copper hydroxide)¹¹⁰. The technique utilizes the drop-wise addition of an aqueous potassium hydroxide solution into an aqueous solution of copper salt generating a localized increase in hydroxide ions surrounded by a much larger nitrate ion concentration, leading to the formation of $\text{Cu}_2(\text{OH})_3\text{NO}_3$ and prevention of $\text{Cu}(\text{OH})_2$ formation. The coppers are coordinated through either two OH^- groups or an OH^- group and a NO_3^- group.¹¹² The reaction proceeds at ambient conditions, with copper (II) nitrate hemipentahydrate ($\text{Cu}(\text{NO}_3)_2 \cdot 2.5 \text{H}_2\text{O}$) and potassium hydroxide reagents to form the $\text{Cu}_2(\text{OH})_3\text{NO}_3$ as shown in Equation 19.



To confirm the presence of different material phases, X-Ray Diffraction (XRD) was employed. XRD analysis of the as synthesized deposits displayed the strongest peak at $2\theta=12.36^\circ$ (d-spacing of 6.93 Å). There was no apparent peak at 16.7135° (5.30 Å) (ICDD 00-013-0420), eliminating the presence of $\text{Cu}(\text{OH})_2$. Although copper hydroxide

hydrate's, $\text{Cu}(\text{OH})_2 \cdot \text{H}_2\text{O}$, peak of 13.3294° (6.637 \AA) (ICDD 00-042-0638) was similar, the results aligned more closely with the copper nitrate hydroxide, $\text{Cu}_2(\text{OH})_3\text{NO}_3$ peak of 12.8045° (6.9078 \AA) (ICDD 01-075-1779) (Figure 39a). The presence of copper nitrate hydroxide was also indicated by the UV-Vis absorption spectrum as the sample produced a broad peak ranging from approximately 550 nm – 850 nm (with a maximum at 650 nm) (Figure 39b). The increase in optical adsorption peak was consistent with the Cu(II) complex findings reported in the literature.^{16, 171} The increase in optical absorbance is advantageous for the IPL process, which relies on the absorption of visible light to initiate localized heating leading to decomposition and sintering. That enhancement mitigates the decreased absorbance, which would typically be seen when using an alternative precursor as observed with similar copper(II) salt structures.¹⁷¹

SEM micrographs of the synthesized $\text{Cu}_2(\text{OH})_3\text{NO}_3$ showed an assortment of morphologies (spherical, rod, platelet) (Figure 39c). However, optimization to obtain a narrow dispersion of particle size and morphology was not a priority of this work since the focus is the mechanics of the IPL process of $\text{Cu}_2(\text{OH})_3\text{NO}_3$ to produce a Cu film where the IPL process is intended to modify the morphology of the deposited ink.

Further characterization of the $\text{Cu}_2(\text{OH})_3\text{NO}_3$ was carried out through thermogravimetric analysis (TGA) (Figure 39d). The first peak at 160°C is attributed to the weight loss of adsorbed water at approximately 17 wt%, which is similar to the value of 158°C observed in the literature.²⁰⁶ The remaining weight change of approximately 30% from 160°C to 250°C represented the thermal decomposition of $\text{Cu}_2(\text{OH})_3\text{NO}_3$ to CuO which is in agreement with reported values.¹¹⁴

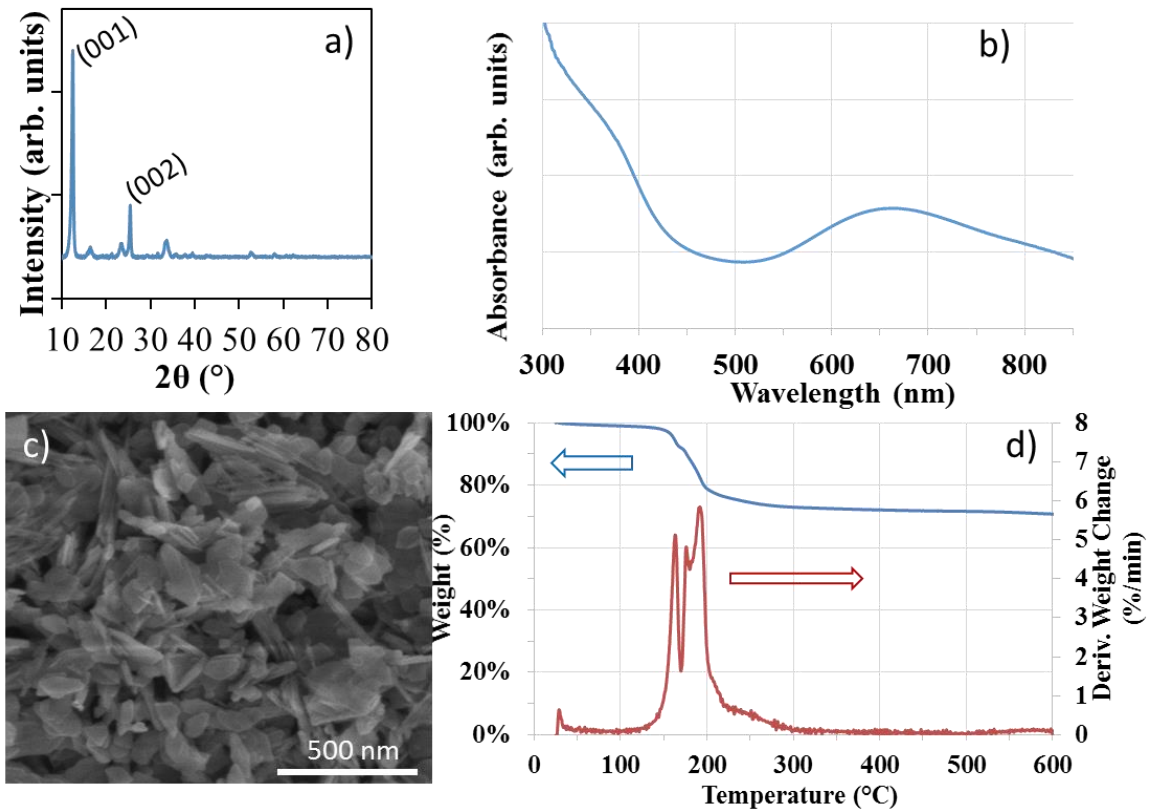


Figure 39: Characterization of synthesized copper nitrate hydroxide a) XRD b) Absorbance c) SEM d) TGA

2) Establishment of Baseline Conversion to CuO

The as synthesized $\text{Cu}_2(\text{OH})_3\text{NO}_3$ was deposited as a screen printed film and subsequently subjected to IPL Processing, wherein a localized rise in temperature was induced. This increase in temperature is high enough to both desorb water and convert the $\text{Cu}_2(\text{OH})_3\text{NO}_3$ to CuO. The initial pulses are used to remove the adsorbed water, which occurs within the first five and 10 pulses as show in Figure 40. Following water desorption, the $\text{Cu}_2(\text{OH})_3\text{NO}_3$ begins to undergo conversion as described by Equation 12 and Equation 13.

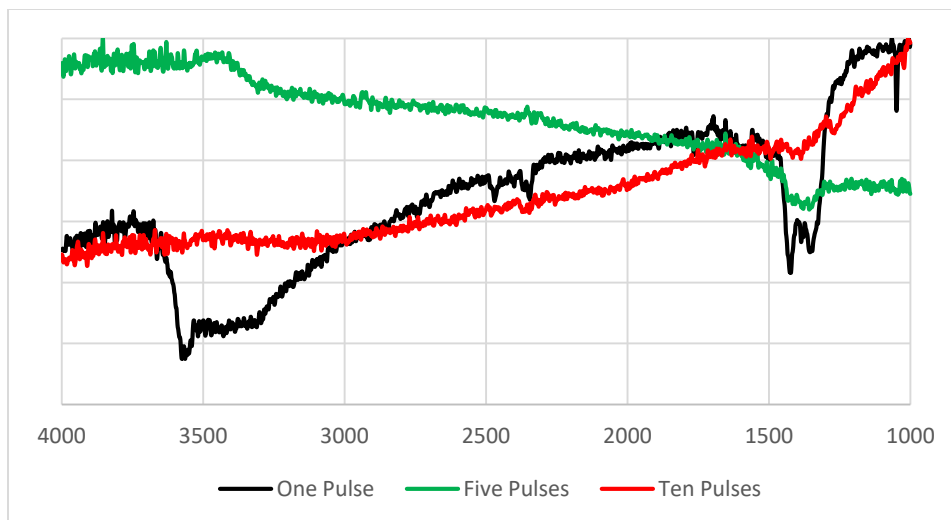


Figure 40. FTIR of $\text{Cu}_2(\text{OH})_3\text{NO}_3$ with one (black), five (green), and ten (red) 12.8 Jcm^{-2} pulses of IPL processing

The samples visually changed from a pale blue to black as the process proceeded, which serves as a visual indicator of the transformation of $\text{Cu}_2(\text{OH})_3\text{NO}_3$ to CuO . The $\text{Cu}_2(\text{OH})_3\text{NO}_3$ transformation into CuO throughout the IPL process was monitored using XRD analysis (Figure 41a). The IPL processed at an energy density of 10.1 Jcm^{-2} showed significant change in the crystal lattice to CuO . At an energy density of 12.8 Jcm^{-2} , at similar pulse number and rate, only trace amounts of $\text{Cu}_2(\text{OH})_3\text{NO}_3$ were present. At 19.2 Jcm^{-2} , the $\text{Cu}_2(\text{OH})_3\text{NO}_3$ peaks are no longer present. At higher energy densities than 19.2 Jcm^{-2} , there is little variation in the crystal structure.

The resulting CuO films displayed significant sintering and melting with increasing energy density as shown in the SEM micrographs (Figure 41B). Little to no changes were observed to the sintering with the application of forty 10.1 Jcm^{-2} pulses, though partial conversion to CuO were observed in the XRD. At an energy density of 19.1 Jcm^{-2} (Figure 41c), significant sintering was observed and, in certain areas of the film, melting.

Furthermore, at an energy density of 35.7 Jcm^{-2} , vast areas of melting of the CuO are observed.

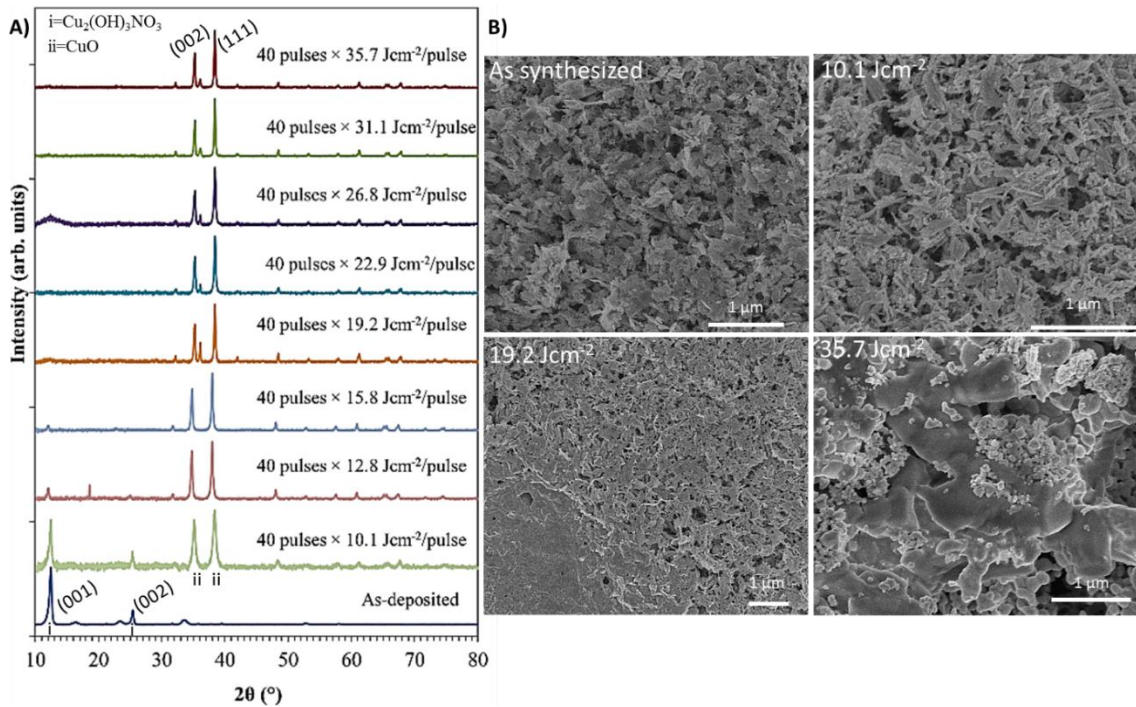


Figure 41: A) XRD results with IPL processing of forty pulses at increasing energy densities B) SEM images of IPL processed copper nitrate hydroxide films with forty pulses at varying energy densities

3) Direct Fabrication of Elemental through Intentional Inclusion of Fructose and Glucose for Enhanced IPL Processing

The aim of this study was to investigate the potential for $\text{Cu}_2(\text{OH})_3\text{NO}_3$ as an alternative precursor for conductive copper that requires conversion to elemental copper. According to Equation 12 and Equation 13, the direct conversion to of $\text{Cu}_2(\text{OH})_3\text{NO}_3$ to elemental Cu was not expected nor was it observed. However, it has been shown previously that conversion of CuO and Cu_2O during the IPL process to Cu can be achieved through the addition of reducing agents. The direct conversion of $\text{Cu}_2(\text{OH})_3\text{NO}_3$ can also be accomplished in the presence of a hydrogen atmosphere as modeled by Equation 20.

Four hydrogen atoms in total are needed to isolate the copper atoms. The hydrogen atoms integrate with the nitrate group and three hydroxyl groups to transform to form nitric acid and water, respectively.



The previous section showed that the oxidation of $\text{Cu}_2(\text{OH})_3\text{NO}_3$ occurred rapidly with CuO emerging at an energy density of 10.1 Jcm^{-2} , which was the lowest energy density used in this work. Therefore, the most efficient formation of copper requires that the reducing environment be induced prior to significant transformation of $\text{Cu}_2(\text{OH})_3\text{NO}_3$ to CuO. The direct conversion of $\text{Cu}_2(\text{OH})_3\text{NO}_3$ to Cu would be favorable, as it would decrease the energy needed for conversion when compared to energy to convert into CuO and then reduce CuO into Cu. A reducing environment can be established through the decomposition of organic molecules. (Table 2) Therefore, it would be desirable to utilize organic molecules, which are abundant and cost efficient, and environmentally friendly. These criteria are met by both fructose and glucose.

An analogous atomic representation of the overall transformation of $\text{Cu}_2(\text{OH})_3\text{NO}_3$ with fructose or glucose leads to Equation 21, as both fructose and glucose have the same atomic structure (though differ in their molecular structure which leads to varying material properties). According to equation 5, the molar ratio of $\text{Cu}_2(\text{OH})_3\text{NO}_3$ to monosaccharide is 18:1, setting the minimum amount of monosaccharide at 3.18 wt% to $\text{Cu}_2(\text{OH})_3\text{NO}_3$. A 10 wt% monosaccharide concentration was used due to the high viscosity printing requirements, which is more than sufficient to create the reducing atmosphere upon decomposition. The decomposition leads further into smaller organic molecules throughout the process. One of the main decomposition products is formic acid.²⁰⁷ The reduction

reaction for $\text{Cu}_2(\text{OH})_3\text{NO}_3$ be represented as Equation 22. Equation 22 is similar to a Cu_2O reduction mechanism from the literature.²⁰⁸

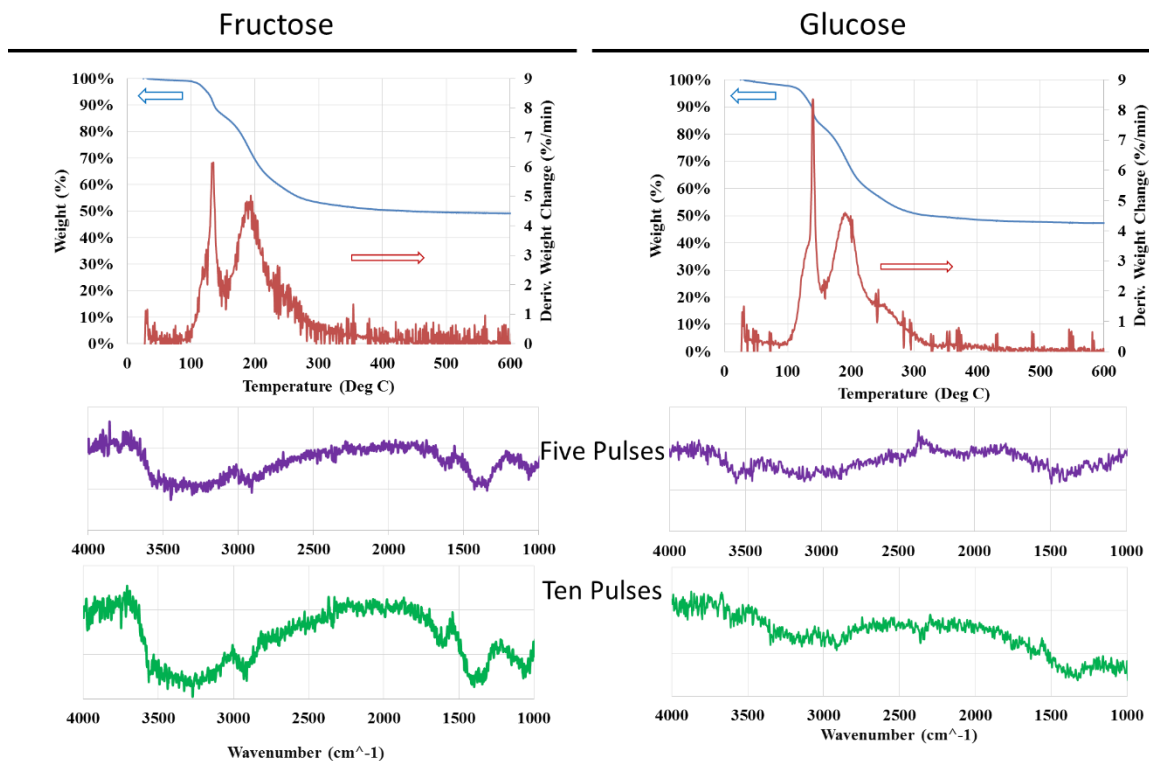


Figure 42: TGA and then the FTIR 12.8 Jcm⁻² IPL processed fructose (left) and glucose samples (right)

The most important differences between fructose and glucose for this study were the thermal decomposition temperature, enthalpy of decomposition, and resulting byproducts. Thermogravimetric analysis (TGA) helped to identify how these differences affect the $\text{Cu}_2(\text{OH})_3\text{NO}_3$ reduction (Figure 42). During the TGA analysis both the fructose and glucose samples displayed a similar behavior or weight change throughout the 150°C to 220°C range. The fructose sample had an additional weight change from 100°C to 120°C followed by a more rapid weight change from 125°C to 145°C. The largest peak is

attributed to fructose in 125°C to 145°C range. The glucose sample had very similar peaks though the peak was observed at 175°C compared to 145°C for the fructose sample. The observed temperature difference of approximately 30°C is comparable to literature value differences of the thermal decomposition temperatures with 138.7°C (fructose) and 166.4°C (glucose) resulting in a 27.7°C difference.²⁰⁹ The reported values are higher than the literature values as the thermal decomposition temperatures are known to vary with the heating rate.²⁰⁹ The observed weight losses (53% for fructose and 55% for the glucose) were larger than the 30% weight loss during conversion to CuO. The increased weight loss was anticipated as the transformation of $\text{Cu}_2(\text{OH})_3\text{NO}_3$ to CuO versus Cu differs with an oxygen atom, the weight loss associated with the decomposition of fructose and glucose, and varying water contents in the samples.

Fructose is known to thermally decompose ($\Delta H_{\text{rxn}}=11.09$ kcal/mol) into glyceraldehyde and 1,3-dihydroxyacetone while glucose ($\Delta H_{\text{rxn}}=12.06$ kcal/mol) decomposes into erythrose and glycolaldehyde.²¹⁰ To confirm the formation of decomposition products by observing aldehyde and carboxylic groups, specific FTIR was performed with lower IPL processing than used anywhere else in the study with only five and ten pulses at an energy density of 12.8 Jcm^{-2} being applied. FTIR analysis primarily displayed peaks characteristic of fructose and glucose with O-H bonds ($3500\text{-}3200 \text{ cm}^{-1}$) and C-C alkane bonds ($3000\text{-}2800 \text{ cm}^{-1}$). With five and ten 12.8 Jcm^{-2} IPL pulses, the formation of characteristic bonds for the fructose and glucose decomposition, such as aldehyde and carboxylic acid groups ($1750\text{-}1650 \text{ cm}^{-1}$), began to emerge. The $\text{Cu}_2(\text{OH})_3\text{NO}_3$ peaks of bonded O-H, $\text{Cu}_2(\text{OH})_3\text{NO}_3$ (1421 cm^{-1} , 1047 cm^{-1} , N-O bonds (1384 and 872 cm^{-1}) also became more readily observed (Figure 43). The observed O-H

bonds peaks showed a decreasing trend and an emergence of new peaks within the 1750 cm^{-1} - 1650 cm^{-1} range. These peaks are characteristic of functional groups containing double bonded oxygen molecules (aldehydes and carboxylic acids). The presence of these peaks, at a relatively low total energy input of this study, suggests that the decomposition is happening prior to the conversion of copper hydroxide nitrate and leading towards a reducing environment.

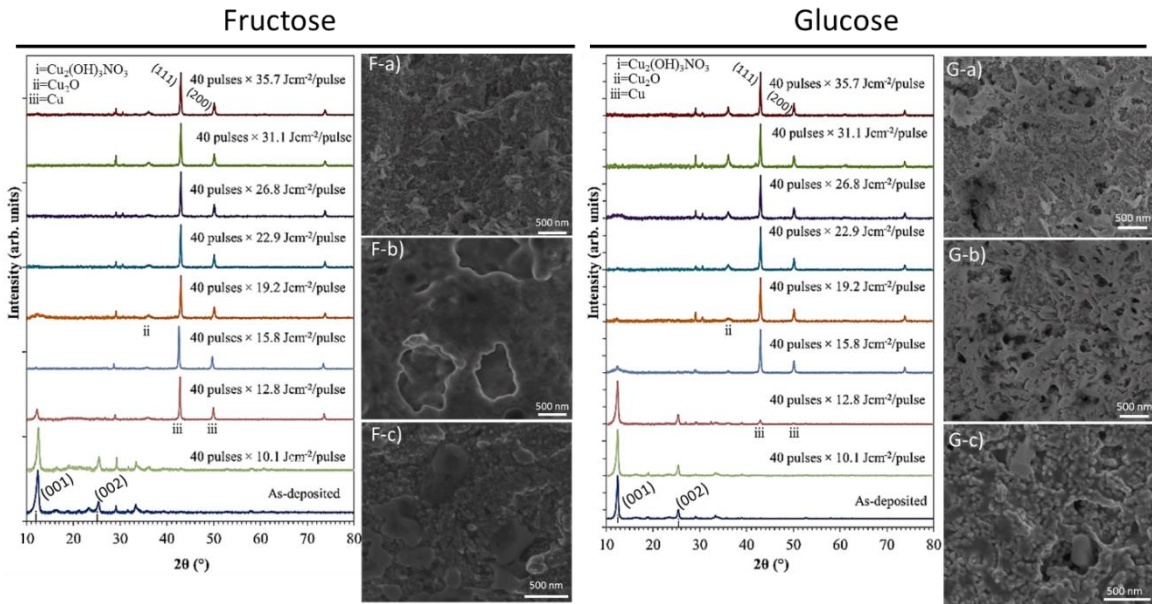


Figure 43: XRD results with IPL processing of forty pulses at increasing energy densities for fructose (left) and glucose (right). SEM images of fructose (F-a-c) and glucose (G-a-c) samples at different energy densities of IPL processing a) 12.8 Jcm^{-2} c) 15.8 Jcm^{-2} c) 35.7 Jcm^{-2}

The conversion to Cu happened at an IPL energy density of 12.8 Jcm^{-2} for fructose and 15.8 Jcm^{-2} for glucose as shown with XRD in Figure 43 as the strongest XRD peaks became 43.472 (111), 50.373 (200), and 73.995 which are consistent with the crystalline structure of Cu (ICDD 00-001-1241). The XRD analysis did not show a significant presence of either Cu₂O or CuO during the IPL reduction process. Trace signs of Cu₂O

can be seen in the XRD though they are associated with copper's exposure to oxygen/water in the atmosphere.

Higher IPL energy densities were studied to characterize the sintering of the formed films. Since the fructose samples had an earlier conversion to Cu, a higher degree of sintering was observed in the fructose samples (Figure 43F-a-c) when compared to the glucose samples (Figure 43G-a-c) at the same energy density. At an energy density of 12.8 Jcm^{-2} , SEM images of the fructose sample (Figure 43F-a) and glucose samples (Figure 43G-a) begin to show a slightly higher porosity than the deposited films as the organic molecule decomposition leads to gas evolution and disruption of the films. At an energy density of 15.8 Jcm^{-2} , the fructose sample (Figure 43F-b) show a higher degree of sintering and melting towards a bulk film while the glucose samples (Figure 43G-b) only have particle necking present and still maintain a resemblance to the deposited films. At an energy density of 35.7 Jcm^{-2} , both the fructose sample (Figure 43F-c) and glucose samples (Figure 43G-c) have a lower degree of porosity as the IPL processing provides the energy to sinter the Cu films.

4) Sheet Resistance of Produced Conductive Cu Films

As the fructose samples displayed the preferable results with an earlier onset of copper nitrate hydroxide converting into copper, the sheet resistance for these samples were measured throughout the IPL process. (Figure 44) The sheet resistance of the films continued to decrease as the intensity of the pulse was increased with a sheet resistance of $0.224 \Omega/\square$ at 35.7 Jcm^{-2} . The bulk resistivity of the films can be found by the product of the sheet resistance and the film thickness ($\rho = tRs$), incorporating a thickness of $5.59\mu\text{m}$,

the bulk resistivity for the 35.7 Jcm^{-2} sample is $1.251 \cdot 10^{-4} \Omega \cdot \text{cm}$; within two magnitudes of bulk copper's resistivity. The resistivity was lower than that of bulk copper, which can be attributed to the porosity of the deposited films. Porosity of the films was caused by the volume change going from $\text{Cu}_2(\text{OH})_3\text{NO}_3$ to Cu and organic decomposition reactions leading to gas evolution.

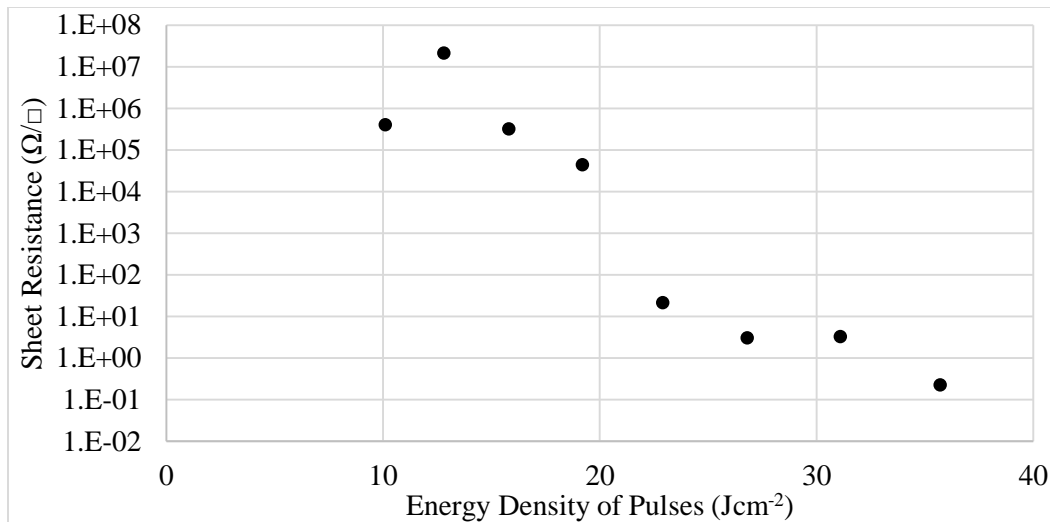


Figure 44: Sheet Resistance of IPL processed fructose films with forty pulses at varying energy densities.

C. Summary

In summary, the $\text{Cu}_2(\text{OH})_3\text{NO}_3$ was formed through aqueous room temperature reaction with a copper salt and potassium hydroxide, which was deposited with screen-printing. With inclusion of fructose or glucose, the materials transformed with IPL Processing to create conductive copper. A Copper oxide intermediary was not observed during Cu formation and fructose provided a faster reduction than glucose.

CHAPTER 6: REDUCTION OF GRAPHENE OXIDE NANOSHEETS AND $\text{Cu}(\text{OH})_2$ NANOWIRES VIA INTENSE PULSED LIGHT PROCESSING

A. Introduction

In this chapter, graphene oxide (GO) films have been subjected to IPL Processing to cause their rapid reduction, which is indicated through changes in transparency, sheet resistance, and the Raman I_D/I_G peak ratio. The addition of $\text{Cu}(\text{OH})_2$ NWs to the inks has also been shown to increase the performance of resultant films with lower sheet resistances.

B. Results and Discussion

1) Process Overview for IPL Processing of GO

The main techniques used to study the effectiveness of IPL Processing to reduce the graphene oxide has broken down into three main steps: 1) Ink Preparation, 2) Spin Coating Deposition, and 3) IPL Processing. (Figure 45) The reductive transformation of the GO to rGO is displayed as a shift in color from yellowish-brown to grey/black. The ink was prepared by dispersing synthesized GO into ethanol (which is preferable to water for spin-coating deposition due to its lower surface tension). A second GO ink was made with fructose (10 wt% of GO), as previous IPL work done in our lab observed that fructose in the ink aided reduction (of copper nitrate hydroxide to copper), to investigate if the reduction of GO could also be aided. Fructose enhanced the reduction capabilities of IPL processing due to it decomposing and creating a reducing environment.¹⁷⁰ Spin Coating

deposition was then utilized at six different spin speeds. At each spin speed, three IPL Processing Energy inputs were applied. Additionally, lower sheet resistances were found with the samples containing fructose, which led to an additional analysis to understand how the transparency and sheet resistance of the films were changing with an IPL processing at eleven IPL Processing Energy inputs (with the redundancies).

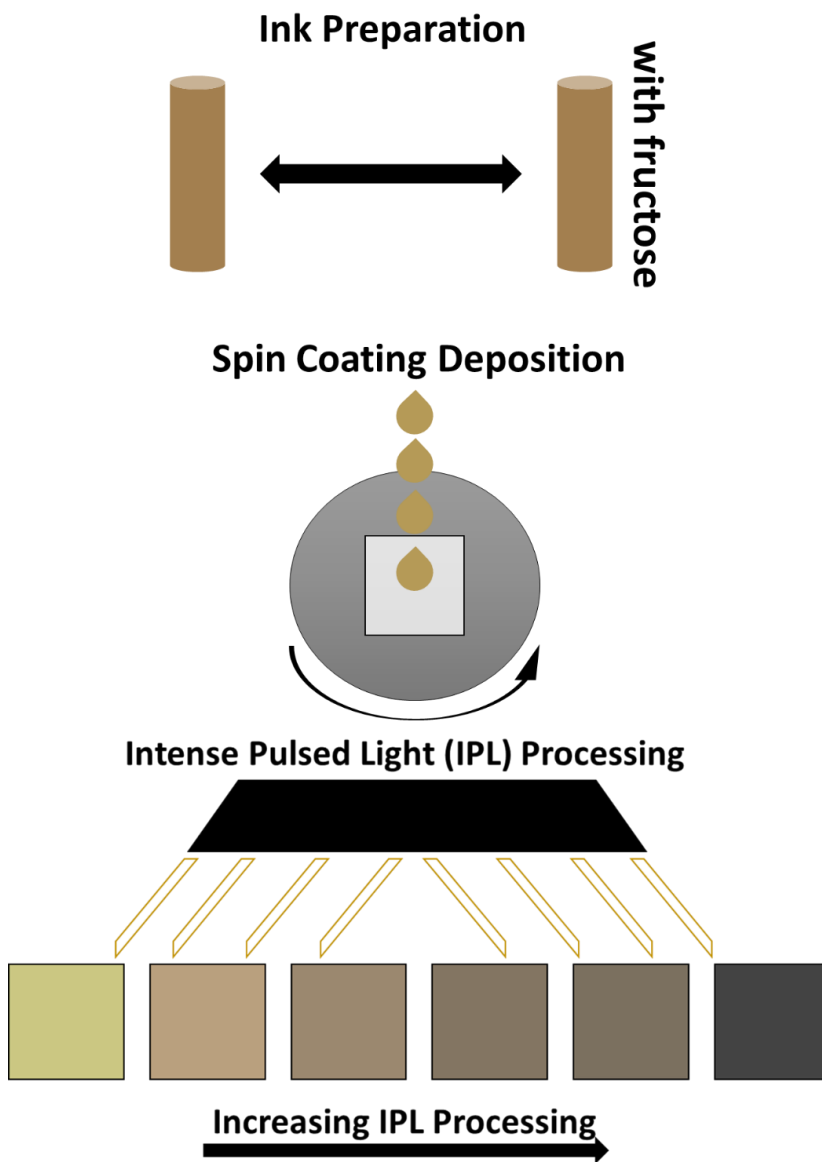


Figure 45: Overview schematic of spin-coated graphene oxide depositions and IPL processing

Simultaneous thermogravimetric analysis and differential scanning calorimetry (SDT) of the as synthesized GO was performed. (Figure 46) The sample showed a significant weight loss through 150°C due to the water content. Above ~162°C through ~718°C, the heat flow had positive yet lower absolute values. The highest heat flow per weight observed was at ~200°C.

The film thickness of the samples was measured at the six different spin speeds. (Figure 47) Higher spin speeds led to thinner films, due the increased centripetal forces. The samples that were created with the solution containing fructose displayed smaller film thickness values and had smaller deviations. This can be attributed, in part, due to the creation of more uniform films, as fructose acts as a binder, increasing film adhesion during deposition. Optical transparency (550 nm) of the films also increased with increased spin speeds, as the transparency is a function of the film thickness. (Figure 48) The addition of fructose only slightly altered the deposited films, which was anticipated due to the relatively small quantity of fructose added to the ink. It is interesting that the addition of fructose appeared to contribute to the deposition process, as it was introduced as a means to enhance the effectiveness of the IPL Processing through its decomposition. Here it is seen that the additive of fructose can play a dual role throughout the process, aiding in both the spin-coating deposition and IPL Processing. A deeper understanding of how the viscosity, surface tension, substrate adhesion, and extent of GrO nanosheet separation could prove beneficial to further development of smooth films.

SEM images of the different spin speeds for samples containing fructose (Figure 49). The images show that there is presence of sheet stacking and, therefore, multiple layers of GO. Additionally, lower spin speeds had better surface coverage.

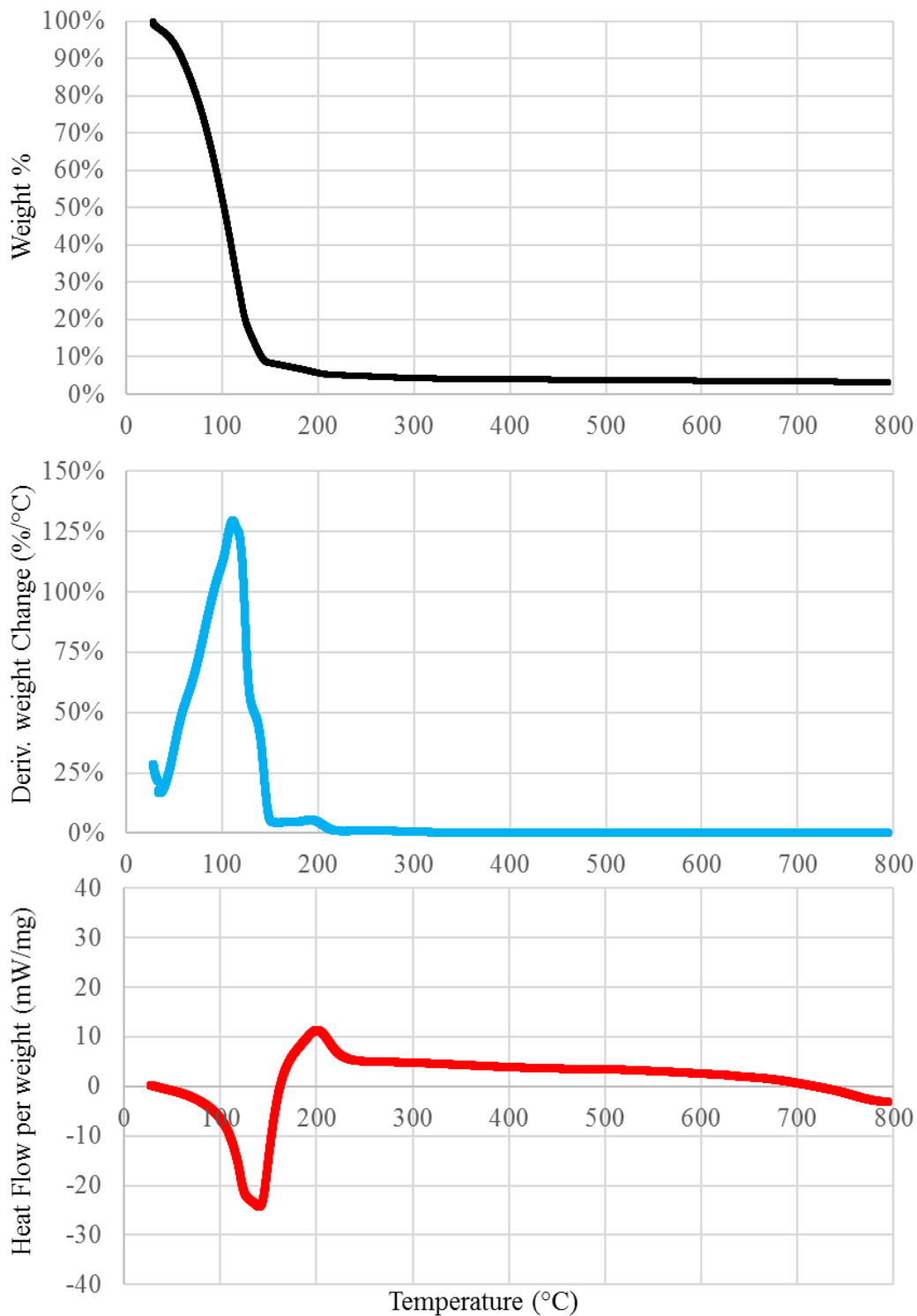


Figure 46: SDT of the as synthesized GO weight% (top), first order derivative of the weight% with respect to temperature (middle), and the heat flow normalized by the weight (bottom)

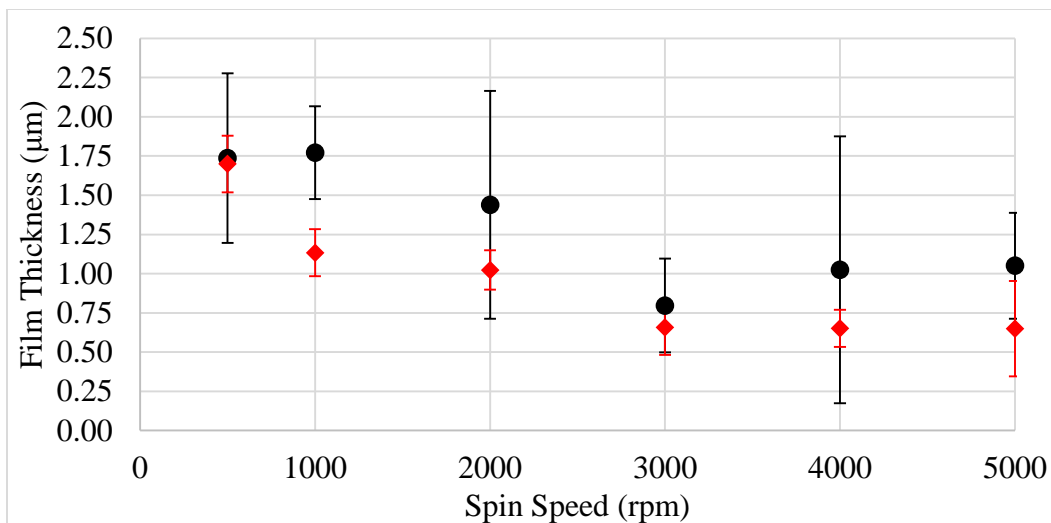


Figure 47: Film thickness of the as deposited GO films (black circles) & with fructose (red diamonds)

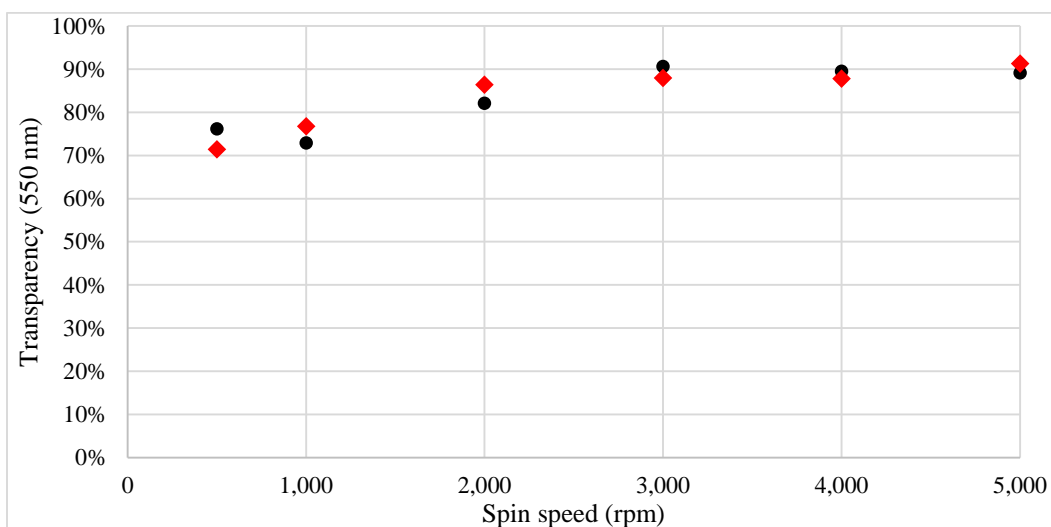


Figure 48: Transparency of deposited GO films (black circles) & with fructose (red diamonds)

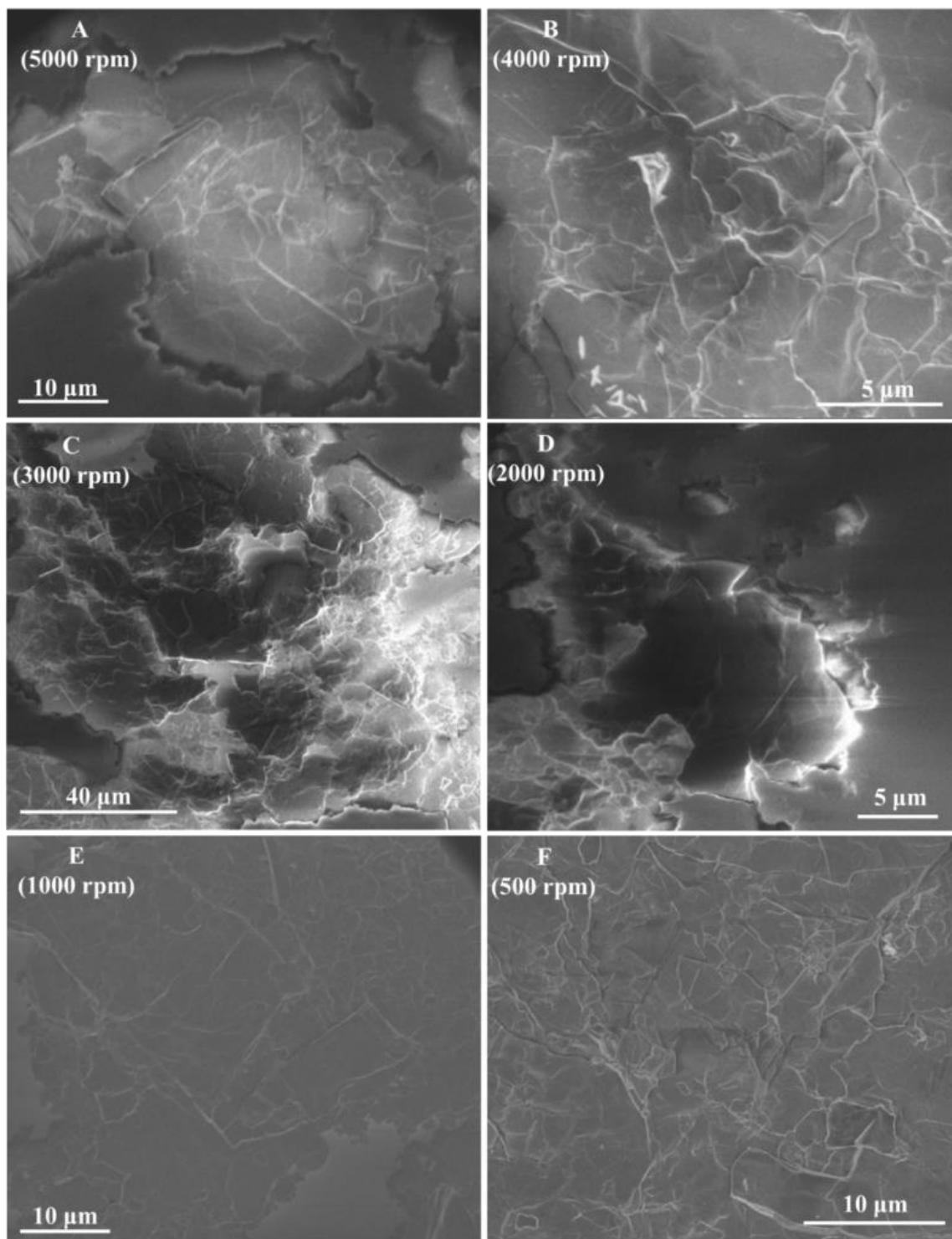


Figure 49: SEM Images of as deposited GO samples (with fructose) A) 5,000 rpm B) 4,000 rpm C) 3,000 rpm D) 2,000 rpm E) 1,000 rpm F) 500 rpm

2) Reduction of GO with IPL Processing

Sheet resistance of the samples after IPL processing samples was measured (Figure 50). The sheet resistance was found to decrease with decreasing spin speeds. The addition of fructose produced lower sheet resistances, indicating higher performance. Without fructose, the sheet resistance of samples without fructose could not be accurately measured above 2,000 rpm due to the limitations of the equipment's compliance range. The 500 rpm samples did not have conclusive results, which can be attributed to uneven film deposition at such low spin speeds.

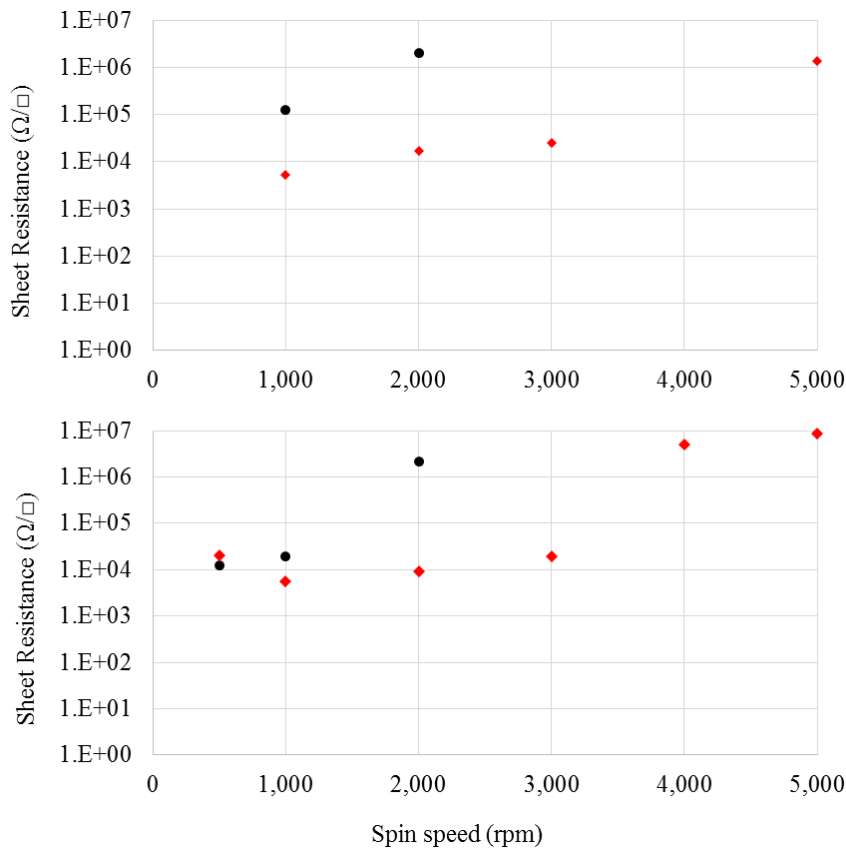


Figure 50: Comparison of sheet resistance IPL Processing Energy Density Inputs 1428 Jcm⁻² and 1744 Jcm⁻², for both samples without fructose (black circles) and with fructose (red diamonds).

SEM images of the GO films before/ after IPL Processing with forty 35.7 Jcm^{-2} pulses for spin speeds of 3,000 rpm and 1,000 rpm are displayed in Figure 51. It can be seen the high energy density pulses did alter the films, which could be attributed to outgassing of H_2O and CO_2 vapors from the rapidly increased localized temperatures.

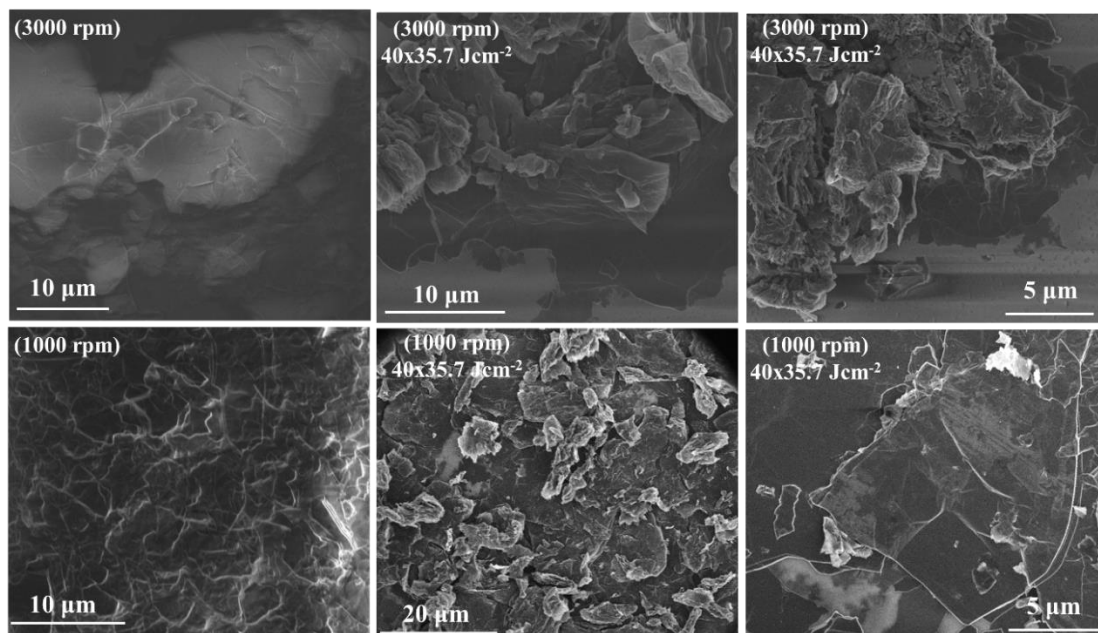


Figure 51: SEM images of spin-coated GO (without fructose) at 3,000 rpm (top row) and 1,000 rpm (bottom row). The corresponding as deposited samples shown firstly (left), followed by two images at different magnifications of the samples post IPL Processing (center and right).

Figure 52 displays the observed transparency of the samples at select IPL Energy Density inputs, which exhibit a red shifting of the absorbance with an increasing extent of IPL Processing. The increased absorption occurs due to the reformation of π - π bonds, which have higher energy, red-shifting the absorbance. This can be seen visually as the color changes from yellowish-brown to black. The increased absorbance is advantageous for IPL processing; as sequential IPL pulses will be more effective in contributing to the reduction. Qualitatively, the reduction's progress can be seen by a visual transformation of films from yellowish-brown to black.

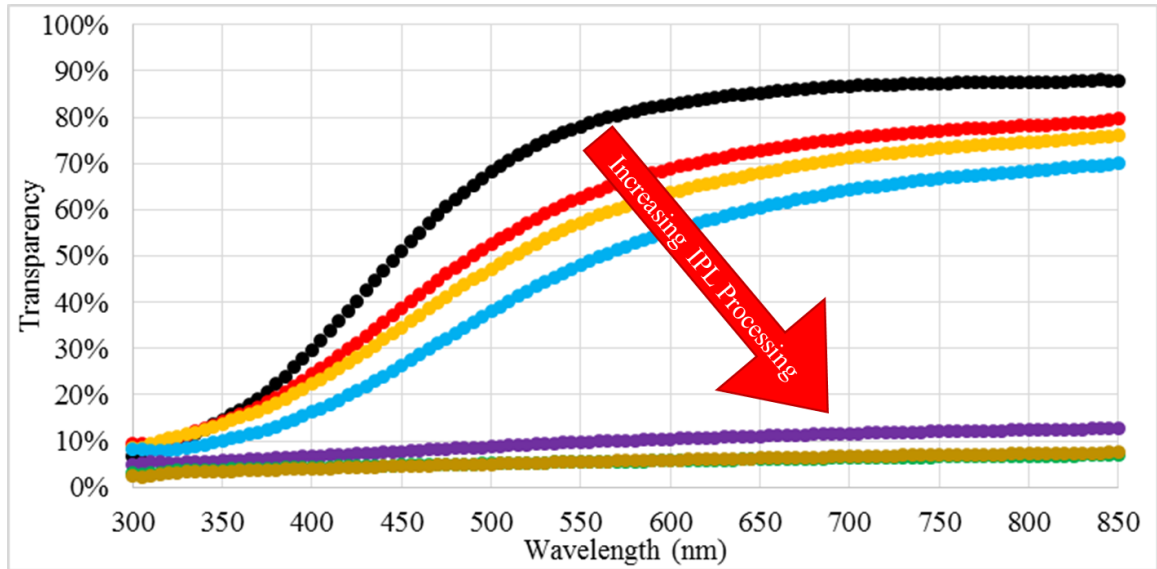


Figure 52: Transparency vs. Wavelength for 1,000 rpm spin-coated GO with fructose as deposited (black) and at several IPL Energy Density Inputs 178.5 Jcm⁻² (red), 357 Jcm⁻² (yellow), 632 Jcm⁻² (blue), 714 Jcm⁻² (purple), 1428 Jcm⁻² (green), and 1744 Jcm⁻² (brown).

Figure 53 displays the transparency, sheet resistance, and Raman I_D/I_G peak ratio for the 1,000rpm samples with fructose with varying amount of IPL processing, shown as total energy density. The transparency primarily displays a decreasing trend with increasing IPL processing. However, there is an observable ‘knee’ found in the transparency in between a total energy density of 632.0 Jcm⁻² and 714 Jcm⁻² with the transparency changing from 48.07% to 9.74%. This ‘knee’ has been observed in previous studies done in our lab for sheet resistance.^{106, 170} There was a corresponding knee of the sheet resistance, which decreased from 65.20 MΩ/□ to 20.11 kΩ/□.

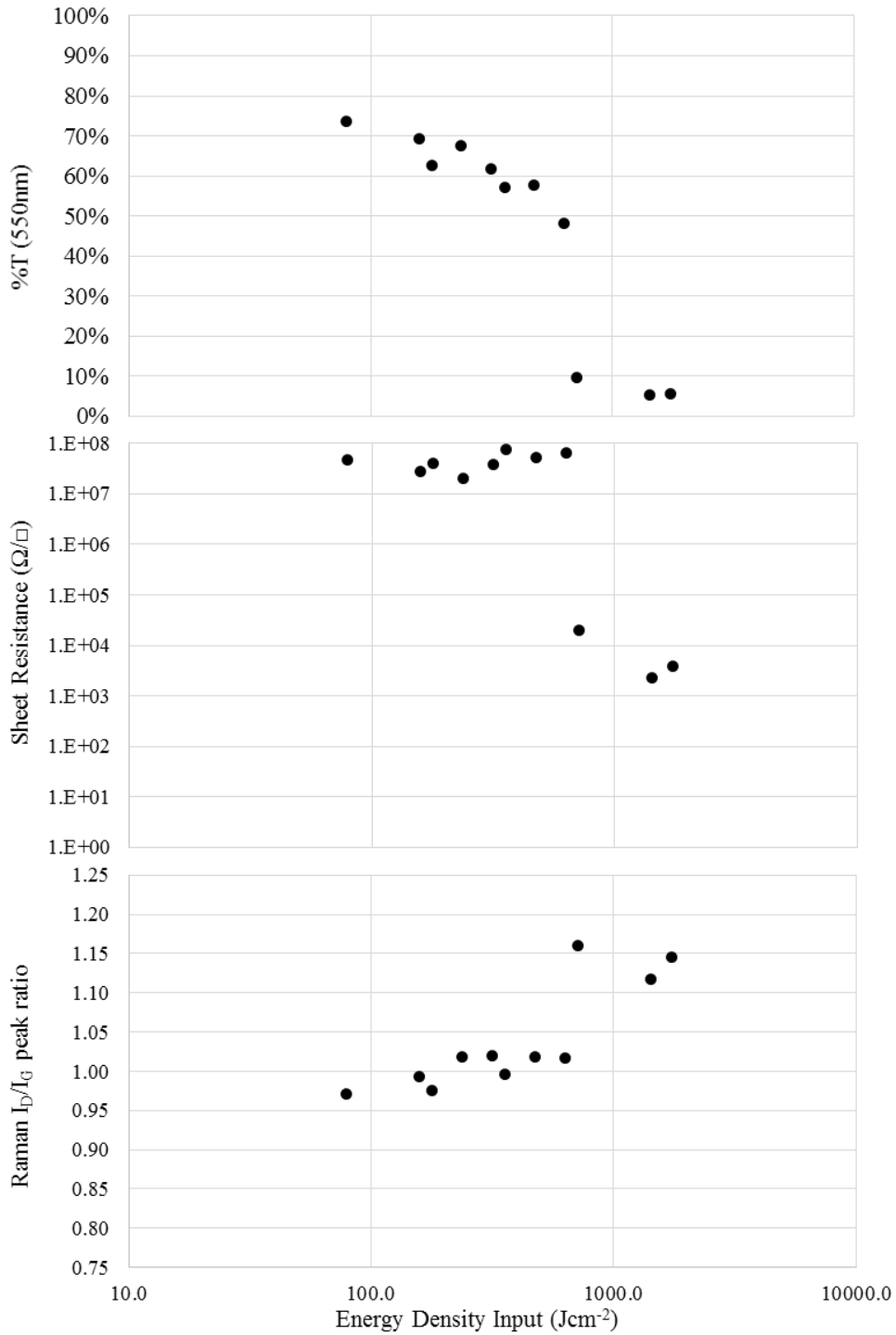


Figure 53: (Top) Transparency (Middle) Sheet Resistance and (Bottom) Raman peak ratio (I_D/I_G) with increasing total induced energy density through IPL Processing

Profilometry measurements of the film thickness was performed with increasing IPL Energy Density Inputs. (Figure 54) It can be observed that the higher IPL Processing Energy Density Inputs tended to also lead to an increased film thickness. Specifically, the data closest to the observed ‘knee’ of 714 Jcm⁻² and 1428 Jcm⁻² that had exhibited improved sheet resistance, but also exhibited nearly a four-fold to five-fold increase in film thickness and higher variations in thickness measurements.

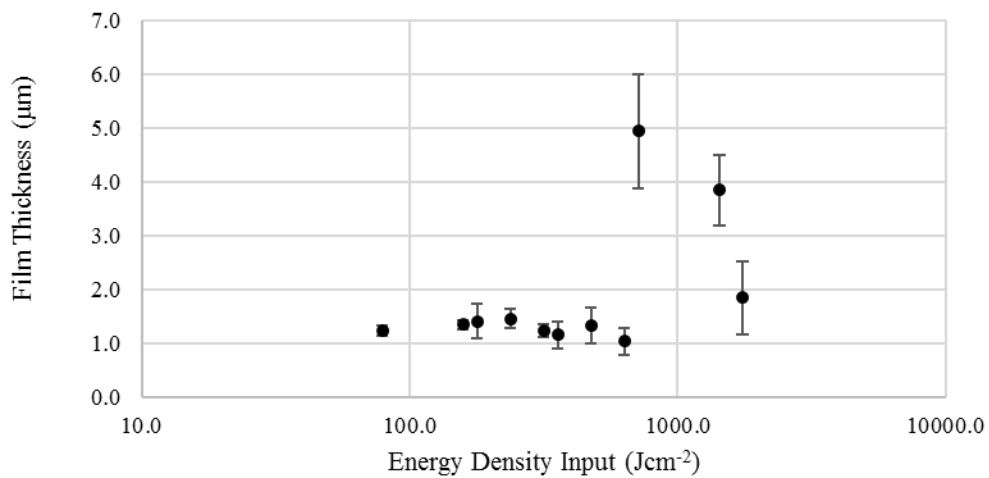


Figure 54: Film Thickness of 1,000 rpm spin-coated GO with fructose samples with increasing IPL Energy Density Input.

The film thickness increase indicates that the film morphology was modified during IPL Processing under these conditions. This was confirmed through SEM images of the films, which show that the films underwent a notable change in morphology. (Figure 55) However, the highest IPL Processing Energy Density Input of 1744Jcm⁻² did not have as drastic change in film thickness or morphology. This is because the IPL Processing was performed in an incremental fashion.

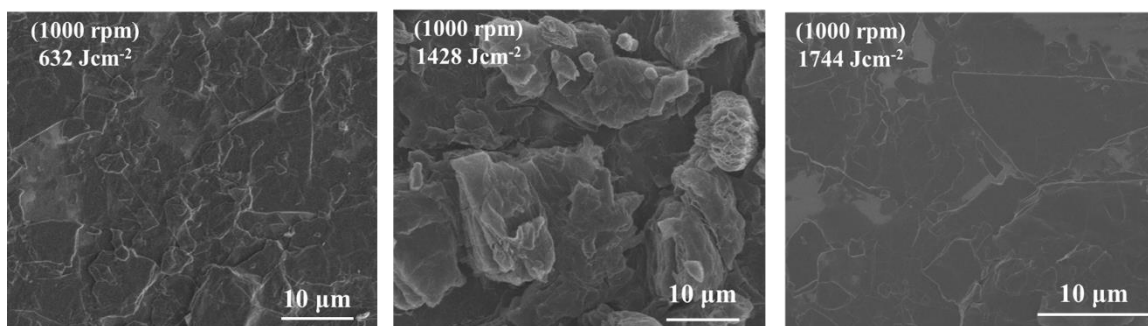


Figure 55: SEM imagery of 1,000 rpm spin-coated GO with fructose samples displaying film morphology at IPL Processing Energy Density Inputs of 632 Jcm^{-2} (left), 1428 Jcm^{-2} (center), and 1744 Jcm^{-2} . It is noted that the IPL processing of the 1744 Jcm^{-2} sample was done with an incremental IPL Processing scheme, which resulted in maintaining the nanosheets' orientations.

The use of step-wise increases of the Energy Density utilized for Incremental IPL Processing helped to preserve the film thickness and morphology because it gradually heats the films prior to the onset of the organic decomposition. The lower Energy Density pulses help to remove the residual water of the deposited GO. Then, as the Energy Density of the pulses continue to be increased step-wise, the reduction can proceed gradually. The reduction's gaseous products would less likely to delaminate the nanosheets from their horizontal orientation.

3) Demonstrated Use of Flexible Plastic for IPL Processing GO

Films

Plastic substrates are interesting for IPL Processing due to potential scalability to roll-to-roll, flexible processing. Plastic substrates differ glass during IPL Processing due to their lower thermal capacity and irreversible damage to the plastic itself if too high of a temperature reached. However, the lower thermal capacity is advantageous as less energy

is lost to the substrate as a heat sink, leading to a more efficient process through a significant decrease of IPL Processing needed to facilitate the GO reduction.

Figure 56 displays the results of the cellulosic plastic samples (TOPAS 6015). It should be noted that the films did have a degree of macroscopic non-conformity. It is noted that the energy densities of 15.8 Jcm^{-2} and 35.7 Jcm^{-2} did cause deformation of the plastic. The circular samples were thicker in the center as the vacuum suction of the substrates used during spin-coating to keep them in place affected the deposition process. The transparency of the samples displayed a 'knee', decreasing between the 10.1 Jcm^{-2} and 15.8 Jcm^{-2} total energy density, from 65.45% to 17.13%. The sheet resistance showed a complementary pattern to film transparencies as a significant decrease (four magnitudes) was observed in between the total energy densities of 10.1 Jcm^{-2} and 15.8 Jcm^{-2} ($62.5 \text{ M}\Omega/\square$ to $3.43 \text{ k}\Omega/\square$).

It was also important to show that the reduced films on flexible substrates had bending capabilities. This was done through a manual bending process while the film was an intermediary between a DC power supply and an LED. (Figure 57) The LED light continued illumination throughout manually bending the rGO film. Pictures are displayed below for the bending at three voltage settings (2.81 V, 8.13 V, and 15 V). Without the film, the LED turned on $\sim 1.5 \text{ V}$.

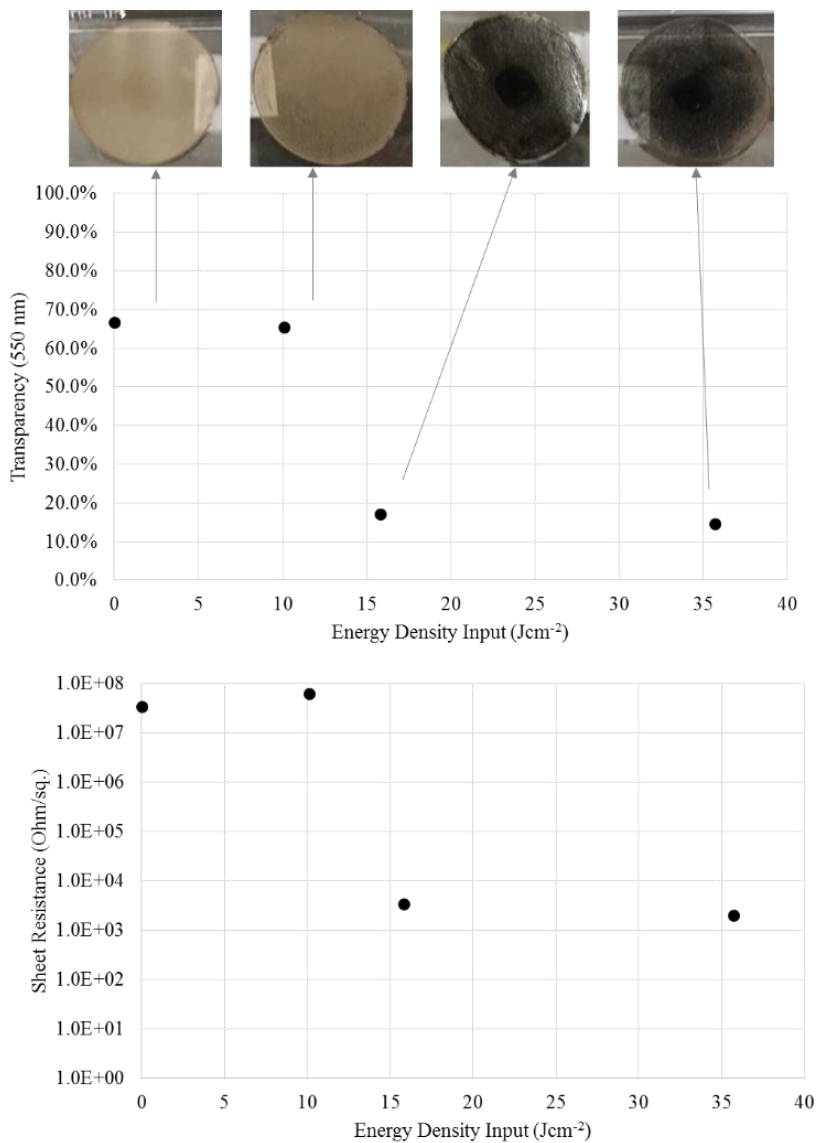


Figure 56: Cellulosic plastic sample (Top) film transparency and (Bottom) sheet resistance



Figure 57: Bending of cellulosic plastic sample connected to a red LED and a DC Power Source at 2.81 V (left) 8.13 V (middle) and 15.0 V (right)

4) Alternative Deposition Methods for Creation of GO Films

In this subsection, results from Ultrasonic Spray Deposition and Rod-coating GO are briefly displayed. Both of these deposition methods have a much higher potential for scaling to commercial applications than spin-coating. The GO as deposited films that made with Ultrasonic Spray Deposition had high optical transparency values, which decrease significantly with IPL Processing at an Energy Density Input of 1428 Jcm^{-2} . (Figure 58) These films all had measurable sheet resistance values (Figure 59), so their FOM could be calculated (Figure 60) with the highest value being close to the rGO FOM values discussed in Chapter 2. Additionally, average thickness measurements (Figure 61) showed that each pass resulted approximately 40.8nm film thickness, and SEM imagery showed that the film coverage was better for two passes. (Figure 62)

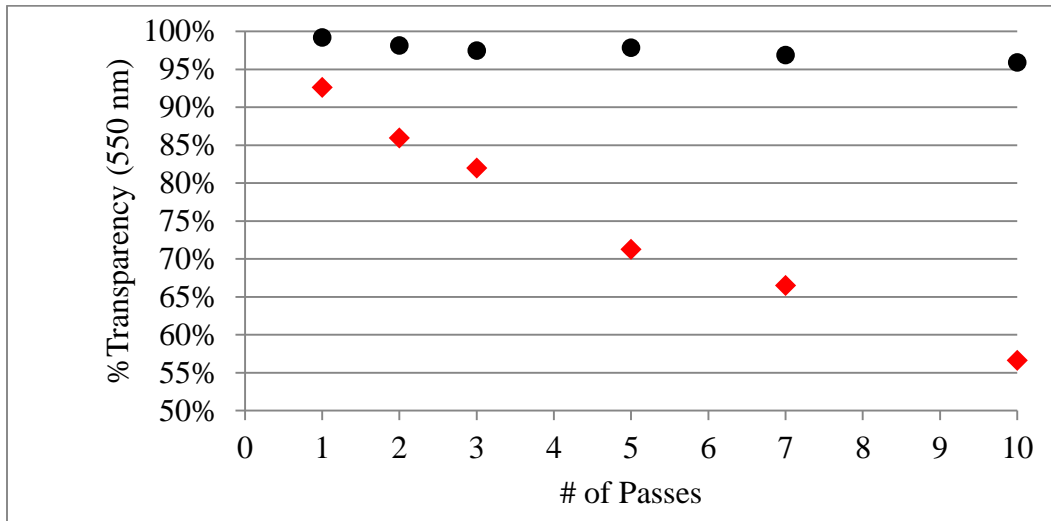


Figure 58: Transparency (550nm) vs. # of Ultrasonic Spray Deposition Passes of GO films as deposited (black circles) and after IPL Processing with a 1428 Jcm^{-2} Energy Density Input (red diamonds).

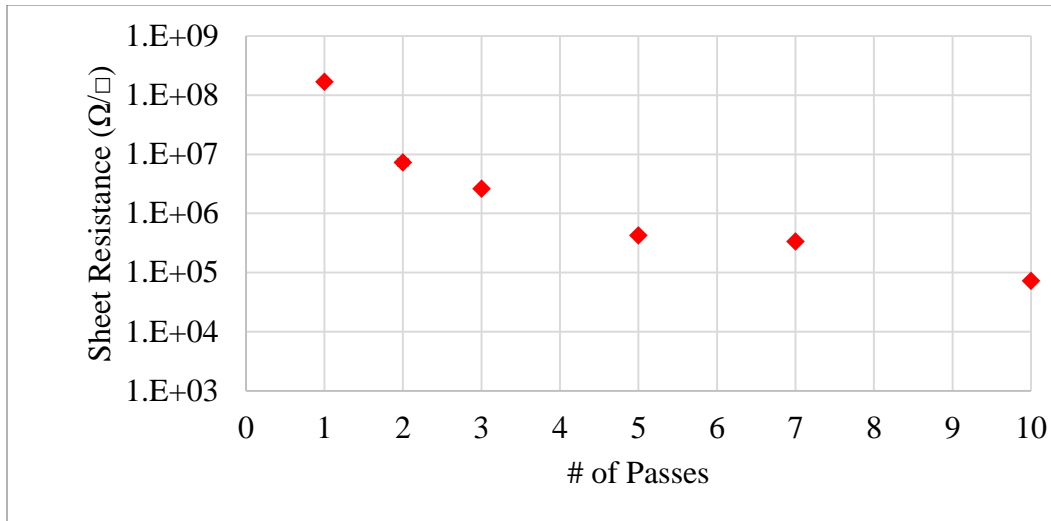


Figure 59: Sheet Resistance versus # of Ultrasonic Spray Deposition passes of GO films after IPL Processing with an Energy Density Input of 1428 Jcm⁻².

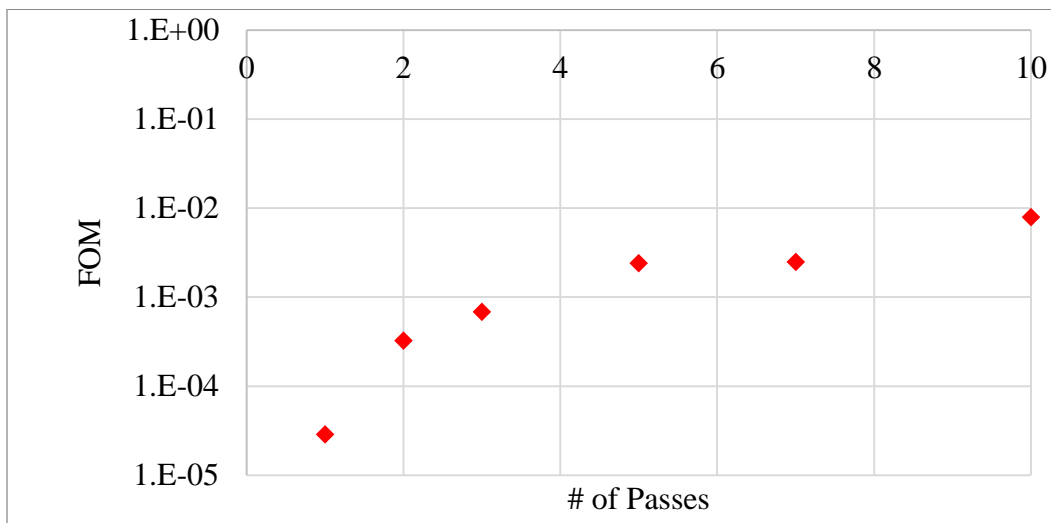


Figure 60: Calculated Figure of Merit (FOM) versus # of Ultrasonic Spray Deposition passes of GO films after an IPL Processing Energy Density Input of 1428 Jcm⁻².

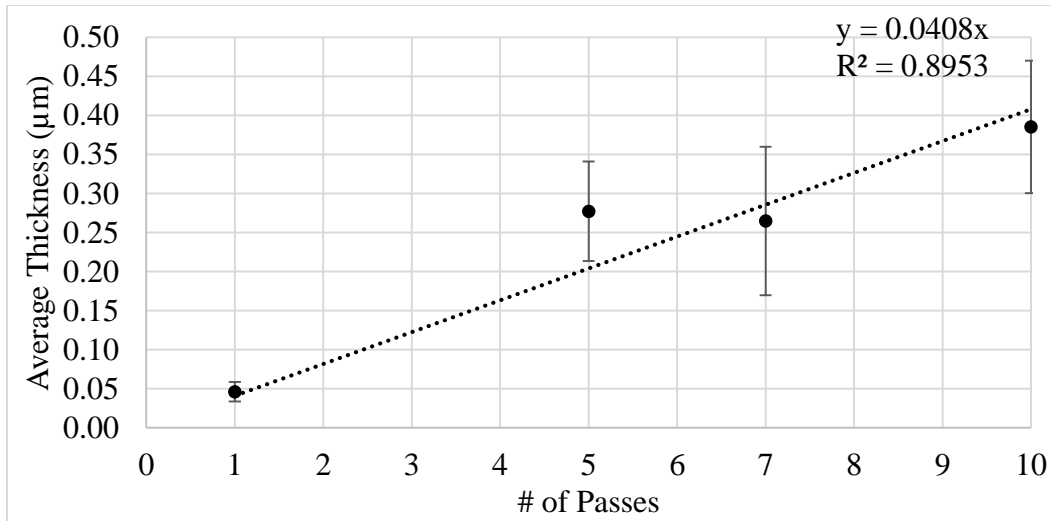


Figure 61: Average thickness versus # of Ultrasonic Spray Deposition Passes of GO films with error bars that indicate the standard deviation of measurements and featuring a trendline to display the observed linear relationship of the number of passes to the recorded average thickness of the films (y intercept set to zero).

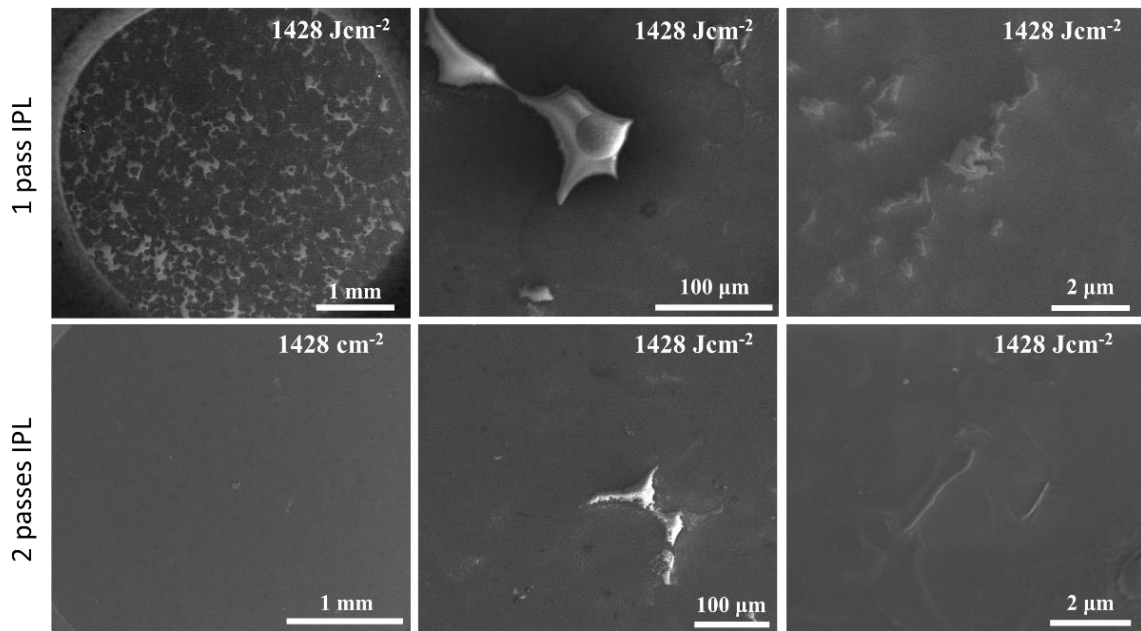


Figure 62: SEM Images of GO films fabricated with Ultrasonic Spray Deposition with 1 pass (top) and 2 passes (bottom) after IPL Processing with an Energy Density Input of 1428 Jcm².

Deposition of GO films with Rod-coating was performed on a flexible plastic. These films displayed extremely high optical transparency and also exhibited similar trends to spin-coated GO films with decreasing transparency with increasing IPL Processing Energy Density Input. (Figure 63)

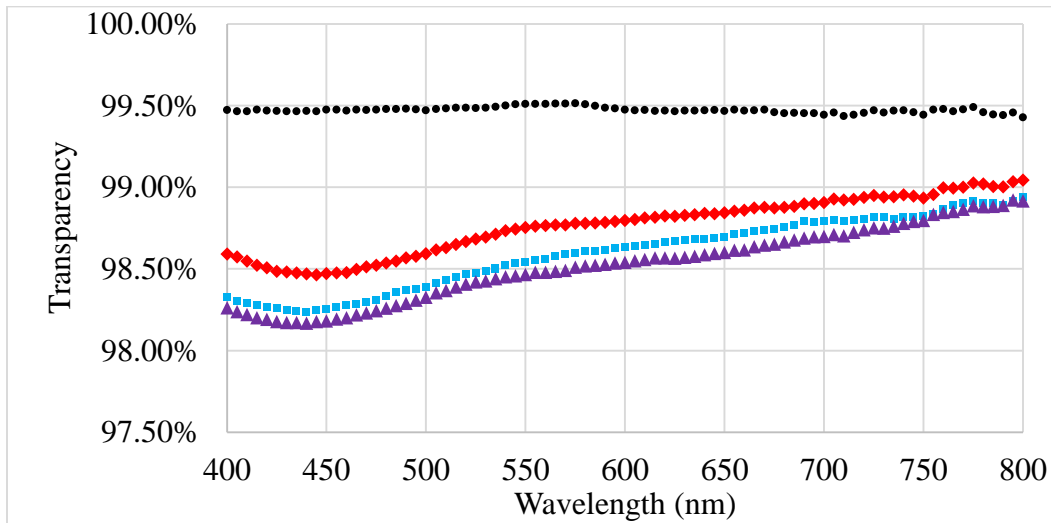


Figure 63: Transparency of Rod-coated GO films deposited on TOPAS 6015 with one pulse of varying Energy Density pulses of IPL Processing versus wavelength (400 nm - 800 nm). The as deposited film (Black) displayed the highest transparency over the region. The remaining three films displayed a lower transparency values with increased energy densities of 19.2 Jcm⁻² (second – red diamonds), 26.8 Jcm⁻² (third – blue squares), and 35.7 Jcm⁻² (forth/bottom – purple triangles).

5) $\text{Cu}(\text{OH})_2$ NWs for Implementation for Engineering Hybridized Films

SEM imagery of the as synthesized $\text{Cu}(\text{OH})_2$ NWs showed that they had diameters $\sim 10\text{nm}$ and lengths of $\sim 1\text{-}2\mu\text{m}$. (Figure 64) It can be seen that the NWs did tend to bundle/agglomerate and not discretely separated.

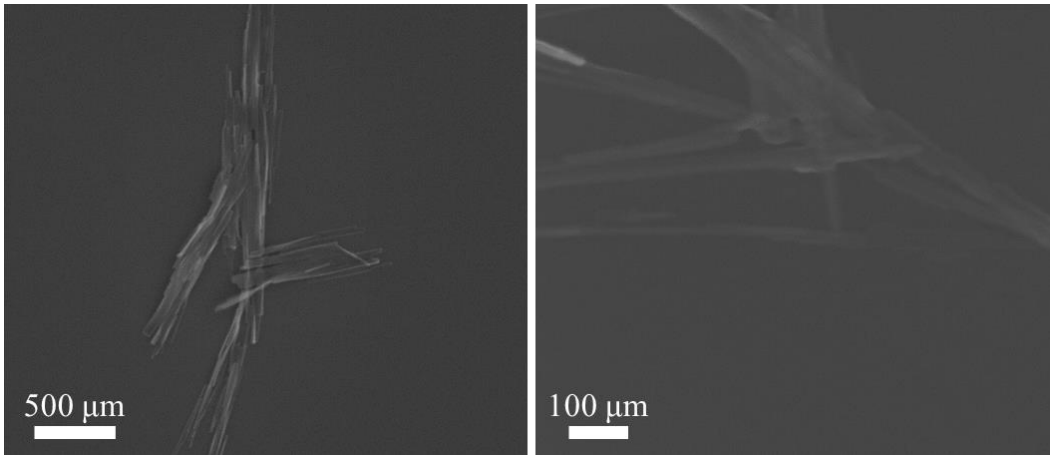


Figure 64: SEM images of as synthesized $\text{Cu}(\text{OH})_2$ NWs.

SDT of the as synthesized $\text{Cu}(\text{OH})_2$ NWs is displayed in Figure 65. The $\text{Cu}(\text{OH})_2$ NWs displayed a similar drop in weight to the as synthesized GO prior to $\sim 150^\circ\text{C}$, which can be attributed to water and ethanol. Between 150.90°C and 536.74°C , a positive heat flow per weight was observed meaning that the full reduction of $\text{Cu}(\text{OH})_2$ NWs to Cu is achieved at $\sim 536.74^\circ\text{C}$. Two peaks ($\sim 236^\circ\text{C}$ and 312°C) can also be seen within this range for both the derivative weight change and heat flow per weight, which indicates that there are multiple phase transitions during the temperature increase.

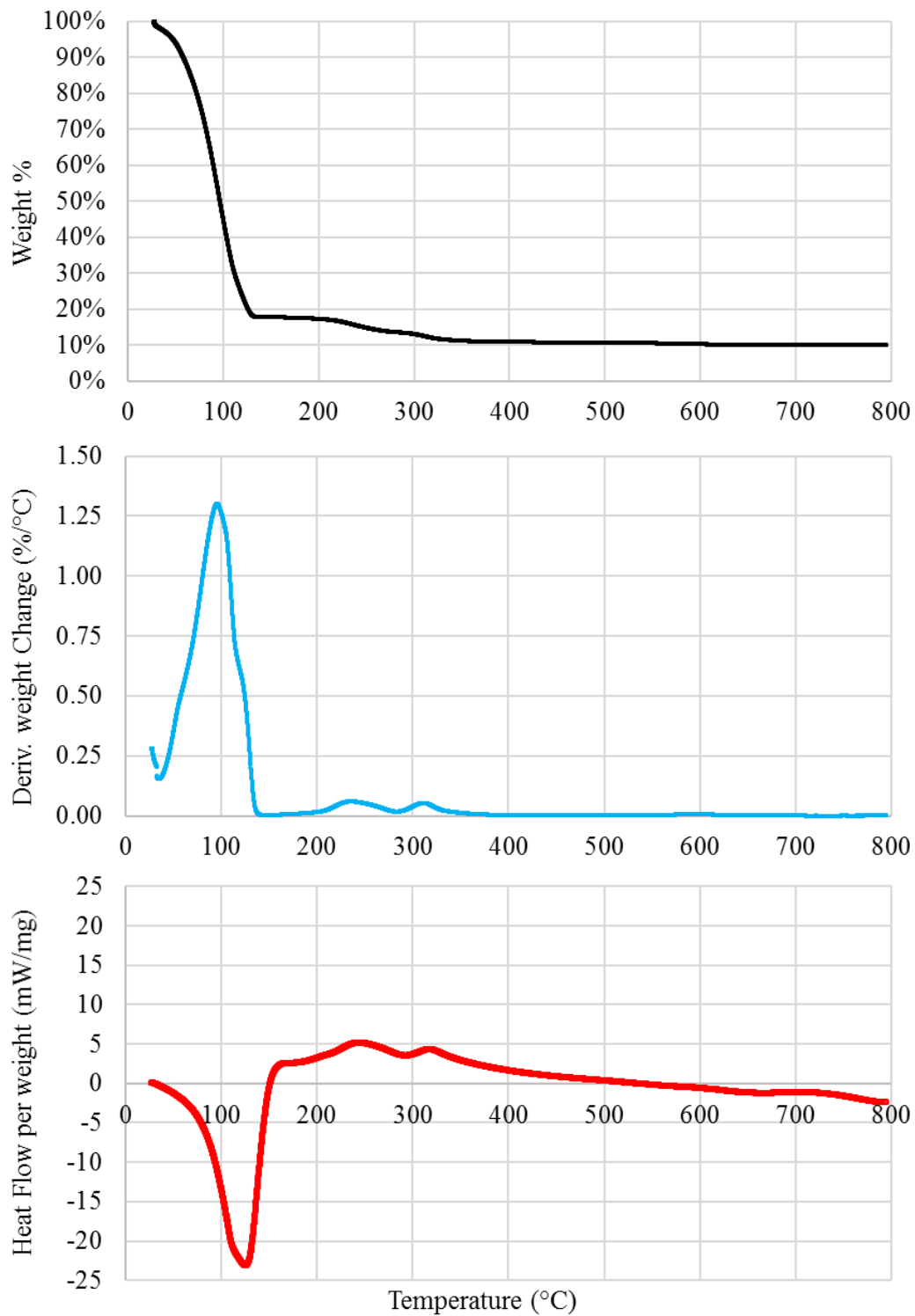


Figure 65: SDT of as synthesized $\text{Cu}(\text{OH})_2$ NWs with the weight% (top), first order derivative of the weight% with respect to temperature (middle), and the heat flow normalized by the weight (bottom).

6) *IPL Processing of Hybrid Films Deposited from Mixtures Containing GO and Cu(OH)₂ NWs*

The 15-20 mg/mL hybrid inks were created with concentrations of GO and Cu(OH)₂ of 68.35% GO, 91.53% GO, and 98.18% GO (by weight). After these inks were drop-casted and subsequently IPL Processed, they displayed lower sheet resistances with higher relative Cu concentrations. (Figure 66) This was anticipated due to the low sheet resistance of elemental Cu versus rGO.

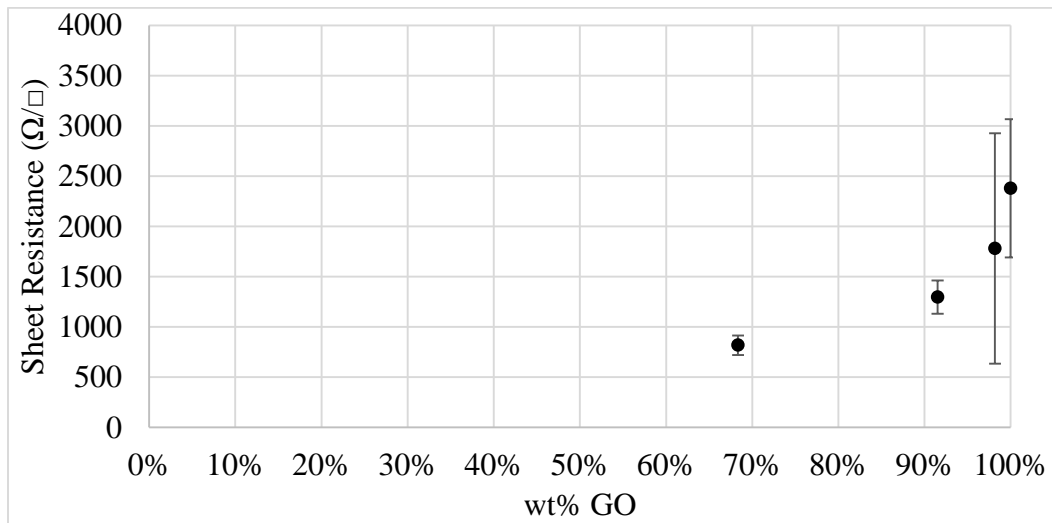


Figure 66: Sheet Resistance after 1744 Jcm⁻² Incremental IPL Energy Density Input versus wt% GO in solution.

Samples created by spin-coating at 500 rpm with pre-heated glass substrates at 80°C to create thicker films. They were then IPL Processed incrementally. Sheet resistances were measurable for mixtures of 68.35% GO at the four highest energy density inputs and 91.53% GO at only for the highest energy density input). (Figure 67) These samples were visually much thicker at their centers and that can be seen through the

contrast of the 68.35% GO sheet resistance measurements over different parts of the samples. (Figure 68)

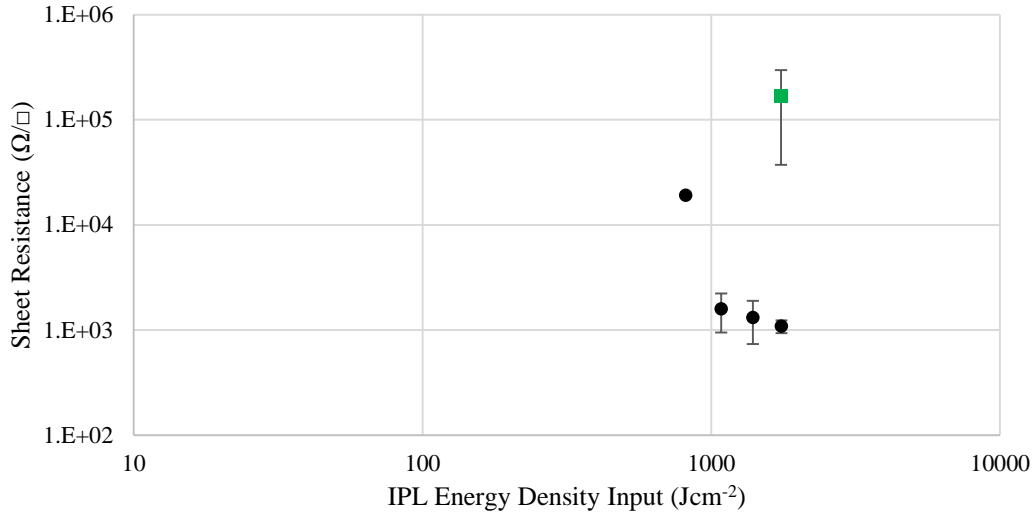


Figure 67: R_s comparison of spin-coated samples at concentrations of 91.53% GO (green squares) and 68.35% GO (black circles) versus IPL Energy Density Input.

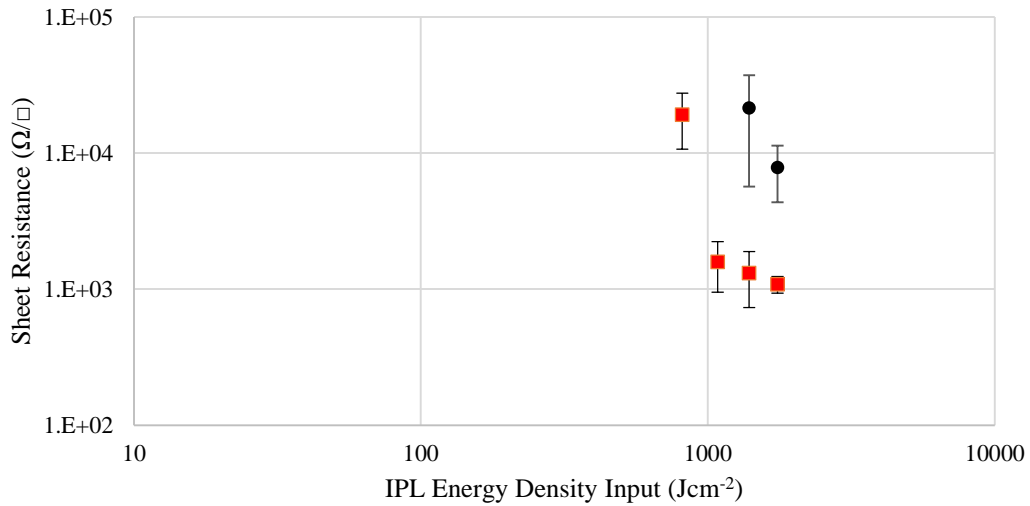


Figure 68: R_s comparison of spin-coated 68.35% GO at the center (red squares) and over the entire samples (black circles) vs. IPL Energy Density Input.

XRD was performed to confirm the reduction of $\text{Cu}(\text{OH})_2$ to Cu for the 68.35% GO ink concentration. (Figure 69) It was observed that the peak intensity of the main XRD

peak of Cu, which located at 43.2° (ICDD 00-004-0836), increased dramatically with higher IPL Processing energy density inputs.

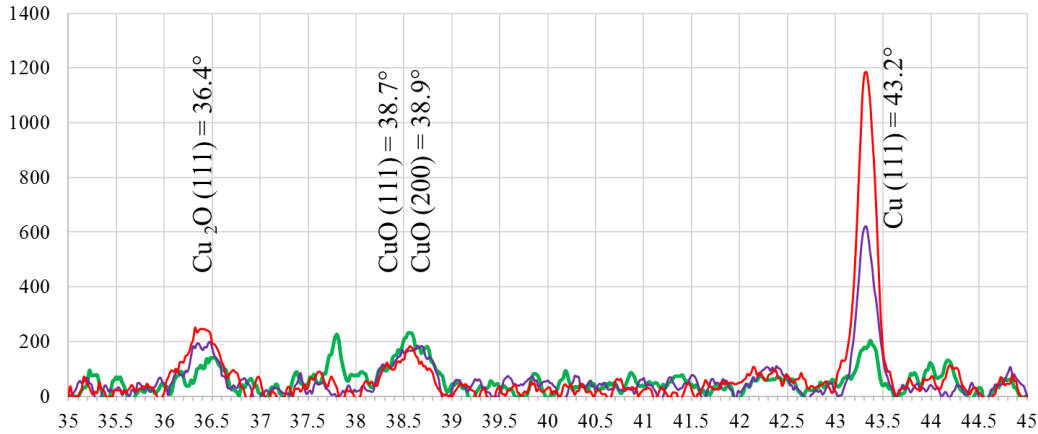


Figure 69: XRD of 68.35% GO vs. IPL Energy Density Inputs of 632 Jcm^{-2} (green), 1428 Jcm^{-2} (purple), and 1744 Jcm^{-2} (red).

The film morphology of 100% GO and 68.35% GO after incremental IPL Processing at a total energy density input of 1744 Jcm^{-2} was analyzed with SEM imagery. (Figure 70) It can be seen that the hybrid mixture's image hints at higher levels of material interconnectivity. This indicates that the Cu NWs trend of lower sheet resistance with increasing $\text{Cu}(\text{OH})_2$ NWs concentrations in the inks could be attributed to an enhancement of the electrical conductivity both from the presence of conductive Cu but also from connecting the nanosheets. The produced data had limited viability to describe the physics of a hybrid system due to the thickness of films needed for sheet resistance measurements. However, the further development of the hybridized system would need to explore the importance of contact resistance between rGO nanosheets and a Cu NWs and if there is Ohmic contact. The anticipated electrical resistances are shown below in Figure 71.

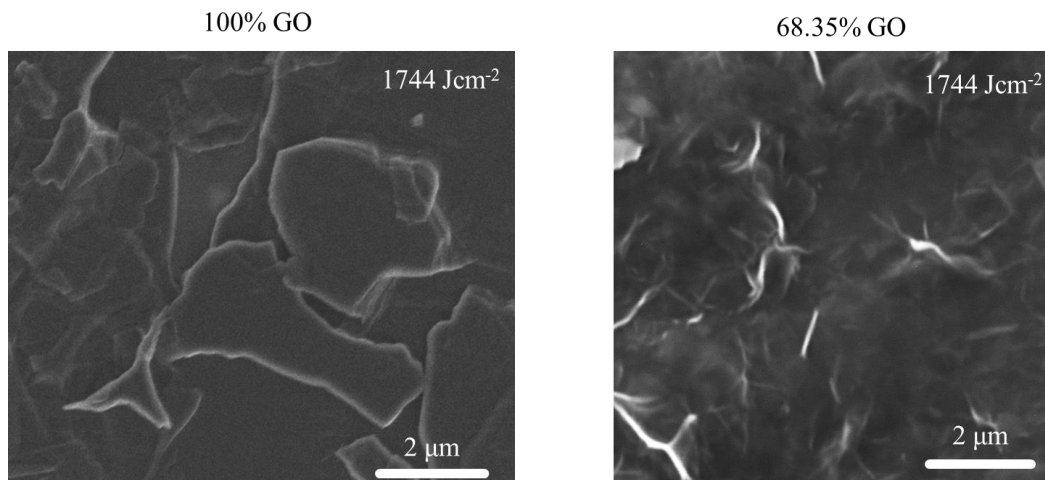


Figure 70: SEM images of 100% GO (left) and 68.35% GO films after Incremental IPL Processing with an Energy Density Input of 1744Jcm^{-2} .

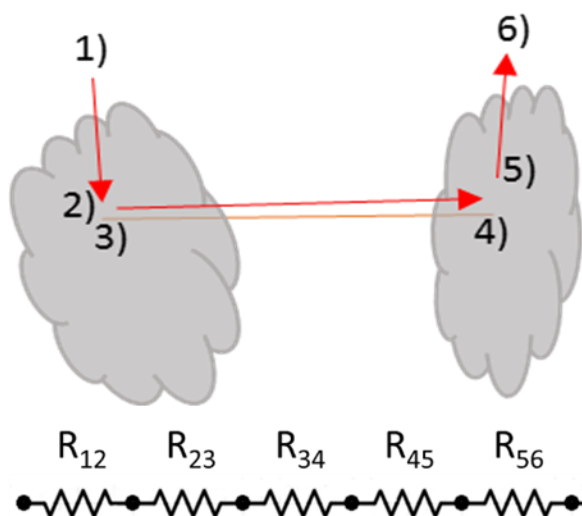


Figure 71: Schematic for current passing through a rGO nanosheet (grey) to a Cu NW (orange) and then to another rGO nanosheet (gray), with corresponding electrical resistances shown where R_{23} and R_{45} are the contact resistances between the Cu and rGO.

C. Summary

In summary, this chapter has shown that IPL Processing has the ability to rapidly reduce GO into electrically conductive rGO and produced favorable results through addition of fructose into ink formulations. This was shown by sheet resistance values that decreased four magnitudes. Furthermore, the IPL Processing of GO films was improved by applying incremental pulses that were able to maintain film morphology. The flexibility of these films was exemplified on a plastic substrate, which became electrically conductive with only one pulse of IPL Processing. Lastly, the use of inks composed of GO and Cu(OH)_2 NW mixtures did lead to better electrical performance of films.

CONCLUSIONS

Intense Pulsed Light Processing has been implemented to three different morphologies and four materials to create conductive films. The inks exhibited increased solution stability due to their oxide and hydroxide forms.

The Cu₂O-NiO core-layer nanostructures were synthesized using a room temperature solution based method, deposited with spray coating, and IPL Processed. The final dispersions can be easily deposited on to a substrate using evaporative solution-phase techniques; in this case an ultrasonic spray was used to deposit films. During the initial synthesis stage Cu₂O nanoparticles were surrounded with a NiO layer. The subsequent IPL treatment reduced both oxides to their corresponding metal forms in less than 1½ minutes. In addition, the IPL process sinters neighboring particles and lowers the resistivity of the films. During stage two we controlled the thickness of the nickel layer. The processes were optimized so that the nickel layer uniformly coated the Cu₂O particles, as well as providing a degree of control over the layer thickness. Finally, in stage three by measuring the thermoelectric properties of silicon before and after being heated with Cu and Cu-Ni depositions, we have shown that the nickel layer is able to mitigate the diffusion of Cu into silicon. The next steps of this research are to investigate the decomposition of organic molecules throughout the IPL processing and discrete particles for isolated core/shell analysis.

Copper nitrate hydroxide was synthesized and successfully reduced into elemental copper, with the inclusion of fructose and glucose to decompose during the IPL process. The results shown help to further understand the reduction mechanism. Copper nitrate hydroxide was not found to transform into an intermediary copper oxide throughout the process. This is significant since less energy is required which is favorable for its viability in future commercial applications. As the copper nitrate hydroxide synthesized did convert to elemental copper only in the presence of the reducing agents, analysis of different organics, based on application, could be explored further. The lowest resistivity measured was $0.224 \Omega/\square$.

IPL processing of GO successfully reduced the material to rGO. The results also indicated that there is potential for this method in the scalable production of TCFs. The lowest sheet resistance achieved was $R_s=5.499 \text{ k}\Omega/\text{sq.}$, with a transparency of %T (550nm) = 10.13% and the most transparent sample, with a significantly reduced sheet resistance ($R_s=1.384 \text{ M}\Omega/\text{sq.}$), exhibited a transparency at 550nm of 55.58%. These findings are also enticing as application onto a flexible plastic substrate displayed the reduction after only a single pulse and could be bent without loss of conductance. Combining the GO with copper hydroxide nanowires did lead to a conductivity enhancement.

RECOMMENDATIONS FOR FUTURE WORK

The sheet resistances of the films could be improved by optimization of sugar ratios for both deposition and IPL Processing to enhance both film quality and efficient usage of energy, including modulating the number of pulses and the time interval between pulses affecting the local temperature rise in films for optimal processing. Additionally, further investigation of the implementation of plastic/flexible substrates in roll-to-roll deposition and IPL Processing followed by robust bending tests would help to demonstrate cost and scale advantages towards commercialization. As the substrates' surface properties would be significantly different, investigation into surface modification of substrates and/or doping of GO to enhance chemical interactions to favor single layer, flat, deposition would be advantageous. The performance of GO & Cu NW hybrids could be improved by the investigation into scalable and efficient synthesis of higher aspect ratio NWs with larger diameters closer to ~ 50 nm and lengths closer to ~ 100 μm). Lastly, thermal/kinetic modeling of IPL Processing of the various nanomaterials, especially GO, would enable predictive processing parameters and deeper understanding of optimizing IPL Processing.

REFERENCES

1. Riegel, S.; Mutter, F.; Lauermann, T.; Terheiden, B.; Hahn, G., Review on screen printed metallization on p-type silicon. *Energy Procedia* **2012**, *21*, 14-23.
2. Powell, D. M.; Winkler, M. T.; Choi, H. J.; Simmons, C. B.; Needleman, D. B.; Buonassisi, T., Crystalline silicon photovoltaics: a cost analysis framework for determining technology pathways to reach baseload electricity costs. *Energy & Environmental Science* **2012**, *5* (3), 5874-5883.
3. Weber, E. R., Transition metals in silicon. *Applied Physics A Solids and Surfaces* **1983**, *30* (1), 1-22.
4. Chromik, R. R.; Neils, W. K.; Cotts, E. J., Thermodynamic and kinetic study of solid state reactions in the Cu-Si system. *Journal of Applied Physics* **1999**, *86* (8), 4273.
5. Istratov, A. A.; Weber, E. R., Physics of Copper in Silicon. *Journal of The Electrochemical Society* **2002**, *149* (1), G21.
6. Ono, H.; Nakano, T.; Ohta, T., Diffusion barrier effects of transition metals for Cu/M/Si multilayers (M=Cr, Ti, Nb, Mo, Ta, W). *Applied Physics Letters* **1994**, *64* (12), 1511.
7. Wang, S.-Q., Barriers Against Copper Diffusion into Silicon and Drift Through Silicon Dioxide. *MRS Bulletin* **1994**, *19* (08), 30-40.
8. Henley, W. B.; Ramappa, D. A.; Jastrezbski, L., Detection of copper contamination in silicon by surface photovoltage diffusion length measurements. *Applied Physics Letters* **1999**, *74* (2), 278.
9. Estreicher, S. K., Rich chemistry of copper in crystalline silicon. *Physical Review B* **1999**, *60* (8), 5375-5382.
10. Park, S.-H.; Kim, H.-S., Flash light sintering of nickel nanoparticles for printed electronics. *Thin Solid Films* **2014**, *550*, 575-581.
11. Perelaer, J.; Abbel, R.; Wunscher, S.; Jani, R.; van Lammeren, T.; Schubert, U. S., Roll-to-roll compatible sintering of inkjet printed features by photonic and microwave exposure: from non-conductive ink to 40% bulk silver conductivity in less than 15 seconds. *Advanced Materials* **2012**, *24* (19), 2620-5.
12. Goodrich, A.; Hacke, P.; Wang, Q.; Sopori, B.; Margolis, R.; James, T. L.; Woodhouse, M., A wafer-based monocrystalline silicon photovoltaics road map: Utilizing known technology improvement opportunities for further reductions in manufacturing costs. *Solar Energy Materials and Solar Cells* **2013**, *114*, 110-135.
13. Hansen, J.; Sato, M.; Ruedy, R.; Lo, K.; Lea, D. W.; Medina-Elizade, M., Global temperature change. *Proceedings of the National Academy of Sciences* **2006**, *103* (39), 14288-14293.
14. Jeong, S.; Song, H. C.; Lee, W. W.; Lee, S. S.; Choi, Y.; Son, W.; Kim, E. D.; Paik, C. H.; Oh, S. H.; Ryu, B. H., Stable aqueous based Cu nanoparticle ink for printing

- well-defined highly conductive features on a plastic substrate. *Langmuir* **2011**, *27* (6), 3144-9.
15. Niittynen, J.; Abbel, R.; Mäntysalo, M.; Perelaer, J.; Schubert, U. S.; Lupo, D., Alternative sintering methods compared to conventional thermal sintering for inkjet printed silver nanoparticle ink. *Thin Solid Films* **2014**, *556*, 452-459.
 16. Wünscher, S.; Abbel, R.; Perelaer, J.; Schubert, U. S., Progress of alternative sintering approaches of inkjet-printed metal inks and their application for manufacturing of flexible electronic devices. *Journal of Materials Chemistry C* **2014**, *2* (48), 10232-10261.
 17. Kwan, Y. C. G.; Le, Q. L.; Huan, C. H. A., Time to failure modeling of silver nanowire transparent conducting electrodes and effects of a reduced graphene oxide over layer. *Solar Energy Materials and Solar Cells* **2016**, *144*, 102-108.
 18. Ahn, Y.; Jeong, Y.; Lee, D.; Lee, Y., Copper nanowire-graphene core-shell nanostructure for highly stable transparent conducting electrodes. *ACS Nano* **2015**, *9* (3), 3125-33.
 19. Kim, W. K.; Lee, S.; Hee Lee, D.; Hee Park, I.; Seong Bae, J.; Woo Lee, T.; Kim, J. Y.; Hun Park, J.; Chan Cho, Y.; Ryong Cho, C.; Jeong, S. Y., Cu mesh for flexible transparent conductive electrodes. *Sci Rep* **2015**, *5*, 10715.
 20. Kiruthika, S.; Gupta, R.; Rao, K. D. M.; Chakraborty, S.; Padmavathy, N.; Kulkarni, G. U., Large area solution processed transparent conducting electrode based on highly interconnected Cu wire network. *Journal of Materials Chemistry C* **2014**, *2* (11), 2089.
 21. Mayousse, C.; Celle, C.; Carella, A.; Simonato, J.-P., Synthesis and purification of long copper nanowires. Application to high performance flexible transparent electrodes with and without PEDOT:PSS. *Nano Research* **2014**, *7* (3), 315-324.
 22. Zhu, Y.; Cai, W.; Piner, R. D.; Velamakanni, A.; Ruoff, R. S., Transparent self-assembled films of reduced graphene oxide platelets. *Applied Physics Letters* **2009**, *95* (10), 103104.
 23. Eda, G.; Fanchini, G.; Chhowalla, M., Large-area ultrathin films of reduced graphene oxide as a transparent and flexible electronic material. *Nature Nanotechnology* **2008**, *3* (5), 270-4.
 24. Becerril, H. A.; Mao, J.; Liu, Z.; Stoltenberg, R. M.; Bao, Z.; Chen, Y., Evaluation of solution-processed reduced graphene oxide films as transparent conductors. *ACS Nano* **2008**, *2* (3), 463-70.
 25. Shi, L.; Yang, J.; Yang, T.; Hanxun, Q.; Li, J.; Zheng, Q., Molecular level controlled fabrication of highly transparent conductive reduced graphene oxide/silver nanowire hybrid films. *RSC Advances* **2014**, *4* (81), 43270-43277.
 26. Kholmanov, I. N.; Domingues, S. H.; Chou, H.; Wang, X.; Tan, C.; Kim, J. Y.; Li, H.; Piner, R.; Zarbin, A. J.; Ruoff, R. S., Reduced graphene oxide/copper nanowire hybrid films as high-performance transparent electrodes. *ACS Nano* **2013**, *7* (2), 1811-6.
 27. Li, X.; Zhu, Y.; Cai, W.; Borysiak, M.; Han, B.; Chen, D.; Piner, R. D.; Colombo, L.; Ruoff, R. S., Transfer of large-area graphene films for high-performance transparent conductive electrodes. *Nano Letters* **2009**, *9* (12), 4359-63.

28. Chen, J.-H.; Jang, C.; Xiao, S.; Ishigami, M.; Fuhrer, M. S., Intrinsic and extrinsic performance limits of graphene devices on SiO₂. *Nature Nanotechnology* **2008**, *3* (4), 206-209.
29. Kim, K. S.; Zhao, Y.; Jang, H.; Lee, S. Y.; Kim, J. M.; Kim, K. S.; Ahn, J. H.; Kim, P.; Choi, J. Y.; Hong, B. H., Large-scale pattern growth of graphene films for stretchable transparent electrodes. *Nature* **2009**, *457* (7230), 706-10.
30. Majumder, M.; Rendall, C.; Li, M.; Behabtu, N.; Eukel, J. A.; Hauge, R. H.; Schmidt, H. K.; Pasquali, M., Insights into the physics of spray coating of SWNT films. *Chemical Engineering Science* **2010**, *65* (6), 2000-2008.
31. Haacke, G., New figure of merit for transparent conductors. *Journal of Applied Physics* **1976**, *47* (9), 4086.
32. Nam, V.; Lee, D., Copper Nanowires and Their Applications for Flexible, Transparent Conducting Films: A Review. *Nanomaterials* **2016**, *6* (3), 47.
33. Zhu, S.; Gao, Y.; Hu, B.; Li, J.; Su, J.; Fan, Z.; Zhou, J., Transferable self-welding silver nanowire network as high performance transparent flexible electrode. *Nanotechnology* **2013**, *24* (33), 335202.
34. Sachse, C.; Weiß, N.; Gaponik, N.; Müller-Meskamp, L.; Eychmüller, A.; Leo, K., ITO-Free, Small-Molecule Organic Solar Cells on Spray-Coated Copper-Nanowire-Based Transparent Electrodes. *Advanced Energy Materials* **2014**, *4* (2), 1300737.
35. Zhou, H.-M.; Yi, D.-Q.; Yu, Z.-M.; Xiao, L.-R.; Li, J., Preparation of aluminum doped zinc oxide films and the study of their microstructure, electrical and optical properties. *Thin Solid Films* **2007**, *515* (17), 6909-6914.
36. Nair, R. R.; Blake, P.; Grigorenko, A. N.; Novoselov, K. S.; Booth, T. J.; Stauber, T.; Peres, N. M.; Geim, A. K., Fine structure constant defines visual transparency of graphene. *Science* **2008**, *320* (5881), 1308.
37. Garg, R.; Dutta, N.; Choudhury, N., Work Function Engineering of Graphene. *Nanomaterials* **2014**, *4* (2), 267-300.
38. Geim, A. K.; Novoselov, K. S., The rise of graphene. *Nature Materials* **2007**, *6* (3), 183-91.
39. Wang, X.; Zhi, L.; Müllen, K., Transparent, Conductive Graphene Electrodes for Dye-Sensitized Solar Cells. *Nano Letters* **2008**, *8* (1), 323-327.
40. Ahn, J.-H.; Hong, B. H., Graphene for displays that bend. *Nature Nanotechnology* **2014**, *9* (10), 737-738.
41. Zhu, Y.; Murali, S.; Cai, W.; Li, X.; Suk, J. W.; Potts, J. R.; Ruoff, R. S., Graphene and graphene oxide: synthesis, properties, and applications. *Advanced Materials* **2010**, *22* (35), 3906-24.
42. Mattevi, C.; Kim, H.; Chhowalla, M., A review of chemical vapour deposition of graphene on copper. *Journal of Materials Chemistry* **2011**, *21* (10), 3324.
43. Hummers, W. S.; Offeman, R. E., Preparation of Graphitic Oxide. *Journal of the American Chemical Society* **1958**, *80* (6), 1339-1339.
44. Eda, G.; Chhowalla, M., Chemically Derived Graphene Oxide: Towards Large-Area Thin-Film Electronics and Optoelectronics. *Advanced Materials* **2010**, *22* (22), 2392-2415.

45. Yun, J. M.; Yeo, J. S.; Kim, J.; Jeong, H. G.; Kim, D. Y.; Noh, Y. J.; Kim, S. S.; Ku, B. C.; Na, S. I., Solution-processable reduced graphene oxide as a novel alternative to PEDOT:PSS hole transport layers for highly efficient and stable polymer solar cells. *Advanced Materials* **2011**, *23* (42), 4923-4928.
46. Paredes, J. I.; Villar-Rodil, S.; Solis-Fernandez, P.; Martinez-Alonso, A.; Tascon, J. M., Atomic force and scanning tunneling microscopy imaging of graphene nanosheets derived from graphite oxide. *Langmuir* **2009**, *25* (10), 5957-68.
47. Bich Ha, N.; Van Hieu, N., Promising applications of graphene and graphene-based nanostructures. *Advances in Natural Sciences: Nanoscience and Nanotechnology* **2016**, *7* (2), 023002.
48. Shang, J.; Ma, L.; Li, J.; Ai, W.; Yu, T.; Gurzadyan, G. G., The Origin of Fluorescence from Graphene Oxide. *Sci Rep* **2012**, *2*, 792.
49. Galande, C.; Mohite, A. D.; Naumov, A. V.; Gao, W.; Ci, L.; Ajayan, A.; Gao, H.; Srivastava, A.; Weisman, R. B.; Ajayan, P. M., Quasi-Molecular Fluorescence from Graphene Oxide. *Sci Rep* **2011**, *1*, 85.
50. Chng, E. L. K.; Pumera, M., The Toxicity of Graphene Oxides: Dependence on the Oxidative Methods Used. *Chemistry – A European Journal* **2013**, *19* (25), 8227-8235.
51. Rauti, R.; Lozano, N.; León, V.; Scaini, D.; Musto, M.; Rago, I.; Ulloa Severino, F. P.; Fabbro, A.; Casalis, L.; Vázquez, E.; Kostarelos, K.; Prato, M.; Ballerini, L., Graphene Oxide Nanosheets Reshape Synaptic Function in Cultured Brain Networks. *ACS Nano* **2016**, *10* (4), 4459-4471.
52. Gilje, S.; Dubin, S.; Badakhshan, A.; Farrar, J.; Danczyk, S. A.; Kaner, R. B., Photothermal deoxygenation of graphene oxide for patterning and distributed ignition applications. *Advanced Materials* **2010**, *22* (3), 419-23.
53. An, B. W.; Kim, K.; Kim, M.; Kim, S.-Y.; Hur, S.-H.; Park, J.-U., Direct Printing of Reduced Graphene Oxide on Planar or Highly Curved Surfaces with High Resolutions Using Electrohydrodynamics. *Small* **2015**, *11* (19), 2263-2268.
54. Kholmanov, I. N.; Stoller, M. D.; Edgeworth, J.; Lee, W. H.; Li, H.; Lee, J.; Barnhart, C.; Potts, J. R.; Piner, R.; Akinwande, D.; Barrick, J. E.; Ruoff, R. S., Nanostructured hybrid transparent conductive films with antibacterial properties. *ACS Nano* **2012**, *6* (6), 5157-63.
55. Wei, G.; Yu, J.; Gu, M.; Tang, T. B., Dielectric relaxation and hopping conduction in reduced graphite oxide. *Journal of Applied Physics* **2016**, *119* (22), 224102.
56. Stobinski, L.; Lesiak, B.; Malolepszy, A.; Mazurkiewicz, M.; Mierzwa, B.; Zemek, J.; Jiricek, P.; Bieloshapka, I., Graphene oxide and reduced graphene oxide studied by the XRD, TEM and electron spectroscopy methods. *Journal of Electron Spectroscopy and Related Phenomena* **2014**, *195*, 145-154.
57. Tien, H.-W.; Huang, Y.-L.; Yang, S.-Y.; Hsiao, S.-T.; Liao, W.-H.; Li, H.-M.; Wang, Y.-S.; Wang, J.-Y.; Ma, C.-C. M., Preparation of transparent, conductive films by graphenenanosheet deposition on hydrophilic or hydrophobic surfaces through control of the pH value. *Journal of Materials Chemistry* **2012**, *22* (6), 2545-2552.

58. Niu, Y.; Zhao, J.; Zhang, X.; Wang, X.; Wu, J.; Li, Y.; Li, Y., Large area orientation films based on graphene oxide self-assembly and low-temperature thermal reduction. *Applied Physics Letters* **2012**, *101* (18), 181903.
59. Watcharotone, S.; Dikin, D. A.; Stankovich, S.; Piner, R.; Jung, I.; Dommett, G. H.; Evmenenko, G.; Wu, S. E.; Chen, S. F.; Liu, C. P.; Nguyen, S. T.; Ruoff, R. S., Graphene-silica composite thin films as transparent conductors. *Nano Letters* **2007**, *7* (7), 1888-92.
60. Wang, J.; Liang, M.; Fang, Y.; Qiu, T.; Zhang, J.; Zhi, L., Rod-coating: towards large-area fabrication of uniform reduced graphene oxide films for flexible touch screens. *Advanced Materials* **2012**, *24* (21), 2874-8.
61. Li, X.; Zhang, G.; Bai, X.; Sun, X.; Wang, X.; Wang, E.; Dai, H., Highly conducting graphene sheets and Langmuir-Blodgett films. *Nature Nanotechnology* **2008**, *3* (9), 538-42.
62. Shin, H.-J.; Kim, K. K.; Benayad, A.; Yoon, S.-M.; Park, H. K.; Jung, I.-S.; Jin, M. H.; Jeong, H.-K.; Kim, J. M.; Choi, J.-Y.; Lee, Y. H., Efficient Reduction of Graphite Oxide by Sodium Borohydride and Its Effect on Electrical Conductance. *Advanced Functional Materials* **2009**, *19* (12), 1987-1992.
63. Su, C.-Y.; Xu, Y.; Zhang, W.; Zhao, J.; Tang, X.; Tsai, C.-H.; Li, L.-J., Electrical and Spectroscopic Characterizations of Ultra-Large Reduced Graphene Oxide Monolayers. *Chemistry of Materials* **2009**, *21* (23), 5674-5680.
64. Dan, B.; Irvin, G. C.; Pasquali, M., Continuous and Scalable Fabrication of Transparent Conducting Carbon Nanotube Films. *ACS Nano* **2009**, *3* (4), 835-843.
65. Jeong, C.; Nair, P.; Khan, M.; Lundstrom, M.; Alam, M. A., Prospects for nanowire-doped polycrystalline graphene films for ultratransparent, highly conductive electrodes. *Nano Letters* **2011**, *11* (11), 5020-5.
66. Tsen, A. W.; Brown, L.; Levendorf, M. P.; Ghahari, F.; Huang, P. Y.; Havener, R. W.; Ruiz-Vargas, C. S.; Muller, D. A.; Kim, P.; Park, J., Tailoring electrical transport across grain boundaries in polycrystalline graphene. *Science* **2012**, *336* (6085), 1143-6.
67. Layani, M.; Kamyshny, A.; Magdassi, S., Transparent conductors composed of nanomaterials. *Nanoscale* **2014**, *6* (11), 5581-91.
68. Won, Y.; Kim, A.; Lee, D.; Yang, W.; Woo, K.; Jeong, S.; Moon, J., Annealing-free fabrication of highly oxidation-resistive copper nanowire composite conductors for photovoltaics. *NPG Asia Materials* **2014**, *6* (6), e105.
69. Michaelson, H. B., The work function of the elements and its periodicity. *Journal of Applied Physics* **1977**, *48* (11), 4729-4733.
70. Hu, X.; Chen, L.; Ji, T.; Zhang, Y.; Hu, A.; Wu, F.; Li, G.; Chen, Y., Roll-to-Roll Production of Graphene Hybrid Electrodes for High-Efficiency, Flexible Organic Photoelectronics. *Advanced Materials Interfaces* **2015**, *2* (17), 1500445.
71. Deng, B.; Hsu, P.-C.; Chen, G.; Chandrashekar, B. N.; Liao, L.; Ayitimuda, Z.; Wu, J.; Guo, Y.; Lin, L.; Zhou, Y.; Aisijiang, M.; Xie, Q.; Cui, Y.; Liu, Z.; Peng, H., Roll-to-Roll Encapsulation of Metal Nanowires between Graphene and Plastic Substrate for High-Performance Flexible Transparent Electrodes. *Nano Letters* **2015**, *15* (6), 4206-4213.

72. Dong, P.; Zhu, Y.; Zhang, J.; Peng, C.; Yan, Z.; Li, L.; Peng, Z.; Ruan, G.; Xiao, W.; Lin, H.; Tour, J. M.; Lou, J., Graphene on Metal Grids as the Transparent Conductive Material for Dye Sensitized Solar Cell. *The Journal of Physical Chemistry C* **2014**, *118* (45), 25863-25868.
73. Zhou, T.; Liu, F.; Suganuma, K.; Nagao, S., Use of graphene oxide in achieving high overall thermal properties of polymer for printed electronics. *RSC Advances* **2016**, *6* (25), 20621-20628.
74. Domingues, S. H.; Kholmanov, I. N.; Kim, T.; Kim, J.; Tan, C.; Chou, H.; Alieva, Z. A.; Piner, R.; Zarbin, A. J. G.; Ruoff, R. S., Reduction of graphene oxide films on Al foil for hybrid transparent conductive film applications. *Carbon* **2013**, *63*, 454-459.
75. Luechinger, N. A.; Athanassiou, E. K.; Stark, W. J., Graphene-stabilized copper nanoparticles as an air-stable substitute for silver and gold in low-cost ink-jet printable electronics. *Nanotechnology* **2008**, *19* (44), 445201.
76. Li, B.; Zhang, X.; Chen, P.; Li, X.; Wang, L.; Zhang, C.; Zheng, W.; Liu, Y., Waveband-dependent photochemical processing of graphene oxide in fabricating reduced graphene oxide film and graphene oxide-Ag nanoparticles film. *RSC Advances* **2014**, *4* (5), 2404-2408.
77. Magdassi, S.; Grouchko, M.; Kamyshny, A., Copper Nanoparticles for Printed Electronics: Routes Towards Achieving Oxidation Stability. *Materials* **2010**, *3* (9), 4626-4638.
78. Liu, Q.-m.; Zhou, D.-b.; Yamamoto, Y.; Ichino, R.; Okido, M., Preparation of Cu nanoparticles with NaBH₄ by aqueous reduction method. *Transactions of Nonferrous Metals Society of China* **2012**, *22* (1), 117-123.
79. Li, D.; Sutton, D.; Burgess, A.; Graham, D.; Calvert, P. D., Conductive copper and nickel lines via reactive inkjet printing. *Journal of Materials Chemistry* **2009**, *19* (22), 3719.
80. Wu, S. H.; Chen, D. H., Synthesis of high-concentration Cu nanoparticles in aqueous CTAB solutions. *Journal of Colloid and Interface Science* **2004**, *273* (1), 165-9.
81. Deng, D.; Jin, Y.; Cheng, Y.; Qi, T.; Xiao, F., Copper nanoparticles: aqueous phase synthesis and conductive films fabrication at low sintering temperature. *ACS Applied Materials & Interfaces* **2013**, *5* (9), 3839-46.
82. Xiong, J.; Wang, Y.; Xue, Q.; Wu, X., Synthesis of highly stable dispersions of nanosized copper particles using l-ascorbic acid. *Green Chemistry* **2011**, *13* (4), 900.
83. Wu, C.; Mosher, B. P.; Zeng, T., One-step green route to narrowly dispersed copper nanocrystals. *Journal of Nanoparticle Research* **2006**, *8* (6), 965-969.
84. Tang, X.-F.; Yang, Z.-G.; Wang, W.-J., A simple way of preparing high-concentration and high-purity nano copper colloid for conductive ink in inkjet printing technology. *Colloids and Surfaces A: Physicochemical and Engineering Aspects* **2010**, *360* (1-3), 99-104.
85. Park, B. K.; Jeong, S.; Kim, D.; Moon, J.; Lim, S.; Kim, J. S., Synthesis and size control of monodisperse copper nanoparticles by polyol method. *Journal of Colloid and Interface Science* **2007**, *311* (2), 417-24.

86. Zhu, H.-t.; Zhang, C.-y.; Yin, Y.-s., Rapid synthesis of copper nanoparticles by sodium hypophosphite reduction in ethylene glycol under microwave irradiation. *Journal of Crystal Growth* **2004**, *270* (3-4), 722-728.
87. Blosi, M.; Albonetti, S.; Dondi, M.; Martelli, C.; Baldi, G., Microwave-assisted polyol synthesis of Cu nanoparticles. *Journal of Nanoparticle Research* **2010**, *13* (1), 127-138.
88. Cuya Huaman, J. L.; Sato, K.; Kurita, S.; Matsumoto, T.; Jeyadevan, B., Copper nanoparticles synthesized by hydroxyl ion assisted alcohol reduction for conducting ink. *Journal of Materials Chemistry* **2011**, *21* (20), 7062.
89. Huang, L.; Jiang, H.; Zhang, J.; Zhang, Z.; Zhang, P., Synthesis of copper nanoparticles containing diamond-like carbon films by electrochemical method. *Electrochemistry Communications* **2006**, *8* (2), 262-266.
90. Zhou, X. J.; Harmer, A. J.; Heinig, N. F.; Leung, K. T., Parametric Study on Electrochemical Deposition of Copper Nanoparticles on an Ultrathin Polypyrrole Film Deposited on a Gold Film Electrode. *Langmuir* **2004**, *20* (12), 5109-5113.
91. Ryu, J.; Kim, H.-S.; Hahn, H. T., Reactive Sintering of Copper Nanoparticles Using Intense Pulsed Light for Printed Electronics. *Journal of Electronic Materials* **2010**, *40* (1), 42-50.
92. Liu, Z.; Yang, Y.; Liang, J.; Hu, Z.; Li, S.; Peng, S.; Qian, Y., Synthesis of Copper Nanowires via a Complex-Surfactant-Assisted Hydrothermal Reduction Process. *The Journal of Physical Chemistry B* **2003**, *107* (46), 12658-12661.
93. Ponce, A. A.; Klabunde, K. J., Chemical and catalytic activity of copper nanoparticles prepared via metal vapor synthesis. *Journal of Molecular Catalysis A: Chemical* **2005**, *225* (1), 1-6.
94. Condorelli, G. G.; Costanzo, L. L.; Fragalà, I. L.; Giuffrida, S.; Ventimiglia, G., A single photochemical route for the formation of both copper nanoparticles and patterned nanostructured films. *Journal of Materials Chemistry* **2003**, *13* (10), 2409-2411.
95. Kitchens, C. L.; McLeod, M. C.; Roberts, C. B., Chloride ion effects on synthesis and directed assembly of copper nanoparticles in liquid and compressed alkane microemulsions. *Langmuir* **2005**, *21* (11), 5166-73.
96. Capek, I., Preparation of metal nanoparticles in water-in-oil (w/o) microemulsions. *Advances in Colloid and Interface Science* **2004**, *110* (1-2), 49-74.
97. Mohamed, M. A.; Galwey, A. K.; Halawy, S. A., A comparative study of the thermal reactivities of some transition metal oxalates in selected atmospheres. *Thermochimica Acta* **2005**, *429* (1), 57-72.
98. Salavati-Niasari, M.; Davar, F., Synthesis of copper and copper(I) oxide nanoparticles by thermal decomposition of a new precursor. *Materials Letters* **2009**, *63* (3-4), 441-443.
99. Kumar, B.; Saha, S.; Basu, M.; Ganguli, A. K., Enhanced hydrogen/oxygen evolution and stability of nanocrystalline (4–6 nm) copper particles. *Journal of Materials Chemistry A* **2013**, *1* (15), 4728.
100. Carroll, K. J.; Calvin, S.; Ekiert, T. F.; Unruh, K. M.; Carpenter, E. E., Selective Nucleation and Growth of Cu and Ni Core/Shell Nanoparticles. *Chemistry of Materials* **2010**, *22* (7), 2175-2177.

101. Yamauchi, T.; Tsukahara, Y.; Sakata, T.; Mori, H.; Yanagida, T.; Kawai, T.; Wada, Y., Magnetic Cu-Ni (core-shell) nanoparticles in a one-pot reaction under microwave irradiation. *Nanoscale* **2010**, *2* (4), 515-23.
102. Chang, Y.; Lye, M. L.; Zeng, H. C., Large-scale synthesis of high-quality ultralong copper nanowires. *Langmuir* **2005**, *21* (9), 3746-8.
103. Shi, Y.; Li, H.; Chen, L.; Huang, X., Obtaining ultra-long copper nanowires via a hydrothermal process. *Science and Technology of Advanced Materials* **2005**, *6* (7), 761-765.
104. Jin, M.; He, G.; Zhang, H.; Zeng, J.; Xie, Z.; Xia, Y., Shape-controlled synthesis of copper nanocrystals in an aqueous solution with glucose as a reducing agent and hexadecylamine as a capping agent. *Angewandte Chemie International Edition* **2011**, *50* (45), 10560-4.
105. Zheng, Y.; Liang, J.; Chen, Y.; Liu, Z., Economical and green synthesis of Cu nanowires and their use as a catalyst for selective hydrogenation of cinnamaldehyde. *RSC Advances* **2014**, *4* (78), 41683-41689.
106. Dharmadasa, R.; Jha, M.; Amos, D. A.; Druffel, T., Room temperature synthesis of a copper ink for the intense pulsed light sintering of conductive copper films. *ACS Applied Materials & Interfaces* **2013**, *5* (24), 13227-13234.
107. Ranjbar-Karimi, R.; Bazmandegan-Shamili, A.; Aslani, A.; Kaviani, K., Sonochemical synthesis, characterization and thermal and optical analysis of CuO nanoparticles. *Physica B: Condensed Matter* **2010**, *405* (15), 3096-3100.
108. Sunkara, S.; Vendra, V. K.; Kim, J. H.; Druffel, T.; Sunkara, M. K., Scalable synthesis and photoelectrochemical properties of copper oxide nanowire arrays and films. *Catalysis Today* **2013**, *199*, 27-35.
109. Orel, Z. C.; Anžlovar, A.; Dražić, G.; Žigon, M., Cuprous Oxide Nanowires Prepared by an Additive-Free Polyol Process. *Crystal Growth & Design* **2007**, *7* (2), 453-458.
110. Zhang, L.; Lu, W.; Feng, Y.; Ni, J.; Lu, Y.; Shang, X., Facile Synthesis of Leaf-like Cu(OH)₂ and Its Conversion into CuO with Nanopores. *Acta Physico-Chimica Sinica* **2008**, *24* (12), 2257-2262.
111. Li, Y.; Yang, X. Y.; Rooke, J.; Van Tendeloo, G.; Su, B. L., Ultralong Cu(OH)₂ and CuO nanowire bundles: PEG200-directed crystal growth for enhanced photocatalytic performance. *Journal of Colloid and Interface Science* **2010**, *348* (2), 303-12.
112. Linder, G. G.; Atanasov, M.; Pebler, J., A Single-Crystal Study of the Magnetic Behavior and Exchange Coupling in Cu₂(OH)₃NO₃. *Journal of Solid State Chemistry* **1995**, *116* (1), 1-7.
113. Park, S. H.; Kim, H. J., Unidirectionally aligned copper hydroxide crystalline nanorods from two-dimensional copper hydroxy nitrate. *Journal of the American Chemical Society* **2004**, *126* (44), 14368-9.
114. Niu, H.; Yang, Q.; Tang, K., A new route to copper nitrate hydroxide microcrystals. *Materials Science & Engineering: B* **2006**, *135* (2), 172-175.
115. Henrist, C.; Traina, K.; Hubert, C.; Toussaint, G.; Rulmont, A.; Cloots, R., Study of the morphology of copper hydroxynitrate nanoplatelets obtained by controlled

- double jet precipitation and urea hydrolysis. *Journal of Crystal Growth* **2003**, 254 (1-2), 176-187.
116. Wang, X.-b.; Huang, L.-n., A novel one-step method to synthesize copper nitrate hydroxide nanorings. *Transactions of Nonferrous Metals Society of China* **2009**, 19, s480-s484.
 117. Hofmann, U.; Holst, R., Über die Säurenatur und die Methylierung von Graphitoxyd. *Berichte der deutschen chemischen Gesellschaft (A and B Series)* **1939**, 72 (4), 754-771.
 118. Staudenmaier, L., Verfahren zur Darstellung der Graphitsäure. *Berichte der deutschen chemischen Gesellschaft* **1898**, 31 (2), 1481-1487.
 119. Zhu, Y.; James, D. K.; Tour, J. M., New Routes to Graphene, Graphene Oxide and Their Related Applications. *Advanced Materials* **2012**, 24 (36), 4924-4955.
 120. Marcano, D. C.; Kosynkin, D. V.; Berlin, J. M.; Sinitskii, A.; Sun, Z.; Slesarev, A.; Alemany, L. B.; Lu, W.; Tour, J. M., Improved Synthesis of Graphene Oxide. *ACS Nano* **2010**, 4 (8), 4806-4814.
 121. Sun, X.; Luo, D.; Liu, J.; Evans, D. G., Monodisperse Chemically Modified Graphene Obtained by Density Gradient Ultracentrifugal Rate Separation. *ACS Nano* **2010**, 4 (6), 3381-3389.
 122. Rourke, J. P.; Pandey, P. A.; Moore, J. J.; Bates, M.; Kinloch, I. A.; Young, R. J.; Wilson, N. R., The Real Graphene Oxide Revealed: Stripping the Oxidative Debris from the Graphene-like Sheets. *Angewandte Chemie International Edition* **2011**, 50 (14), 3173-3177.
 123. Kim, D.; Moon, J., Highly Conductive Ink Jet Printed Films of Nanosilver Particles for Printable Electronics. *Electrochemical and Solid-State Letters* **2005**, 8 (11), J30.
 124. Kirkpatrick, A. R. For localized thermal processing. 1979.
 125. Pope, D. S.; Schroder, K. A.; Rawson, I. M. Method for Reducing Thin Films on Low Temperature Substrates. 2011.
 126. Fink, R. L.; Novak, J. P.; Ginsberg, V. Sintering metallic inks on low melting point substrates. WO2013052721A1, 2013.
 127. Pan, J.; Le, H.; Kucherenko, S.; Yeomans, J. A., A model for the sintering of spherical particles of different sizes by solid state diffusion. *Acta Materialia* **1998**, 46 (13), 4671-4690.
 128. Naik, K. S.; Sglavo, V. M.; Raj, R., Flash sintering as a nucleation phenomenon and a model thereof. *Journal of the European Ceramic Society* **2014**, 34 (15), 4063-4067.
 129. Song, Y.-W.; Park, S.-H.; Han, W.-S.; Hong, J.-M.; Kim, H.-S., Single-step high-speed nanogranulation of metal alloy around carbon nanotubes by flash light irradiation. *Materials Letters* **2011**, 65 (15-16), 2510-2513.
 130. Sazgarnia, A.; Shanei, A.; Shanei, M. M., Monitoring of transient cavitation induced by ultrasound and intense pulsed light in presence of gold nanoparticles. *Ultrason Sonochem* **2014**, 21 (1), 268-74.
 131. Ryu, J.; Kim, K.; Kim, H. S.; Hahn, H. T.; Lashmore, D., Intense pulsed light induced platinum-gold alloy formation on carbon nanotubes for non-enzymatic glucose detection. *Biosens Bioelectron* **2010**, 26 (2), 602-7.

132. Abbel, R.; van Lammeren, T.; Hendriks, R.; Ploegmakers, J.; Rubingh, E. J.; Meinders, E. R.; Groen, W. A., Photonic flash sintering of silver nanoparticle inks: a fast and convenient method for the preparation of highly conductive structures on foil. *MRS Communications* **2012**, *2* (04), 145-150.
133. Chung, W. H.; Hwang, H. J.; Lee, S. H.; Kim, H. S., In situ monitoring of a flash light sintering process using silver nano-ink for producing flexible electronics. *Nanotechnology* **2013**, *24* (3), 035202.
134. Galagan, Y.; Coenen, E. W. C.; Abbel, R.; van Lammeren, T. J.; Sabik, S.; Barink, M.; Meinders, E. R.; Andriessen, R.; Blom, P. W. M., Photonic sintering of inkjet printed current collecting grids for organic solar cell applications. *Organic Electronics* **2013**, *14* (1), 38-46.
135. Hösel, M.; Krebs, F. C., Large-scale roll-to-roll photonic sintering of flexo printed silver nanoparticle electrodes. *Journal of Materials Chemistry* **2012**, *22* (31), 15683.
136. Lee, D. J.; Park, S. H.; Jang, S.; Kim, H. S.; Oh, J. H.; Song, Y. W., Pulsed light sintering characteristics of inkjet-printed nanosilver films on a polymer substrate. *Journal of Micromechanics and Microengineering* **2011**, *21* (12), 125023.
137. Yung, K. C.; Gu, X.; Lee, C. P.; Choy, H. S., Ink-jet printing and camera flash sintering of silver tracks on different substrates. *Journal of Materials Processing Technology* **2010**, *210* (15), 2268-2272.
138. Han, W. S.; Hong, J. M.; Kim, H. S.; Song, Y. W., Multi-pulsed white light sintering of printed Cu nanoinks. *Nanotechnology* **2011**, *22* (39), 395705.
139. Hwang, H. J.; Chung, W. H.; Kim, H. S., In situ monitoring of flash-light sintering of copper nanoparticle ink for printed electronics. *Nanotechnology* **2012**, *23* (48), 485205.
140. Kim, H.-S.; Dhage, S. R.; Shim, D.-E.; Hahn, H. T., Intense pulsed light sintering of copper nanoink for printed electronics. *Applied Physics A* **2009**, *97* (4), 791-798.
141. Zhong, Z.; Woo, K.; Kim, I.; Hwang, H.; Kwon, S.; Choi, Y.-M.; Lee, Y.; Lee, T.-M.; Kim, K.; Moon, J., Roll-to-roll-compatible, flexible, transparent electrodes based on self-nanoembedded Cu nanowires using intense pulsed light irradiation. *Nanoscale* **2016**, *8* (16), 8995-9003.
142. Cui, H.-W.; Jiu, J.-T.; Nagao, S.; Sugahara, T.; Suganuma, K.; Uchida, H.; Schroder, K. A., Ultra-fast photonic curing of electrically conductive adhesives fabricated from vinyl ester resin and silver micro-flakes for printed electronics. *RSC Advances* **2014**, *4* (31), 15914-15922.
143. Li, R.-Z.; Hu, A.; Zhang, T.; Oakes, K. D., Direct Writing on Paper of Foldable Capacitive Touch Pads with Silver Nanowire Inks. *ACS Applied Materials & Interfaces* **2014**, *6* (23), 21721-21729.
144. Song, C.-H.; Ok, K.-H.; Lee, C.-J.; Kim, Y.; Kwak, M.-G.; Han, C. J.; Kim, N.; Ju, B.-K.; Kim, J.-W., Intense-pulsed-light irradiation of Ag nanowire-based transparent electrodes for use in flexible organic light emitting diodes. *Organic Electronics* **2015**, *17*, 208-215.
145. Jiu, J.; Sugahara, T.; Nogi, M.; Araki, T.; Suganuma, K.; Uchida, H.; Shinozaki, K., High-intensity pulse light sintering of silver nanowire transparent films on

- polymer substrates: the effect of the thermal properties of substrates on the performance of silver films. *Nanoscale* **2013**, *5* (23), 11820-8.
146. Jiu, J.; Nogi, M.; Sugahara, T.; Tokuno, T.; Araki, T.; Komoda, N.; Suganuma, K.; Uchida, H.; Shinozaki, K., Strongly adhesive and flexible transparent silver nanowire conductive films fabricated with a high-intensity pulsed light technique. *Journal of Materials Chemistry* **2012**, *22* (44), 23561.
 147. Yang, S.; Choi, H.; Lee, D. S.; Choi, C.; Choi, S.; Kim, I., Improved Optical Sintering Efficiency at the Contacts of Silver Nanowires Encapsulated by a Graphene Layer. *Small* **2014**, *11* (11), 1293.
 148. Dharmadasa, R.; Dharmadasa, I. M.; Druffel, T., Intense Pulsed Light Sintering of Electrodeposited CdS Thin Films. *Advanced Engineering Materials* **2014**, *16* (11), 1351-1361.
 149. Colorado, H. A.; Dhage, S. R.; Hahn, H. T., Thermo chemical stability of cadmium sulfide nanoparticles under intense pulsed light irradiation and high temperatures. *Materials Science & Engineering: B* **2011**, *176* (15), 1161-1168.
 150. Dharmadasa, R.; Lavery, B.; Dharmadasa, I. M.; Druffel, T., Intense Pulsed Light Treatment of Cadmium Telluride Nanoparticle-Based Thin Films. *ACS Applied Materials & Interfaces* **2014**, *6* (7), 5034-5040.
 151. Jang, K.; Yu, S.; Park, S.-H.; Kim, H.-S.; Ahn, H., Intense pulsed light-assisted facile and agile fabrication of cobalt oxide/nickel cobaltite nanoflakes on nickel-foam for high performance supercapacitor applications. *Journal of Alloys and Compounds* **2015**, *618*, 227-232.
 152. Zhang, J.-Y.; Boyd, I. W., Low temperature photo-oxidation of silicon using a xenon excimer lamp. *Applied Physics Letters* **1997**, *71* (20), 2964-2966.
 153. Drahi, E.; Blayac, S.; Borbely, A.; Benaben, P., Impact of ink synthesis on processing of inkjet-printed silicon nanoparticle thin films: A comparison of Rapid Thermal Annealing and photonic sintering. *Thin Solid Films* **2015**, *574*, 169-176.
 154. Secor, E. B.; Ahn, B. Y.; Gao, T. Z.; Lewis, J. A.; Hersam, M. C., Rapid and Versatile Photonic Annealing of Graphene Inks for Flexible Printed Electronics. *Advanced Materials* **2015**, *27* (42), 6683-6688.
 155. Dhage, S. R.; Kim, H.-S.; Hahn, H. T., Cu(In,Ga)Se₂ Thin Film Preparation from a Cu(In,Ga) Metallic Alloy and Se Nanoparticles by an Intense Pulsed Light Technique. *Journal of Electronic Materials* **2010**, *40* (2), 122-126.
 156. Kim, I.; Han, H.-S.; Kwak, S.-W.; Yu, J.-S.; Kim, B.; Jang, Y.; Lee, T.-M., Formulation and Characterization of CuIn_{1-x}Ga_xSe₂Ink for Gravure Offset Printing. *Japanese Journal of Applied Physics* **2013**, *52* (5S1), 05DB17.
 157. Dhage, S. R.; Thomas Hahn, H., Rapid treatment of CIGS particles by intense pulsed light. *Journal of Physics and Chemistry of Solids* **2010**, *71* (10), 1480-1483.
 158. Singh, M.; Jiu, J.; Sugahara, T.; Suganuma, K., Photonic sintering of thin film prepared by dodecylamine capped CuIn_xGa_{1-x}Se₂ nanoparticles for printed photovoltaics. *Thin Solid Films* **2014**, *565*, 11-18.
 159. Lavery, B. W.; Kumari, S.; Konermann, H.; Draper, G. L.; Spurgeon, J.; Druffel, T., Intense Pulsed Light Sintering of CH₃NH₃PbI₃ Solar Cells. *ACS Applied Materials & Interfaces* **2016**, *8* (13), 8419-8426.

160. Lee, J. H.; Lee, Y. M.; Lim, S. J.; Choi, D. K.; Yu, J.-W., Intense pulsed light annealed buffer layers for organic photovoltaics. *Solar Energy Materials and Solar Cells* **2015**, *143*, 517-521.
161. Song, C.-H.; Han, C. J.; Ju, B.-K.; Kim, J.-W., Photoenhanced Patterning of Metal Nanowire Networks for Fabrication of Ultraflexible Transparent Devices. *ACS Applied Materials & Interfaces* **2016**, *8* (1), 480-489.
162. Park, S.-H.; Chung, W.-H.; Kim, H.-S., Temperature changes of copper nanoparticle ink during flash light sintering. *Journal of Materials Processing Technology* **2014**, *214* (11), 2730-2738.
163. Buffat, P.; Borel, J. P., Size effect on the melting temperature of gold particles. *Physical Review A* **1976**, *13* (6), 2287-2298.
164. Pham, L. Q.; Sohn, J. H.; Kim, C. W.; Park, J. H.; Kang, H. S.; Lee, B. C.; Kang, Y. S., Copper nanoparticles incorporated with conducting polymer: effects of copper concentration and surfactants on the stability and conductivity. *Journal of Colloid and Interface Science* **2012**, *365* (1), 103-9.
165. Biçer, M.; Şişman, İ., Controlled synthesis of copper nano/microstructures using ascorbic acid in aqueous CTAB solution. *Powder Technology* **2010**, *198* (2), 279-284.
166. Deng, D.; Qi, T.; Cheng, Y.; Jin, Y.; Xiao, F., Copper carboxylate with different carbon chain lengths as metal–organic decomposition ink. *Journal of Materials Science: Materials in Electronics* **2013**, *25* (1), 390-397.
167. Jha, M.; Dharmadasa, R.; Draper, G. L.; Sherehiy, A.; Sumanasekera, G.; Amos, D.; Druffel, T., Solution phase synthesis and intense pulsed light sintering and reduction of a copper oxide ink with an encapsulating nickel oxide barrier. *Nanotechnology* **2015**, *26* (17), 175601.
168. Paquet, C.; James, R.; Kell, A. J.; Mozenson, O.; Ferrigno, J.; Lafrenière, S.; Malenfant, P. R. L., Photosintering and electrical performance of CuO nanoparticle inks. *Organic Electronics* **2014**, *15* (8), 1836-1842.
169. Wang, B. Y.; Yoo, T. H.; Song, Y. W.; Lim, D. S.; Oh, Y. J., Cu ion ink for a flexible substrate and highly conductive patterning by intensive pulsed light sintering. *ACS Applied Materials & Interfaces* **2013**, *5* (10), 4113-9.
170. Draper, G. L.; Dharmadasa, R.; Staats, M. E.; Lavery, B. W.; Druffel, T. L., Fabrication of Elemental Copper by Intense Pulsed Light Processing of a Copper Nitrate Hydroxide Ink. *ACS Applied Materials & Interfaces* **2015**, 150708113307008.
171. Araki, T.; Sugahara, T.; Jiu, J.; Nagao, S.; Nogi, M.; Koga, H.; Uchida, H.; Shinozaki, K.; Suganuma, K., Cu salt ink formulation for printed electronics using photonic sintering. *Langmuir* **2013**, *29* (35), 11192-7.
172. Chua, C. K.; Pumera, M., Chemical reduction of graphene oxide: a synthetic chemistry viewpoint. *Chemical Society Reviews* **2014**, *43* (1), 291-312.
173. Dhifaf, A. J.; Neus, L.; Kostas, K., Synthesis of few-layered, high-purity graphene oxide sheets from different graphite sources for biology. *2D Materials* **2016**, *3* (1), 014006.
174. Pei, S.; Cheng, H.-M., The reduction of graphene oxide. *Carbon* **2012**, *50* (9), 3210-3228.

175. Some, S.; Kim, S.; Samanta, K.; Kim, Y.; Yoon, Y.; Park, Y.; Lee, S. M.; Lee, K.; Lee, H., Fast synthesis of high-quality reduced graphene oxide at room temperature under light exposure. *Nanoscale* **2014**, *6* (19), 11322-7.
176. Chen, W.; Yan, L., Preparation of graphene by a low-temperature thermal reduction at atmosphere pressure. *Nanoscale* **2010**, *2* (4), 559-563.
177. Gengler, R. Y. N.; Spyrou, K.; Rudolf, P., A roadmap to high quality chemically prepared graphene. *Journal of Physics D: Applied Physics* **2010**, *43* (37), 374015.
178. Xie, G.; Forslund, M.; Pan, J., Direct electrochemical synthesis of reduced graphene oxide (rGO)/copper composite films and their electrical/electroactive properties. *ACS Applied Materials & Interfaces* **2014**, *6* (10), 7444-55.
179. Li, W.; Yang, Y. J., The reduction of graphene oxide by elemental copper and its application in the fabrication of graphene supercapacitor. *Journal of Solid State Electrochemistry* **2014**, *18* (6), 1621-1626.
180. Pei, S.; Zhao, J.; Du, J.; Ren, W.; Cheng, H.-M., Direct reduction of graphene oxide films into highly conductive and flexible graphene films by hydrohalic acids. *Carbon* **2010**, *48* (15), 4466-4474.
181. Fan, X.; Peng, W.; Li, Y.; Li, X.; Wang, S.; Zhang, G.; Zhang, F., Deoxygenation of Exfoliated Graphite Oxide under Alkaline Conditions: A Green Route to Graphene Preparation. *Advanced Materials* **2008**, *20* (23), 4490-4493.
182. Zhu, C.; Guo, S.; Fang, Y.; Dong, S., Reducing Sugar: New Functional Molecules for the Green Synthesis of Graphene Nanosheets. *ACS Nano* **2010**, *4* (4), 2429-2437.
183. Zhou, Y.; Bao, Q.; Tang, L. A. L.; Zhong, Y.; Loh, K. P., Hydrothermal Dehydration for the "Green" Reduction of Exfoliated Graphene Oxide to Graphene and Demonstration of Tunable Optical Limiting Properties. *Chemistry of Materials* **2009**, *21* (13), 2950-2956.
184. Gengler, R. Y.; Badali, D. S.; Zhang, D.; Dimos, K.; Spyrou, K.; Gournis, D.; Miller, R. J., Revealing the ultrafast process behind the photoreduction of graphene oxide. *Nature Communications* **2013**, *4*, 2560.
185. Huang, L.; Liu, Y.; Ji, L.-C.; Xie, Y.-Q.; Wang, T.; Shi, W.-Z., Pulsed laser assisted reduction of graphene oxide. *Carbon* **2011**, *49* (7), 2431-2436.
186. Cote, L. J.; Cruz-Silva, R.; Huang, J., Flash reduction and patterning of graphite oxide and its polymer composite. *Journal of the American Chemical Society* **2009**, *131* (31), 11027-32.
187. Kumar, P.; Subrahmanyam, K. S.; Rao, C. N. R., Graphene Produced by Radiation-Induced Reduction of Graphene Oxide. *International Journal of Nanoscience* **2011**, *10* (04n05), 559-566.
188. Williams, G.; Seger, B.; Kamat, P. V., TiO₂-graphene nanocomposites. UV-assisted photocatalytic reduction of graphene oxide. *ACS Nano* **2008**, *2* (7), 1487-91.
189. Childres, I.; Jauregui, L. A.; Park, W.; Cao, H.; Chen, Y. P., Raman spectroscopy of graphene and related materials. *New Developments in Photon and Materials Research* **2013**, *1*.

190. Ferrari, A. C.; Meyer, J. C.; Scardaci, V.; Casiraghi, C.; Lazzeri, M.; Mauri, F.; Piscanec, S.; Jiang, D.; Novoselov, K. S.; Roth, S.; Geim, A. K., Raman Spectrum of Graphene and Graphene Layers. *Physical Review Letters* **2006**, *97* (18), 187401.
191. Al-Hamry, A.; Kang, H.; Sowade, E.; Dzhagan, V.; Rodriguez, R. D.; Müller, C.; Zahn, D. R. T.; Baumann, R. R.; Kanoun, O., Tuning the reduction and conductivity of solution-processed graphene oxide by intense pulsed light. *Carbon* **2016**, *102*, 236-244.
192. Sung-Hyeon, P.; Hak-Sung, K., Environmentally benign and facile reduction of graphene oxide by flash light irradiation. *Nanotechnology* **2015**, *26* (20), 205601.
193. Arapov, K.; Bex, G.; Hendriks, R.; Rubingh, E.; Abbel, R.; de With, G.; Friedrich, H., Conductivity Enhancement of Binder-Based Graphene Inks by Photonic Annealing and Subsequent Compression Rolling *Advanced Engineering Materials* **2016**, *18* (7), 1234-1239.
194. Kim, J. Y.; Rodriguez, J. A.; Hanson, J. C.; Frenkel, A. I.; Lee, P. L., Reduction of CuO and Cu₂O with H₂: H embedding and kinetic effects in the formation of suboxides. *Journal of the American Chemical Society* **2003**, *125* (35), 10684-92.
195. Svintsitskiy, D. A.; Kardash, T. Y.; Stonkus, O. A.; Slavinskaya, E. M.; Stadnichenko, A. I.; Koscheev, S. V.; Chupakhin, A. P.; Boronin, A. I., In Situ XRD, XPS, TEM, and TPR Study of Highly Active in CO Oxidation CuO Nanopowders. *The Journal of Physical Chemistry C* **2013**, *117* (28), 14588-14599.
196. Richardson, J., X-ray diffraction study of nickel oxide reduction by hydrogen. *Applied Catalysis A: General* **2003**, *246* (1), 137-150.
197. Kern, W., The Evolution of Silicon Wafer Cleaning Technology. *Journal of The Electrochemical Society* **1990**, *137* (6), 1887-1892.
198. van den Ende, D. A.; Hendriks, R.; Cauchois, R.; Groen, W. A., Large area photonic flash soldering of thin chips on flex foils for flexible electronic systems: In situ temperature measurements and thermal modelling. *Electronic Materials Letters* **2014**, *10* (6), 1175-1183.
199. Xu, Y.; Schoonen, M. A. A., The absolute energy positions of conduction and valence bands of selected semiconducting minerals. *American Mineralogist* **2000**, *85* (3-4), 543.
200. Rossiter, W. J.; Godette, M.; Brown, P. W.; Galuk, K. G., An investigation of the degradation of aqueous ethylene glycol and propylene glycol solutions using ion chromatography. *Solar Energy Materials* **1985**, *11* (5-6), 455-467.
201. Rice, F. O.; Vollrath, R. E., The Thermal Decomposition of Acetone in the Gaseous State. *Proceedings of the National Academy of Sciences* **1929**, *15* (9), 702-705.
202. Johnson, B. C., Electrical resistivity of copper and nickel thin-film interconnections. *Journal of Applied Physics* **1990**, *67* (6), 3018-3024.
203. Istratov, A. A.; Weber, E. R., Electrical properties and recombination activity of copper, nickel and cobalt in silicon. *Applied Physics A: Materials Science & Processing* **1998**, *66* (2), 123-136.
204. Hall, R. N.; Racette, J. H., Diffusion and Solubility of Copper in Extrinsic and Intrinsic Germanium, Silicon, and Gallium Arsenide. *Journal of Applied Physics* **1964**, *35* (2), 379-397.

205. Wang, M. T., Barrier Properties of Very Thin Ta and TaN Layers Against Copper Diffusion. *Journal of The Electrochemical Society* **1998**, *145* (7), 2538.
206. Arizaga, G.; Satyanarayana, K.; Wypych, F., Layered hydroxide salts: Synthesis, properties and potential applications. *Solid State Ionics* **2007**, *178* (15-18), 1143-1162.
207. Witowski, J.; Jorres, A., Glucose degradation products: relationship with cell damage. *Peritoneal Dialysis International* **2000**, *20*, S31-S36.
208. Soininen, P. J.; Elers, K. E.; Saanila, V.; Kaipio, S.; Sajavaara, T.; Haukka, S., Reduction of Copper Oxide Film to Elemental Copper. *Journal of The Electrochemical Society* **2005**, *152* (2), G122.
209. Lee, J. W.; Thomas, L. C.; Schmidt, S. J., Investigation of the heating rate dependency associated with the loss of crystalline structure in sucrose, glucose, and fructose using a thermal analysis approach (part I). *Journal of Agricultural and Food Chemistry* **2011**, *59* (2), 684-701.
210. Setzer, W. N., A DFT analysis of thermal decomposition reactions important to natural products. *Natural Product Communications* **2010**, *5* (7), 993-998.

CURRICULUM VITAE

Gabriel L. Draper
gabriel.draper@gmail.com

Education

Ph.D. Candidate – Chemical Engineering
University of Louisville – GPA:3.6
Dissertation Topic: December 2016
“Conductive Inks and Films via Intense Pulsed Light”
Advisors: Dr. Thad Druffel & Dr. Mahendra Sunkara
B.S. Chemical Engineering – Environmental Emphasis
Minors: Chemistry, Biochemistry May
University of Colorado at Boulder – GPA: 3.1 2012
Advisors: Dr. Charles Musgrave & Dr. Wendy Young

Publications

Gabriel L. Draper, Callie Shadrick, Madalyn Wead, Preston Dukes, Nathan Allen, Joshua Jacob, Brandon W. Lavery, Thad Druffel
Reduction of Graphene Oxide via Intense Pulsed Light (under submission)

Zachary Herde, Jagannadh Satyavolu, Gamini Sumanasekera, Ruchira Dharmasena, Gabriel L. Draper
Production of High Surface Area Activated Carbons for Energy Storage Applications using Residual Fiber from a C5-Biorefinery (under submission)

Brandon W. Lavery, Sudesh Kumari, Hannah Konermann, Gabriel L. Draper, Joshua Spurgeon, and Thad Druffel
Intense Pulsed Light Sintering of $CH_3NH_3PbI_3$ Solar Cells
ACS Applied Materials & Interfaces **2016** 8 (13), 8419-8426 DOI: 10.1021/acsami.5b10166

Gabriel L. Draper, Ruvini Dharmadasa, Meghan E. Staats, Brandon W. Lavery, and Thad Druffel
Fabrication of Elemental Copper by Intense Pulsed Light Processing of a Copper Nitrate Hydroxide Ink
ACS Applied Materials & Interfaces 2015 7 (30), 16478-16485 DOI: 10.1021/acsami.5b03854

Jha, M., R. Dharmadasa, G.L. Draper, A. Sherehiy, G. Sumanasekera, D. Amos and T. Druffel
Solution phase synthesis and intense pulsed light sintering and reduction of a copper oxide ink with an encapsulating nickel oxide barrier
Nanotechnology, 2015. **26**(17): p. 175601 DOI:10.1088/0957-4484/26/17/175601

Presentations

Fabrication of Elemental Copper by Intense Pulsed Light Processing of a Copper Nitrate Hydroxide Ink

- 2015 Conn Center RE³ Workshop
- NOBCChE National Convention 2015

Inkjet printing quantum dots in hybrid inorganic-organic LEDs

Gabriel Draper, Michael McCreary, Dr. Menaka Jha, Dr. Vaddiraju, and Dr. Delaina Amos

- NOBCChE National Convention 2013
- 2013 Conn Center RE³ Workshop

Research Experience

Graduate Assistant – University of Louisville – Chemical Engineering Department
Advisors: Dr. Thad Druffel and Dr. Mahendra Sunkara

2012-2016

Thesis Topic: Conductive Inks and Films via Intense Pulsed Light Processing

- Analyzed material characteristics throughout varying extents of rapid millisecond time-frame IPL processing
- Collaboratively wrote Commercialization Fund Proposal with research mentor (awarded for \$75,000)
- Engaged in safety training and protocols to help create laboratory safety culture (including chemical inventories, hazardous waste disposal, informal training of less experienced lab-mates, and safe operating procedure documents)
- Synthesis of conductive precursors (i.e. copper oxide, copper hydroxide, and graphene oxide) as functional aqueous based inks for large area roll-to-roll processing towards commercial applications in next-gen photovoltaics and flexible electronics

Professional Research Experience Program Fellowship Student
National Institute of Standards and Technology (Boulder, CO)

2011-2012

- Analyzed and investigated thermo-chemical property journal articles and extracted purities, methods and data
- Applied uncertainties to experimental data that properly reflect methods used
- Established system to increase project efficiency by 20% by preventing redundancies in peer projects
- Processed data from research articles (written in English, French, German, and Russian) cross-checked with Ghemling's VLE Data Collection

Laboratory & Experimental Techniques

Material Characterization

- DLS - Dynamic Light Scattering Particle Size Analyzer
- DSC – Differential Scanning Calorimetry
- Four-Point Probe
- FTIR - Fourier Transform Infrared Spectroscopy
- Profilometry
- Raman Spectroscopy
- Optical Microscopy
- SEM - Scanning Electron Microscopy
- Solar Spectrum Testing Equipment
- SDT – Simultaneous DSC & TGA
- TGA - Thermogravimetric Analysis
- UV-Vis - Ultraviolet–Visible Spectroscopy
- XRD - X-Ray Diffraction

Deposition Techniques

- Chemical Vapor Deposition
- Doctor Blading
- Drop-Casting
- Inkjet Printing
- Microspray Deposition
- Screen Printing
- Spin-Coating
- Sputtering
- Thermal Evaporation
- Ultrasonic Spray Deposition

Processing Techniques

- Centrifugation
- Decantation
- Oxygen Plasma Treatment
- Intense Pulsed Light Processing
- Sonication

Synthesis Experience

- Graphene Oxide via a modified Hummer's Method
- $\text{CuNO}_3(\text{OH})_3$ Nanoparticles
- Cu/Cu₂O Nanoparticles via Reduction with NaBH₄
- Cu₂O/NiO Encapsulated Nanoparticles
- Cu(OH)₂ Nanowires
- TiO₂ Nanoparticles
- CVD Graphene

Teaching Experience

Graduate Teaching Assistant (GTA), University of Louisville – Chemical Engineering

- Materials Science (CHE 253)* Summer 2016
- Coached and coordinated thirteen (13) Undergraduate Teaching Assistants with fellow GTA to grade assignments and deliberating learning with students
 - Collaborated on grading examinations with fellow GTA and the Professor
 - Guest Lecture - Diffusion
- Modeling & Transport Phenomena (CHE 520)* Spring 2016
- Formative Feedback and interpersonal interaction with in-class group assignments
 - Executing grading of in-class and take-home (combined 50% of total grade)
- Chemical Engineering Kinetics and Chemical Reactors (CHE 441)* Fall 2015
- Collaborative relationship with Professor to establish
 - Taught two-lectures on determining rate-law
- Safety, Health, and the Environment (CHE 401)* Summer 2015
- Graded work to facilitate learning and navigating “gray areas” of ethics
- Principles of Fluid Dynamics (CHE 331)* Summer 2015
- Special Guest Lecture & Exam Review: Pedagogy & Exam Skills
 - Sample Activity for Student Engagement:
 - Notecards – Students were asked to give names (and pronunciations), reasoning for interest in chemical engineering, FUN FACT, and check-in upcoming exam
 - Created and distributed custom “Goodbye Letters” by hand – Positive Expression and Recognition of student growth & future potential
 - Provided flexible office hours and availability through various media
- Chemical Engineering Heat and Mass Transfer (CHE 433)* Spring 2015
- Established office hours and flexible appointment times with students
 - Create own solutions for HW
 - Navigated conflicts between Professor/Self/Students/Administration to work towards equitable learning environment
- Chemical Engineering Kinetics and Chemical Reactors (CHE 441)* Fall 2014
- Collaborated with Professor to implement student friendly alternative grading system focused on identifying and correcting errors rather than penalizing them
 - Executed problem sessions highlighting importance of problems and challenging areas
 - Administered office hours to facilitate student learning

Guest Speaker/Lecturer – GEARUP – (three-hour session) 2015 - 2016

- Encouraged STEM to 28 low socioeconomic high school students
- Coupled storytelling and learning the concept of evolution to engage inclusive learning environment
- Hands-on chemistry demonstration and experiment to discuss creating scientific questions and utilizing the scientific method

Guest Lecture – “Scale” for Sustainability Course February 2016

Upper Division Elective – Department of Sustainability and Urban Development

Presentation at Kentucky Science Teacher Association (KSTA) November 2015

in collaboration with Kentucky Science Association (KSA) and WKU

Co-Presenter - “*What Floats Your Boat?*” NGSS Lesson by KY Academy of Science
Kerrie McDaniel (WKU), Amanda Fuller (KSA), and Gabriel Draper

Guest Lecture – Chemical Engineering Thermodynamics II (CHE 312) Summer 2015

Created and Facilitated “Fugacity Feud” Interactive & Collaborative Game to both provide an examination review and also engage students

Leadership Experience

National Assistant Treasurer, (NOBCCHE) 2016

President & Founder, Minority Association of Graduate Students (MAGS) 2015 - 2016

- Established constitution, built a leadership team, and launched unique student organization
- Collaborated with organizations such as Graduate Student Council, Counseling Center, and Cultural Center
- Created Welcoming Event during Orientation specifically for Minority Graduate Students
- Collaborated with Leadership Team to create Survey to identify key areas of need

President & Founder, Native American Student Organization (NASO) 2012-2016

- Visited Indiana University’s Health and Wellness Pow-wow
- Recognized at Women’s Basketball Native American Appreciation Night (2014, 2015)
- Walked out onto center court with other members/advisor
- Designed and implemented cultural awareness events
- Coordinated outreach with Aldente for middle school student after school activities outreach

National Finance Chairperson, National Society of Black Engineers (NSBE) 2013-2014

- Designed and facilitated Board of Corporate Affiliate (BCA) Meetings then produced Career Fair Preparation and Follow-up Guide for NSBE Membership based on recruiter input
- Collaborated with NSBE World Headquarters (WHQ) staff and Finance Zone to make financial decisions
- Lead and coordinated National Finance Committee consisting of six

- Regional Finance Chairs and five full time WHQ employees on direction of corporate, university, and organizational partnerships
- Coordinated consistency of partnership packets across the six Regions resulting in a 38% revenue increase
 - Increased number of BCA partners from 48 to 53 despite anticipated drop to 46
- Region III Finance Chairperson, National Society of Black Engineers (NSBE) 2012-2013
- Represented 3,000-member region to corporate partners
 - Created templates and documentation for position transitions
 - Designed and distributed the Region III Corporate Partnership Packet raising \$51,000 during the Fall Regional Conference
 - Fostered partnerships with 23 companies and four organizations
- Senior Design Project Team Lead 2012
University of Colorado at Boulder
- Simulated concentrated solar power plant configurations for molten nitrate salts, alumina, and two reduction/oxidation chemical cycles
 - Prepared Presentations, arranged meetings with company liaison, and constructed project timeline
 - Wrote professional reports summarizing project processes and goals detailed with equipment design, environmental and safety hazards, and economic analysis
 - Conducted presentation for professors and peers detailing project results
- Chapter President, NSBE University of Colorado at Boulder Chapter 2011-2012
- Developed an engineering Retention and Mentoring Program
 - Increased chapter size by 30%, fundraising by \$12,000 (120%), and activity with the surrounding
 - community by 20%
- Marketing Chairperson, NSBE Region 6 Fall Regional Conference 2011
- Recruited seven committee members and facilitated weekly online meetings
 - Created a marketing competition, website, and fliers
 - Exceeded expected attendance of 300 attendees for conference by 182
- Vice President, NSBE University of Colorado at Boulder Chapter 2010-2011
- Established connections with on campus organizations in order to generate support and collaboration
 - Inspired superior communication within chapter executive board resulting a 50% increase in successful programs
- Resident Advisor, Housing and Dining 2009-2010
- Coached and facilitated growth of 35 residents in residence hall
 - Collaborated with 14 RAs to create and deliver educational programs and presentations with guest speakers
 - Organized on campus, social events to support positive recreation among residents

Funding Board Representative, Residence Hall Association 2008-2009

- Worked with six other students to manage a \$5000 budget for on campus programs

Engineering Quad Representative, Residence Hall Association 2008-2009

- Advocated for supports and policy improvements benefiting engineering students
- Robert's Rules of Order

Professional Development

PLAN (Professional Development, Life Skills, Academic Development, Networking)

University of Louisville - School of Interdisciplinary and Graduate Studies (SIGS)

Graduate Teaching Assistant Academy 2015-2016

- Creating a Civil Classroom Culture: Classroom Management Strategies
- Learning Science: Using What We Know about How Students Learn
- Active Learning and Productive Discussions
- Teaching for Your Peers: Micro-Teaching and Peer Feedback Session
- Constructing Your Philosophy of Teaching Statement
- Turning Motivation Research into Teaching Strategies You Can Use
- Measuring Learning Using Formative Assessment Techniques
- Integrating Technology into Your Classroom: A Panel Discussion
- Teaching for Your Peers: Micro-Teaching and Peer Feedback Session

Grant Writing Academy Fall 2015

- Developing Your Idea
- Finding Funding
- Writing the Proposal
- Building Your Budget
- The Experts' Perspective
- Writing Center Workshopping
- Post-Award Grant Management

STEM Graduate Teaching Assistant Mini-Academy Summer 2015

- Students Today: Understanding and Leveraging Characteristics of Today's Students
- Learning Science: Using What We Know about How Students Learn
- Measuring Learning: Formative and Summative Assessment to Improve Student Learning
- Experimenting with Interaction: Designing Activities for a Lab Course
- Micro-Teaching: Teaching for and Providing Feedback to your Peers

Graduate Teaching Assistants & Diversity Spring 2015

- Understanding the Implications of your Cultural Identities as the Instructor
- Navigating Subtle Racism in the Classroom
- Teaching as Social Justice: Creating Equitable Expectations as the Instructor
- Handling Advisors' and Professors' Cultural Insensitivities Towards You
- Navigating the Job Market: Networking and Interviewing as a Culturally Responsive Applicant
- Looking Forward: Integrating Multiculturalism into a Teaching Philosophy

<u>Human Resources (University of Louisville)</u>	2015-2016
<ul style="list-style-type: none"> • Keeping the PEACC: Green Dot Bystander Training • Qualities of an Effective Supervisor • Title IX Mandatory Reporter Training • Delivering Excellent Customer Service 	
<u>Conn Center for Renewable Energy</u>	2015 - 2016
<ul style="list-style-type: none"> • Sexual Harassment Awareness Training (minors on campus) 	
<u>COACH</u> – Half-day workshop Conflict Resolution and Negotiations	2015

Awards and Recognition

<ul style="list-style-type: none"> • NOBCCChE Advancing Science Award 	2016
<ul style="list-style-type: none"> • School of Interdisciplinary Graduate Studies Dean’s Reception <ul style="list-style-type: none"> ○ Certificate for Completion – GTA Academy ○ Certificate for Completion – Grant Writing Academy ○ Certificate for Completion – STEM GTA Mini-Academy ○ Certificate for Dedication – Professional Development ○ Certificate for Participation – M.A.G.S. Leadership 	2016
<ul style="list-style-type: none"> • University of Louisville Student Awards <ul style="list-style-type: none"> ○ M.A.G.S. Diversity & Inclusion Award (Organization) ○ M.A.G.S. ft. Counseling Center, Graduate Student Council: Collaboration Event of the Year Award (Organization) 	2016
<ul style="list-style-type: none"> • Student Leadership Profile 	2016
<ul style="list-style-type: none"> • Nomination for Faculty Favorite 	2015
<ul style="list-style-type: none"> • COACH Travel Award 	2015
<ul style="list-style-type: none"> • NOBCCChE Advancing Science Award 	2015
<ul style="list-style-type: none"> • Patent License Award presented at the Celebration of Faculty Excellence “The President, Provost, and Executive Vice President for Research and Innovation with to acknowledge and comment the novel and useful creation developed through the scientific and investigative efforts of Delaina Amos, Gabriel Draper, and Thad Druffel as exemplified by the Exclusive License to Bert Thin Films, LLC for Novel Processes for the Synthesis and Deposition of Copper Nanoparticles executed on June 30, 2015” 	2015
<ul style="list-style-type: none"> • School of Interdisciplinary Graduate Studies Dean’s Reception <ul style="list-style-type: none"> ○ Participation in Graduate Teaching Assistant & Diversity Workshops ○ Certificate for Dedication to Professional Development ○ Certificate for Participation – M.A.G.S. Leadership 	2015
<ul style="list-style-type: none"> • 3rd Place Poster Presentation at Conn Center RE³ National Workshop 	2015
<ul style="list-style-type: none"> • Scholarship Award – University of Louisville – Student Awards 	2014
<ul style="list-style-type: none"> • Honorary Mention at RE3 Workshop Poster Presentation 	2013
<ul style="list-style-type: none"> • NSF/NOBCCChE Advancing Science Award 	2013
<ul style="list-style-type: none"> • Ethnic Minority Graduate Assistantship 	2012
<ul style="list-style-type: none"> • NSBE Small Chapter of the Year (National) 	2012
<ul style="list-style-type: none"> • NSBE Third Place Retention Program (National) 	2012
<ul style="list-style-type: none"> • BOLD Center Olympian Award 	2012
<ul style="list-style-type: none"> • NACME Scholar 	2011

Professional Society Memberships

- Kentucky Academy of Science (KAS) 2014 - 2016
- Golden Key Honor Society (UofL Chapter) 2014 - 2016
- National Organization for the Professional Advancement of Black Chemists and Chemical Engineers (NOBCCChE) 2013 - 2016
- Omega Chi Epsilon (American Honor Society for Chemical Engineering) 2011 - 2012
- National Society of Black Engineers (NSBE) 2008 - 2016

Conference Attendance

- UofL Celebration of Teaching and Learning 2016
- Rumble Young Man Rumble 2015
- Conn Center Renewable Energy Workshop 2013 & 2015
- Biomimicry Symposium (Conn Center and Biology Department) 2015
- NOBCCChE National Convention 2013, 2015, & 2016
- NSBE National Convention 2010 - 2014

Misc. University of Louisville Campus Involvement

- Cultural Center Search Committee (x2) 2016
- Commission on Diversity and Racial Equality (CODRE) 2015 - 2016
- Commission on the Status of Women (COSW) 2015 - 2016
- Speed School Student Affairs Committee 2015 - 2016
- Undocumented Student Resource Coalition 2015 - 2016
- Speed School Supreme Court Justice for Student Government Association 2015 - 2016
- Minority Association of Graduate Students 2015 - 2016
- Science Policy and Outreach Group 2014 - 2016
- Speed School Diversity Committee 2014 - 2016
- Speed School Student Council 2014 - 2016
- Entrepreneurship Club 2013 - 2014
- Social Swat Team 2013 - 2016
- African American Male Initiative/Student African American Brotherhood 2012 - 2016
- Native American Student Organization 2012 - 2016
- Ultimate Frisbee Team (Club) 2013 - 2016

Misc. Community Engagement and Mentoring

- Atkinson Elementary School – Mentoring Program 2015 - 2016
- Volunteer Judge – Louisville Regional Science Fair 2015 - 2016
- Rumble Young Man Rumble 5 (RYMR5) Planning Committee 2014 - 2015
- Right Turn Mentoring Program – Mentor 2014 - 2015
- Host/MC for Spotlight Interviews for 1LoveLou 2015
- Alumni Mentor – ChemBio Eng. CU Boulder 2014 - 2015